UCLouvain

FACULTE DES SCIENCES

Faculté des sciences

Liquid Crystals as Ion Conductors in Solid Polymer Electrolytes for Lithium Metal Batteries

Auteure : Mathilde SOMVILLE

Promoteur : Pr. Jean-François Gohy

Lecteurs : Pr. Charles-André Fustin
Pr. Olivier Riant
Pr. Alexandru Vlad

Année académique : 2021-2022

Mémoire de fin d'études présenté en vue de l'obtention du diplôme de master en sciences chimiques à finalité : chimie de l'industrie.

Remerciements

Tout d'abord, j'adresse mes remerciements à mon promoteur, Pr. Jean-François Gohy pour son accueil au sein de son équipe pour la réalisation de ce travail.

Je tiens à remercier mon encadrant, Isaac Álvarez Moisés, qui m'a suivi et guidé tout au long de ce travail. Ton aide m'a permis de mener à bien ce projet. Merci pour le soutien et les précieux conseils apportés durant la rédaction de ce mémoire.

Je tiens également à remercier Pr. Charles-André Fustin, Pr. Olivier Riant et Pr. Alexandru Vlad d'avoir accepté de faire partie de mon jury. Merci pour le temps accordé à la lecture de mon mémoire.

J'aimerais exprimer mes remerciements à toutes les personnes de l'aile B2, trop nombreuses pour les citer, pour leur accueil et leur aide.

Je remercie Laurianne Roland, mon binôme depuis BAC 1, pour son soutien et les bons moments durant ces années.

Finalement, un grand merci à toutes les personnes qui m'ont toujours soutenu de près ou de loin durant ces années d'études.

Abstract

Over the next few decades, our society will be forced to transition to more carbon-neutral methods of energy production. The problem with this transition is that storage systems are not sufficiently developed to meet current energy needs. The solution that offers the best energy density is the Lithium metal battery. However, Lithium metal batteries require improvements in safety. The search for optimisation of all-solid-state Lithium metal batteries is at the heart of this study, and more specifically the development of solid polymer electrolytes. The major challenge is to achieve good ionic conductivity at room temperature for solid polymer electrolytes. The advantages linked to the use of such electrolytes are potentially numerous: mechanical strength, resistance to flammability, limitation of dendrite formation. However, they suffer from poor ionic conductivity, especially at room temperature. With the hope of improving their conductivity, liquid crystals are added to solid polymer electrolytes to form a hybrid material. Indeed, liquid crystals have the property of forming self-organized mesophases that may contain channels that facilitate the passage of ions through the material. The objective is to identify the hybrid material giving an improved conductivity close to that of liquid electrolytes at room temperature for their application in the field of solid electrolytes.

This work started with the synthesis of monomers, liquid crystals, and polymers. Their thermal properties were characterised. Then, different solid polymer electrolytes were made and analysed by electrochemical impedance spectroscopy. For one of the investigated systems, the conductivity is of the order of 10^{-3} S cm^{-1}, which agrees with the objective of this study. An analysis of the thermal and electrochemical stability of the solid polymer electrolytes was performed. A catholyte with the selected solid polymer electrolyte was formed and integrated in an all-solid-state battery. This catholyte proved to be effective despite a significant capacity loss with the solid polymer electrolyte. In addition to the achieved goal, several ways of improvement are envisaged for future work.

List of abbreviations

AIBN	Azobisisobutyronitrile
CLC	Calamitic liquid crystal
CTA	Chain transfer agent
DLC	Discotic liquid crystal
DMC	Dimethyl carbonate
DMF	Dimethylformamide
DMSO	Dimethylsulfoxide
DP	Degree of polymerisation
DSC	Differential scanning calorimetry
e.g.	Example given
EC	Ethylene carbonate
EIS	Electrochemical impedance spectroscopy
etc.	Et caetera
FID	Free induction decay
FR	Free radical
GF	Glass fiber
GPC	Gel permeation chromatography
GPE	Gel polymer electrolyte
HBC	4'-(hexyloxy)-[1,1'-biphenyl]-4-carbonitrile
HPLC	High performance liquid chromatography
HRMS	High-resolution mass spectrometry
ICE	Inorganic ceramic electrolyte
i.e.	In essence
LC	Liquid crystal
LFP	Lithium iron phosphate
Li-SSB	Lithium solid-state battery
LIB	Lithium ion battery
LiFSI	Lithium bis(fluorosulfonyl)imide
LiTFSI	Lithium bis(trifluoromethanesulfonyl)imide

LMB	Lithium metal battery
LSV	Linear sweep voltammetry
M1	(2-oxo-1,3-dioxolan-4-yl)methyl methacrylate
M2	2-((1,3,2-dioxaborepan-2-yl)oxy)ethyl methacrylate
M3	Poly(ethylene glycol) methyl ether methacrylate
MALC	4'-((6-hydroxyhexyl)oxy)-[1,1'-biphenyl]-4-carbonitrile
MBBA	*p*-methoxybenzylidene *p*-butylaniline
Mn	Number average molar mass
Mw	Weight average molar mass
NMR	Nuclear magnetic resonance
PDI	Polydispersity index
PEG	Poly(ethylene glycol)
PEO	Poly(ethylene oxide)
PMMA	Poly(methylmethacrylate)
POM	Polarized optical microscope
RAFT	Radical addition fragmentation chain end transfer
RT	Room temperature
SCE	Solid composite electrolyte
SEI	Solid electrolyte interphase
SEM	Scanning electron microscopy
SPE	Solid polymer electrolyte
SSE	Solid-state electrolyte
Td (5 %)	Degradation of temperature with a loss of 5 % weight
TEA	Triethylamine
TGA	Thermogravimetric analysis
TLC	Thin layer chromatography
TS	Teflon spacer
vs.	Versus

Table des matières

I. Introduction

The industrial revolution developed further the human society by producing goods in big quantities. However, from an environmental point of view, this revolution has led to an increase in greenhouse gas emissions. These emissions are partly responsible for global warming. The consequences of these emissions will not only be limited to climate change but also to our health, biodiversity, *etc*. To limit the impact of this dangerous global warming, the European Union aims to reduce greenhouse gas emissions by 55 % by 2030. If this target is met, carbon neutrality will be possible by 2050. This objective, combined with the depletion of natural resources, requires a rethink of energy production and consumption. Indeed, the energy production sector is the main source of carbon emissions in the world. The solution is the energy transition to greener energy production, energy supplied by renewable sources such as photovoltaic panels, wind turbines, hydroelectric power stations, *etc*. The problem we face now is that storage technology is not sufficiently developed to allow for energy storage. Storage is one key factor in this energy transition to meet the supply and demand of energy as we know it today. Indeed, the problem with greener energy production is its dependence on weather conditions. The development of reversible storage systems has quickly emerged as the solution to this intermittency of energy sources. The automobile sector is also a source of carbon, and the European Union's decision to ban the sale of combustion cars by 2035 is also forcing improvements in hybrid and electric cars. Lithium metal batteries could have a major impact on electric/hybrid cars because of their energy density. This means that for the same weight and space as other battery types, Lithium metal batteries can store and therefore deliver more energy. This improvement would allow the car to travel more kilometres before needing to be recharged. Although these batteries are promising, they still need to be improved because this type of battery presents safety risks. Liquid batteries present many hazards such as off-gassing, leakage of organic solvents and dendrite formation. These hazards lead to a risk of fire. In order to reduce this risk, the use of solid-state batteries is being considered to avoid the presence of organic solvents and the formation of dendrites. Currently, solid-state polymer batteries are manufactured with a solid polymer electrolyte. The disadvantage of these electrolytes is their low ionic conductivity at room temperature. This study focuses on improvement of ionic conductivity in solid polymer electrolytes by adding liquid crystals for Lithium metal batteries. Liquid crystals are interesting because they

can form channels allowing the passage of ions in a material. This facilitated passage would allow for improved ionic conductivity in solid polymer electrolytes. They could also prevent the growth of dendrites through their thermal transition. Indeed, during their transition to the crystalline phase, the growth of dendrites would be hindered while during their transition to the isotropic state dendrites could be detached. The objective of this master thesis is to prove that liquid crystals improve the ionic conductivity by reaching an ionic conductivity close to that of liquid electrolytes. To accomplish this, a "hybrid" material will be produced in this study. This "hybrid" material will be composed of a mixture of a solid polymer electrolyte, a lithium salt, and a liquid crystal.

In chapter 1 of this work, a theoretical background is presented for a better understanding of this evaluation. In chapter 2, the experimental part is gathered; instruments, reagents, and methodology. Chapter 3 presents the results of the performed experiments and their discussion. Finally, the last chapter summarizes the results and gives an outlook for further experiments.

II. Theorical background

Due to its scientific nature, the current study will inevitably refer to conceptual and technical notions. It is therefore appropriate to begin by recalling and clarifying knowledge. This is the objective of this theoretical background.

1. Batteries

Batteries are devices that can store chemical energy and convert it to electrical energy. They are composed of many cells connected to achieve the desired capacity.[1] The focus of this entire work will only be put on secondary batteries.

1.1. Primary vs secondary batteries

Unlike primary batteries which can only serve as energy generator, a secondary battery is a rechargeable electrochemical generator. It can act as an energy accumulator when fed by an external electrical energy source: one says then that the battery works in charging mode. Alternatively, it can serve as an energy generator providing energy for any external electrical use: the device is in that case discharging the energy it is producing. The battery relies on a redox reaction. The rechargeability occurs when this redox reaction is reversible.[2, 3.]

1.1.1. Components and working principle

A cell can be oversimplified as two electrodes in an electrolyte. These electrodes are connected by an external circuit. The electrodes are the places where oxidation or reduction chemical reactions are occurring depending if the battery is being charged or discharged. The electrons can move through an external circuit and produce electrical work. The material of the electrodes is deposited on a current collector together with a binder. The collector is aluminum for the cathode and copper for the anode. The collectors have the role of transporting the electrical charges. The resistance of the collectors must be as low as possible to avoid energy losses. The electrolyte is an ionic conducting material that allows ions to move. If a liquid electrolyte is used, the separator isolates the anode and compartments and thus prevents short circuits in the cell. If solid electrolyte is used no extra separator is needed since the electrolyte acts simultaneously as separator preventing the electrodes to come in contact.[2, 3.] The basic set up and the components of a cell are shown in figure **1**.

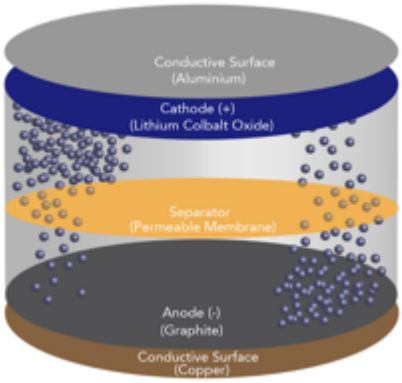

Figure 1: Representation of different components of a coin cell. Ref. [4]

During charging and discharging the electrodes undergo redox reactions. As the reactions are reversible, the species oxidised during discharge must be reduced during charging. When the battery is discharged, the anode is oxidised and the electrons flow through the external circuit to the cathode. The flow of electrons provides an electric current that can be used to do electrical work. To balance the charges between the electrodes, a displacement of ions takes place. When charging the cell, by supplying external energy, the reactions can be reversed.[2]

1.1.2. Characterisation

The theoretical voltage (*U*) of a battery is the potential difference between the two electrodes. This value is expressed in volts (V).[5] $U = cathode\ potential\ - anode\ potential$ (1)

The theoretical capacity (C_{theo}) expressed in Coulomb (C) is the maximum electrical charge that can be stored in the cell. Most often expressed in Ampere hours (Ah).[5]

The theoretical energy of a battery is the total energy that can be stored. This value is expressed in Watt hours (Wh).[5] $E_{theo} = C_{theo} \times V$ (2)

The power of a battery (P) is the energy transfered per unit of time. It is expressed in Watt (W). $P = V \times I$ (3)

The C-rate is a function of the rate at which a cell is discharged relative to its maximum capacity. If the C-rate is 1C, this means that it requires 1 hour for the cell to be discharged.[2]

The ionic conductivity (σ) expresses how fast ions can move from one side of the cell to the other. It is expressed in Siemens per centimetre (S cm^{-1}) and is calculated by the following formula, $\sigma = \sum_i n_i \times \mu_i \times z_i \times e$ (4)

It depends on ion mobility (μ_i), free ion number (n_i), valence of ionic species (z_i) and the unit charge (e). It should not be confused with electrical conductivity, which is the movement of electrons. Ionic conductivity is considered acceptable when it is greater than 10^{-4} S cm^{-1} at

room temperature (RT). For lithium batteries, only the conductivity of the lithium ions is measured.[2, 6.]

The transference number (t_i) of lithium ions is the number of moles of lithium transferred during the migration.

$$t_i = \frac{I_i}{\sum_i I_i} \quad (5)$$

If the transference number is close to 1, this is the ideal case, meaning that only lithium ions are moving, wich are usually faster than the corresponding anion.[2, 7.]

1.2. Lithium ion batteries

In Li-ion batteries (LIBs), the anode is composed of graphite, the cathode is a compound containing lithium, which is the source of lithium ions, such as Li_xCoO_2 or $LiPF_6$. During discharge, the lithium in the anode is released into the electrolyte, while the electron produced passes through the external circuit until the potential difference between electrodes is equilibrated. To balance the charges, a lithium cation goes inside the cathode and forms Li_xCoO_2. During charging, the reverse reaction takes place and thus Li^+ is intercalated in graphite.[2, 5, 8.] The charging/discharging principle is shown in the figure **2**.

Reaction inside: $Li_xCoO_2 \longrightarrow Li_{1-x}CoO_2 + x\ Li^+ + x\ e^-$

$C + 6\ Li^+ + 6\ e^- \longrightarrow Li_6C$

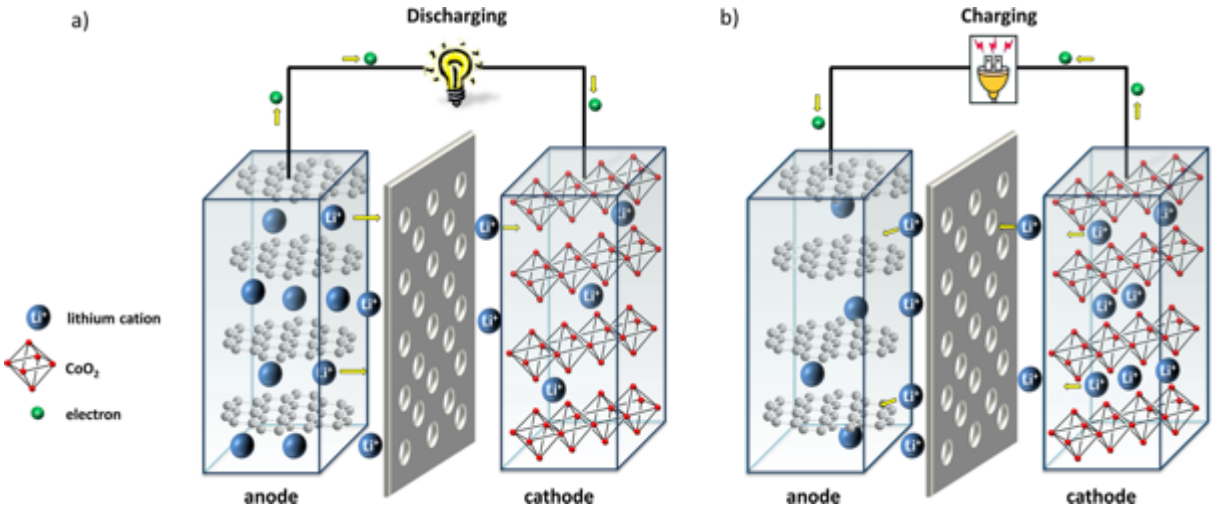

Figure 2: Representation of discharging (a) and charging (b) of a Li-ion battery. Represented from Ref. [5]

On the surface of the anode, we have a layer of solid electrolyte interphase (SEI), which is composed of products of the irreversible decomposition of the electrolyte in contact with the electrodes. The SEI is formed during the first charging of the battery. This layer allows the

passage of lithium cations while the passage of electrolyte is blocked in order to avoid further decomposition. Figure **3** illustrates the principle of SEI.[2]

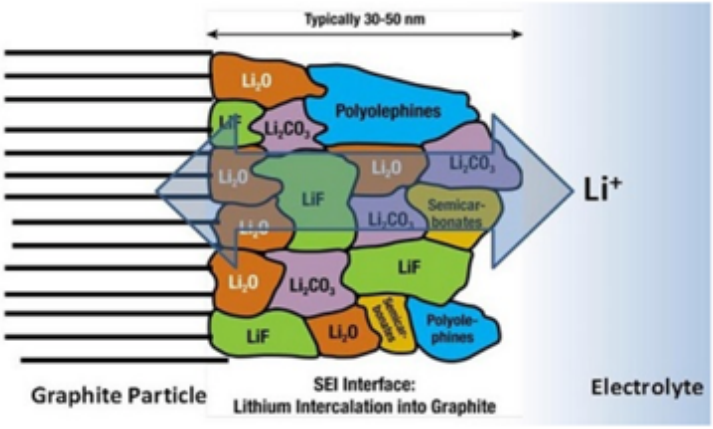

Figure 3: Illustration of SEI on the anode in Li-ion battery. Represented from Ref. [2]

1.3. Lithium metal batteries

Li-metal batteries (LMBs) work in a similar way like Li-ion batteries. The main difference is that the anode is made of lithium metal. This technology is more promising since the theoretical specific capacity of lithium is almost 10 times higher than that of graphite. LMBs show the best performance between energy density and mobility. They are promising because of their low volume-to-weight ratio as lithium is lighter and has a low density than other metals. Lithium has a redox potential of -3,04 V *vs*. the standard hydrogen electrode. Together with a transition metal, *e.g.*, cobalt or manganese, high voltage potential (> 4 V), high energy and power densities are achieved.

When using liquid electrolytes, during charging the lithium cations can deposit irregularly on the anode, forming spiky microstructures called dendrites. The figure **4** is a picture taken by scanning electron microscope (SEM) showing the growth of dendrites on the surfaces of the anode. The formation of dendrites displaces the SEI, causing irregularities. These dendrites cause a decrease over time in the capacity of the battery because some dendrites are no longer connected electronically to the anode and therefore do not participate in the redox reactions. A short circuit may occur when the dendrites continue growing until they reach the cathode, which presents a safety problem because a large amount of energy is released fast and uncontrolled. Therefore, a lot of research is being done to control or suppress the growth of lithium dendrites. Solid polymer electrolyte is a promising technology to slow down or suppress the growth of lithium dendrites.[2, 9, 10, 11.]

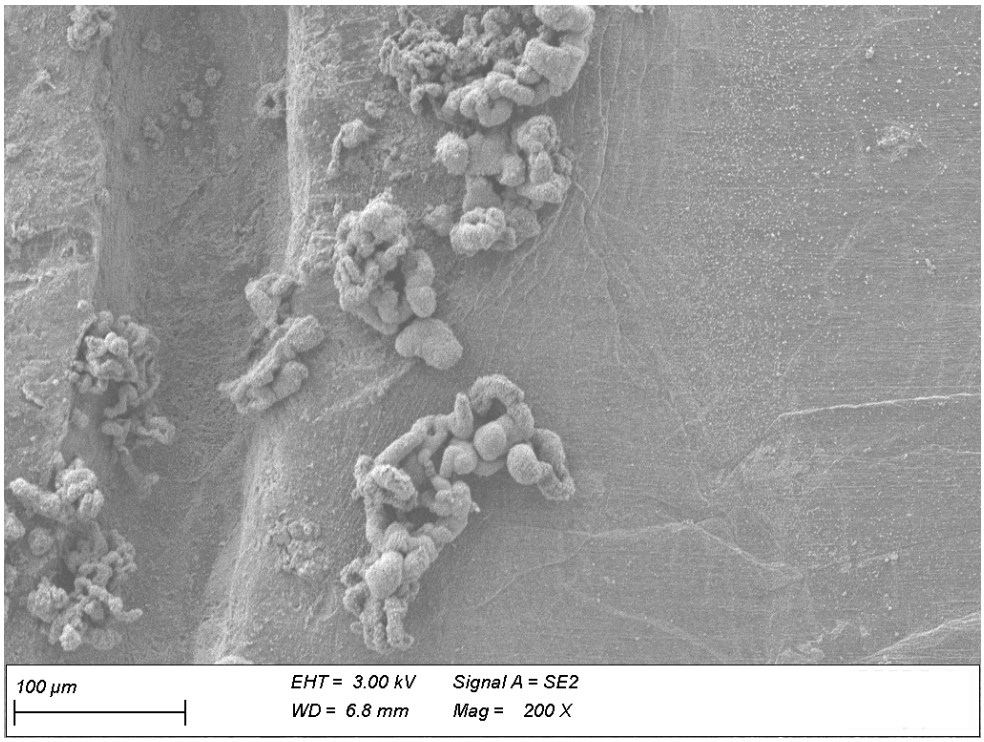

Figure 4 - Picture of dendrites growth on the anode surface. This image is taken by SEM (I. Álvarez Moisés)

1.4. Lithium solid-state batteries

LIBs technology is based on liquid electrolytes and faces safety issues related to the use of toxic and flammable solutions. The solid-state battery is a more interesting approach as it has many advantages. Indeed, solid-state electrolytes (SSEs) can be coupled with a lithium metal anode, allowing a higher energy density, lower risk of thermal runaway and a reduction of dendrite formation. In addition, by avoiding the use of liquid, the risk of leakage and self-ignition is reduced. The development of Li-solid-state batteries (Li-SSBs) is not only limited to the development of new SSEs but also to the cathode. Concerning the SSEs, they must both conduct Li^+ ions and be electrically insulating. The use of SSEs makes it possible to use it as separator, as it must act as a physical barrier to prevent contact between the electrodes. SEs will be discussed in detail in chapter 2.2.2. For the cathode part, the main challenge is the formation of solid-solid interfaces. Poor interfacial contact is the main source of charge accumulation and mass transfer resistance between the electrode materials, the SSE, and the current collector. In order to improve this interfacial contact, a catholyte is made, which consists of a mixture of redox material, SSE and conductive additive (carbon).[8, 12.] The figure **5** schematically represents a Li-SSBs with a catholyte.

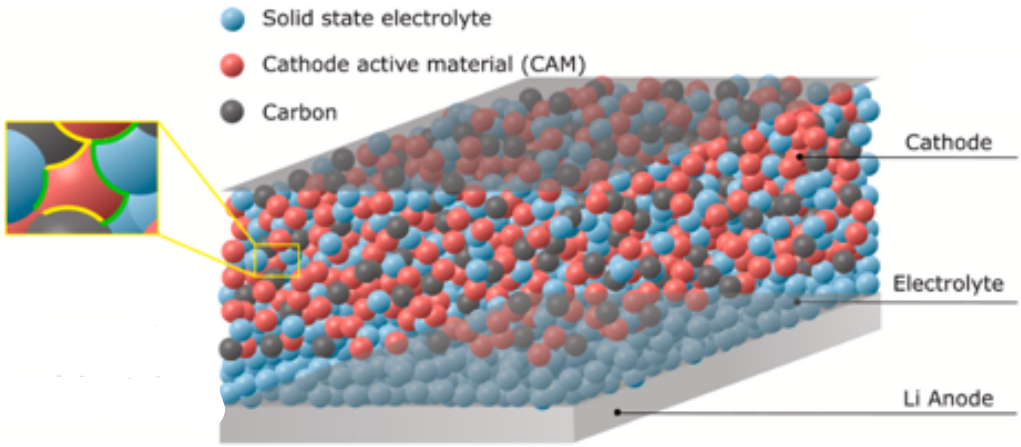

Figure 5: Schematic representation of Li-SSB with lithium as anode. Represented from Ref. [8]

2. Electrolytes

The electrolyte must be chemically inert so that it does not any secondary reactions in the cell components, but still form a SEI. Electrolytes can be enriched with additives giving better properties, *e.g.* fire-retardant, better formation of SEI, improved ionic conductivity and increased electrochemical stability window.

2.1. Performances characteristics

The characteristics defined below will be represented in different diagrams in the section 2.2. This will clarify the properties of the different electrolytes. As discussed before the ionic conductivity is the movement of ions from one battery compartment to another. It should not be confused with electrical conductivity. Interfacial contact is the communication between the electrolyte and the electrodes. Thermal stability defines the ability of a compound to remain stable even at high temperatures. Flexural strength is the ability to resist bending deformation. Electrochemical stability is the voltage range in which the material is stable.[2, 13.]

2.2. Types of electrolytes

2.2.1. Liquid electrolytes

Liquid electrolytes are composed of a lithium salt dissolved in a solvent or mixture of solvents. They have an ionic conductivity of 10^{-2} - 10^{-3} S cm^{-1} at RT and are the best currently available in term of conductivity for LIBs. Commercially available LIBs work with $LiPF_6$ dissolved in ethylene carbonate (EC) and dimethyl carbonate (DMC) which shows a conductivity of 10^{-2} S cm^{-1} at 20 °C. Liquid electrolytes also have good interfacial contact with the electrodes decreasing the internal resistance and overpotential. Liquid electrolytes have excellent fluidity which allows them to integrate well with the electrode material and form the SEI.[14]

Figure **6** shows an illustration of a cell with liquid electrolyte (left) and the characteristics of the liquid electrolyte (right).

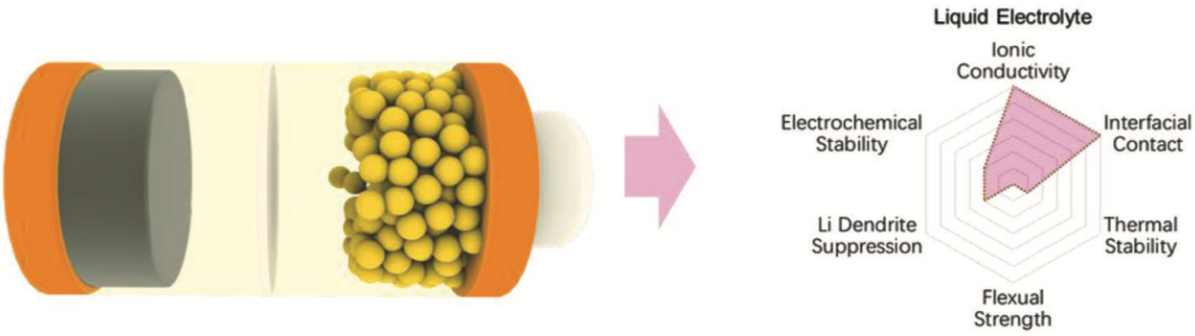

Figure 6: Illustration of a cell using liquid electrolytes (right) and a chart of its most relevant properties (left). Represented from Ref.[14]

In the figure **6**, an imbalance in performance can be seen, with ionic conductivity and interfacial contact peaking but other characteristics being very low.

2.2.2. Solid-state electrolytes

2.2.2.1. Solid polymer electrolytes

Solid polymer electrolytes (SPEs) have a polymer matrix that can solvate lithium salts. The most commonly used lithium salts are lithium bis(trifluoromethanesulfonyl)imide (LiTFSI), lithium bis(fluorosulfonyl)imide (LiFSI) and $LiClO_4$ because they have good electrochemical and thermal stability and high solubility. SPEs have the advantage of a good mechanical flexibility thanks to the polymeric matrix properties. These advantages make them ideal candidates for Li-metal batteries. But they have a lower ionic conductivity compared to liquid electrolytes at RT (10^{-4} - 10^{-6} S cm^{-1}). This limits their use in current lithium battery applications.[14, 15.]

Figure **7** shows an illustration of a cell with solid polymer electrolyte (left) and the characteristics of the solid polymer electrolyte (right).

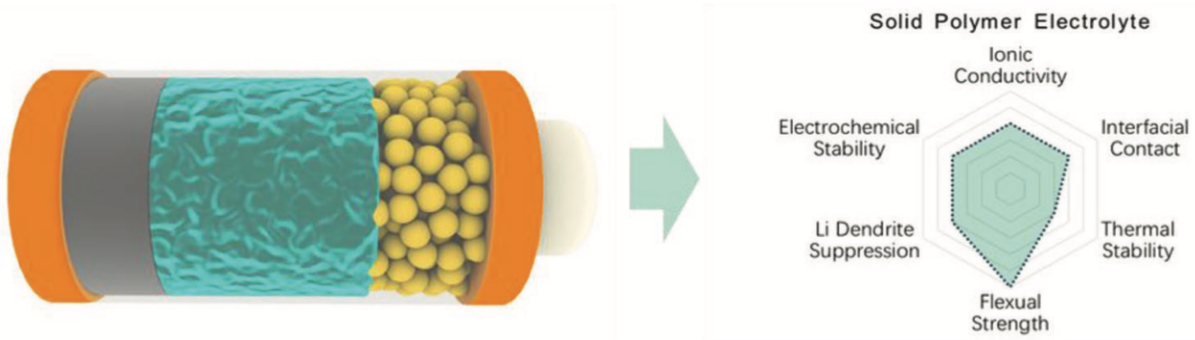

Figure 7: Illustration of a cell using SPE (right) and a chart of its most relevant properties (left). Represented from Ref.[14]

It can be seen from the figure **7** that the domains are more balanced than for liquid electrolytes.

The most widely used polymer is based on polyethylene oxide (PEO) as host matrix. It can dissociate the lithium salt. This characteristic is due to the electron-donor oxygen atoms, which contribute to the coordination of Li^+ with a composition of three ether oxygen per lithium ion. The conduction of the ions is based on two phenomena, as can be seen from figure **8**, the oxygen-assisted hopping of Li^+ ions and the local movement of polymer chain segments that create new coordination sites.[1, 6 ,7.]

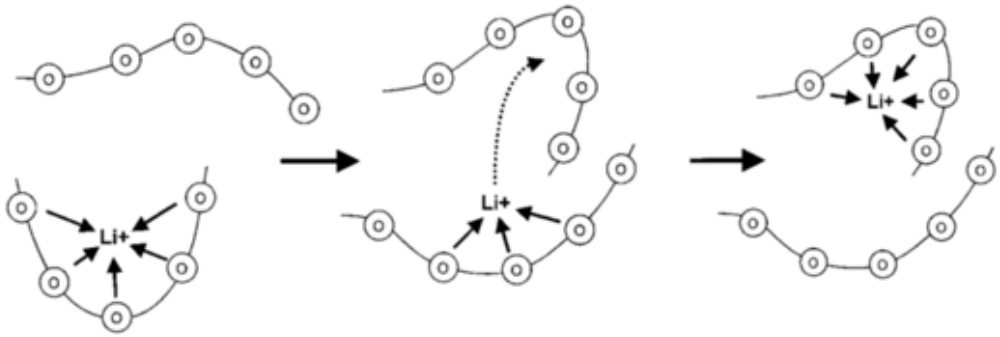

Figure 8: Oxygen-assisted diffusion mechanism of lithium ions in PEO. Represented from Ref. [1]

Its conductivity is of the order of 10^{-7} S cm^{-1} at RT due to its semi-crystalline form. Therefore, these batteries operate at temperatures above 60 °C. Unfortunately, at 60 °C, PEO loses its mechanical properties.[8]

2.2.2.2. Gel polymer electrolytes

Gel polymer electrolytes (GPEs) are formed by polymers networks in which the liquid electrolyte is enclosed. Their conductivity is better than SPEs, 10^{-3} S cm^{-1} at RT. As the liquid electrolyte is in the polymer matrix, the risk of leakage of organic solvents is reduced. This type of electrolyte has the properties of both SSEs and LEs with good mechanical properties, good interfacial contact and can be used as a separator.[16, 17, 18.]

2.2.2.3. Inorganic ceramic electrolytes

The inorganic ceramic electrolytes (ICEs) have a higher ionic conductivity than the solid polymer electrolytes, it is around 10^{-2} S cm^{-1} at 300 °C. However, they have a low flexibility and poor interfacial contact which makes them unreliable for use in batteries.[14]

Figure **9** shows an illustration of a cell with inorganic ceramic electrolyte (left) and the characteristics of the inorganic ceramic electrolyte (right).

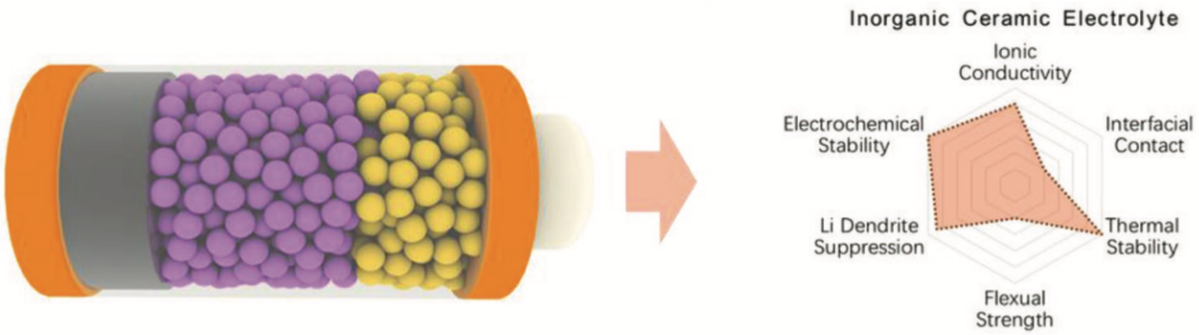

Figure 9: Illustration of a cell using ICE (right) and a chart of its relevant properties (left). Represented from Ref.[14]

The main problems with ICEs are their interfacial contact and their flexural strength which is low as can be seen in the figure **9**.

2.2.2.4. Solid composite electrolytes

Solid composite electrolytes (SCEs) are currently the best candidates among solid electrolytes. They consist of a host polymer matrix and inorganic nanoparticles. They are hybrids and therefore combine the properties of SPEs and ICEs. The conductivity is 10^{-3} - 10^{-4} S cm^{-1} at RT.[14, 18.]

Figure **10** shows an illustration of a cell with solid composite electrolyte (left) and the characteristics of the solid composite electrolyte (right).

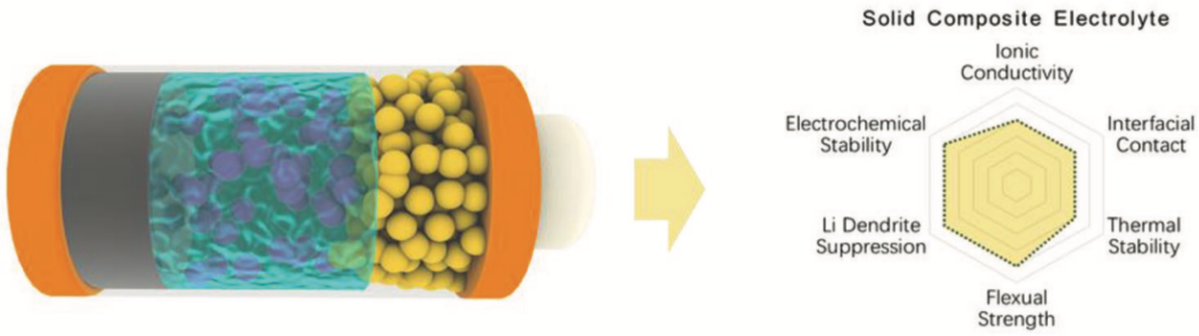

Figure 10: Illustration of a cell using SCE (right) and a chart of its relevant properties (left). Represented from Ref.[14]

It can be seen from figure **10**, the performance ranges are almost perfect for this type of solid electrolyte, which reinforces the fact that they are the best candidates for batteries. But the conductivity is highly dependent on the weight fractions of the ceramic and the surface area of the fillers.[16]

3. Polymer chemistry

3.1. Definitions and concepts

3.1.1. Polymers

A polymer is a macromolecule resulting from the assembly of covalently bonded repetitive molecules. These molecules are called monomers. The conversion of monomer into polymer is called polymerization, as show in figure **11**. When between two and a few dozen monomers are combined, an oligomer is formed.[19]

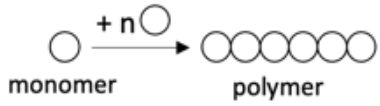

Figure 11: Schematic representation of polymerisation.

There are mainly three classes of polymers:

- Natural polymers which can be found in nature, sometimes with specific molar mass and a dispersity index of 1 (*e.g.* proteins).
- Artificial polymers which are the product of chemical modification of natural polymers.
- Synthetic polymers which are produced in industrial quantities and present typically a dispersity index of > 1.

3.1.2. Monomers

A monomer has one unsaturation or two functional groups. An unsaturation is the presence of double or triple covalent bonds between adjacent carbon atoms. A double bond or an aromatic ring counts as one unsaturation, while a triple bond counts as two unsaturations. A functional group is an atom or group of atoms that have the same physical and chemical properties whenever they are present in the molecule. An example of a functional group is an alcohol (-OH).[20] The figure **12** shows some examples of monomers.

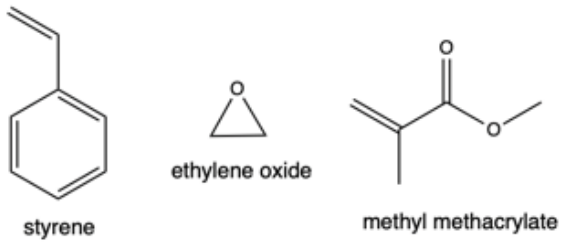

Figure 12: Structure of some monomers; styrene, ethylene oxide and methyl methacrylate.

3.1.3. Characteristic values

The degree of polymerisation (DP) is the total number of monomers in the polymer. The molar mass of a polymer is characterised by the number average molar mass (Mn) and by the weight average molar mass (Mw). The average is used because not all chains have the same length.[21] The Mn is defined as the sum Σ_i of all the molar masses M_i of the i families of species present in the system, each affected by its proportion in number, *i.e.*

$$M_n = \Sigma_i M_i \frac{N_i}{\Sigma_i N_i} = \frac{\Sigma_i N_i M_i}{\Sigma_i N_i} \quad (5)$$

The Mw is defined as the sum Σ_i of all the molar masses M_i of the i families of species present in the system, each affected by its proportion by mass, *i.e.*

$$M_w = \Sigma_i M_i \frac{N_i M_i}{\Sigma_i N_i M_i} = \frac{\Sigma_i N_i M_i^2}{\Sigma_i N_i M_i} \quad (6)$$

Long polymer chains have a higher weight than short chains and thus Mw is larger than Mn. The ratio of these two average molar masses is the polydispersity index (PDI), as you can see on the following formula,

$$PDI = \frac{M_n}{M_w} \quad (7)$$

The PDI gives a value for the molar mass distribution. If the PDI equals 1 means that all the chains have the same length.[21]

3.1.4. Homopolymers and copolymers

There are two types of polymers depending on the polymerisation reaction: homopolymers and copolymers. The properties of homopolymers and copolymers are different. Homopolymers consist of only one type of monomer while copolymers have at least 2 different monomers. In this case the monomers are called comonomers.[19, 22.] Copolymers are divided into four groups:

- Statistical copolymers have a statistical distribution of monomers, as shown in figure **13**. These copolymers are also called random copolymers.[22]

Figure 13: Schematic representation of a statistical copolymer.

- Alternating copolymers where monomer A (MA) and monomer B (MB) alternate regularly where the MA and MB are 2 differents monomers,[22] as shown in figure **14**.

Figure 14: Schematic representation of an alternating copolymer.

- Block copolymers are made by joining blocks of MA and blocks of MB, as shown in figure **15**. The number of blocks is not necessarily equal.[22]

Figure 15: Schematic representation of a block copolymer.

- Graft copolymers have a main chain consisting of MA onto which the side chain MB is grafted, as shown in figure **16**. The main chain is the backbone and the side chain is called the branch.[22]

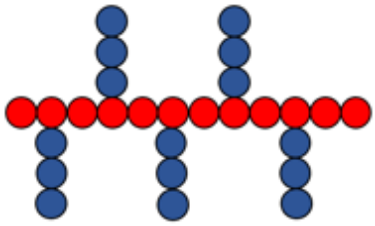

Figure 16: Schematic representation of a graft-copolymer.

3.2. Synthesis of polymers

During the polymerisation process, two types of growth can be distinguished according to their mechanism: step-growth and chain-growth polymerisation.

3.2.1. Step-growth polymerisations

Step-growth polymerisations are generally condensation reactions. The monomers are bi- or multi-functional. The monomers form short chains called oligomers which then combine into long chains. All molecules present are active and react with any other molecule. For example, a dimer (*x*) can react with a monomer (*y*) to form a trimer (*x+y*) : *x*-mer + *y*-mer = *x+y*-mer. The figure **17** is a schematic representation of a step-growth polymerisation. If the monomer has more than two functional sites, cross-linked and branched polymers can be synthetized.[19, 21.]

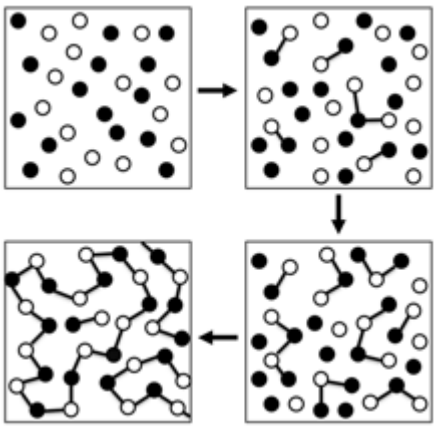

Figure 17: Schematic representation of a step-growth polymerisation. Represented from Ref.[23]

This type of growth requires high conversion rates to obtain high molecular weight polymers. The advantages are the absence of initiator and termination reactions.

3.2.2. Chain-growth polymerisations

Chain polymerisation reactions are generally addition reactions. The monomer carries an unsaturation (or is a cyle). For initiation, the initiator first generates an active species. This active species (cation, radical or anion) reacts with the monomer to form the propagating species. This can grow via addition of monomer to the active part at the end of the chain. The growth of the chain is deactivated either by irreversible termination or transfer reaction.[19, 21.] The figure **18** shows the schematic representation of a chain-growth polymerisation.

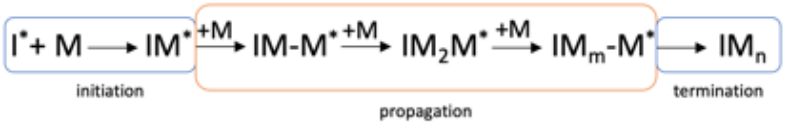

Figure 18: Schematic representation of a chain-growth polymerisation.

Four types of chain polymerisation can be deduced according to the nature of the active center, they are called anionic, cationic, coordinative and radical polymerisation. We will only adress radical polymerisation in the following point.

3.2.2.1. Free radical polymerisation

During the initiation, the radical active center is formed by degradation of the initiator. The addition of the active center on the monomer is the last step of the initiation. The growth of the chain by successive addition of monomer is the propagation step. The last step is the termination which can be done either by transfer or by recombination. Figure **19** summarizes these different steps.[19, 21.]

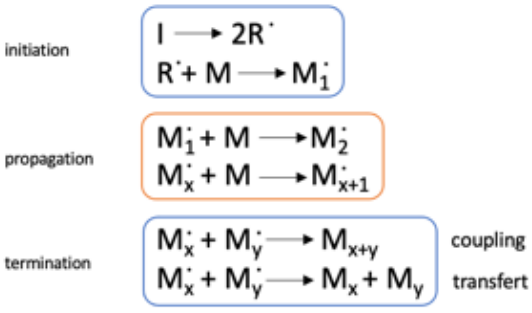

Figure 19: Mechanism of FR polymerisation.

3.2.2.2. Radical addition fragmentation chain end transfer polymerisation

The radical addition fragmentation chain end transfer (RAFT) it is a controlled polymerisation. The term "controlled" is used for polymerisations that result in polymers with well-defined characteristics. This type of polymerisation avoids high dispersity index polymers because the initiation stage is rapid compared to the propagation and the transfer or termination reactions tend to be minimised. The RAFT method allows radical polymerisation to be carried out on a wide range of monomers in aqueous media at lower temperatures than other radical polymerisation techniques. This method requires a chain transfer agent, CTA. The structure of a CTA is shown in figure **20** It must be able to react with a chain carrier in a reaction in which the original carrier chain is deactivated and a new chain is generated.[24, 25.]

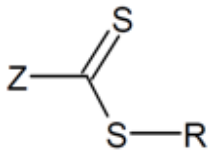

Figure 20: Structure of CTA.

The R and Z groups must stabilise the radical formed after the addition step but also promote the fragmentation of the intermediate by being a good leaving group. The R group must also be a re-initiator depending on the monomer used. The figure **21** shows the reaction mechanism of RAFT with two equilibriums of addition-fragmentation. [21, 24.]

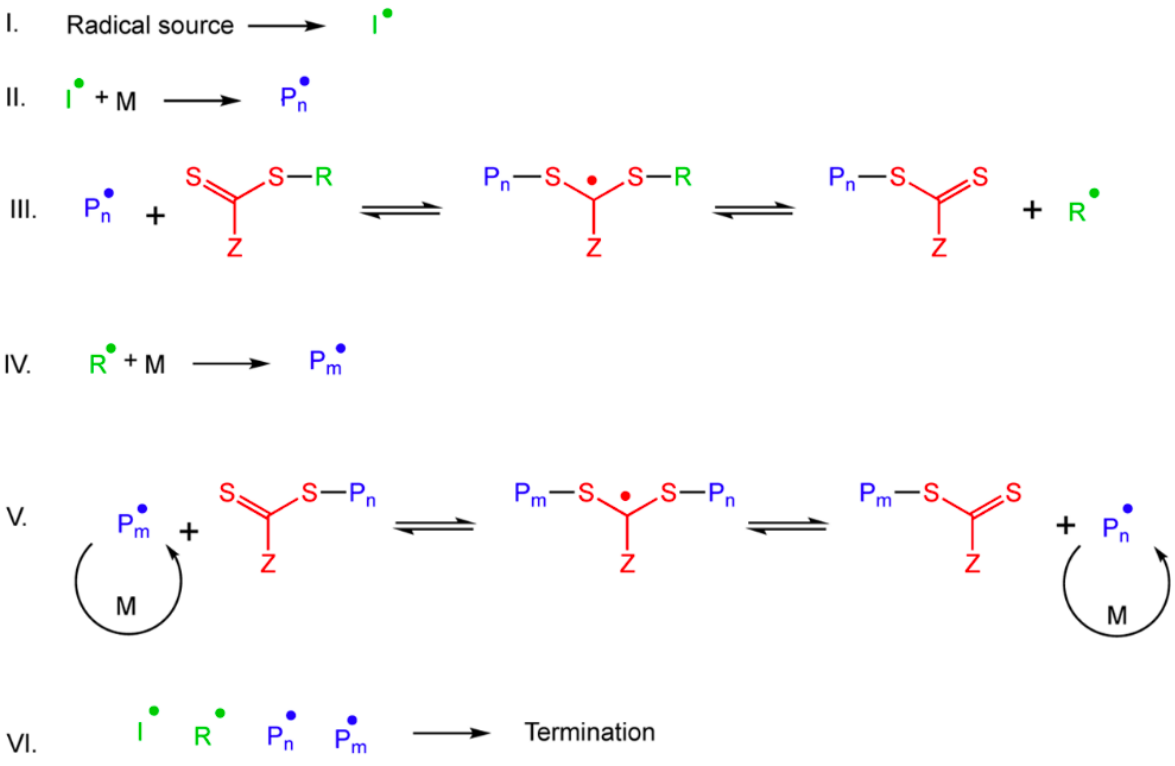

Figure 21: Mechanism of RAFT polymerisation. Represented from Ref.[24]

The initiator is usually azobisisobutyronitrile (AIBN). The initiator is degraded to a radical initiator (step I. in figure **21**), which reacts with a monomer to form a propagating species (II.). During chain transfer, the propagating species reacts with the CTA via an addition reaction forming a radical intermediate (III.). This intermediate is then fragmented to release a new radical that can re-initiate polymerisation (IV. and V.). The termination step is realised by combination of different propagating species or by disproportionation (VI.). As the CTA is more than the initiator, it is the amount of CTA involved that determines the number of chains produced. The number of radical chains that develop corresponds to the number of initiators introduced. The polymeric chains are terminated by thiocarbonyl-thio groups and this can have undesired consequences such as giving a colour for the polymer. This colour can be removed by organic chemistry reactions: *e.g.* addition of NaOH, $NaBH_4$ or NR_3. [21, 24.]

4. Liquid crystals

Liquid crystals (LCs) are a special state of matter that combines the properties of an isotropic liquid with those of a crystalline state. The high order typical of the solid crystalline state is reduced so that the material has a degree of freedom to flow. This state is defined as a

mesophase and molecules with those characteristics are called mesomorphic compounds. Mesogenic groups are moieties that can integrate into a molecule to give it liquid crystal behaviour. These moieties are usually aromatic rings. Liquid crystals have a rigid core and a flexible tail. There must be a balance between rigidity and flexibility. If the liquid crystal is too flexible, then there is no more orientational order and if the liquid crystal is too rigid then there is a direct phase change from solid to liquid. Liquid crystals are divided into three categories: thermotropic, lyotropic and metallotropic mesophases. Thermotropic phases can be observed when the temperature varies. For lyotropic phases, however, the addition of solvent is necessary. Lyotropic phases are always solutions. Some compounds can exhibit both thermotropic and lyotropic mesomorphism, they are called amphotropic liquid crystals. Metallogens consist of at least one metal atom.[26, 27, 28.]

The nanostructures of liquid crystals allow them to form 1D, 2D or 3D channels that facilitate the selective passage of ions through the material, as you can see on the figure **22**. Indeed, the part of the LC that does not carry ions or charge is not miscible with the functional groups involved in the transport. This immiscibility results in flexible and insulating properties, which form the nanoscale channels. This capability makes them promising for use in batteries as electrolytes.[9, 29]

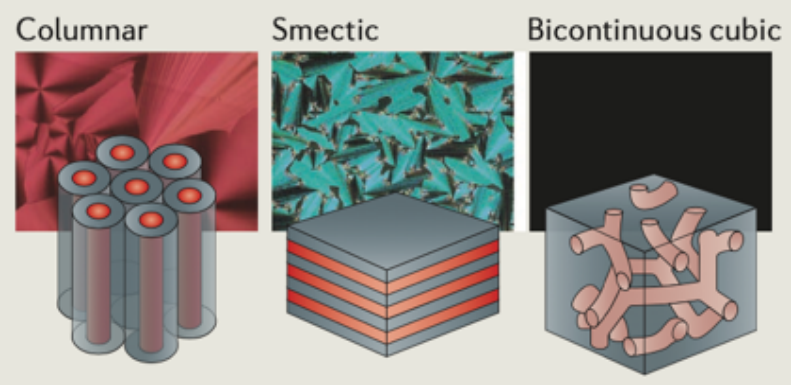

Figure 22: Schematic representation of different channels formed by LCs. Represented from Ref. [26]

4.1. Thermotropic liquid crystals

Thermotropic LC phases are obtained by heating the solid mesomorphic sample. At the melting temperature, the molecule changes from the solid to the liquid crystal phase, due to increased thermal motion. The liquid crystal molecules are positioned in an elongated rod or disk shape; they are called calamitic or discotic liquid crystals,[27, 28.] as can be seen from figure **23**.

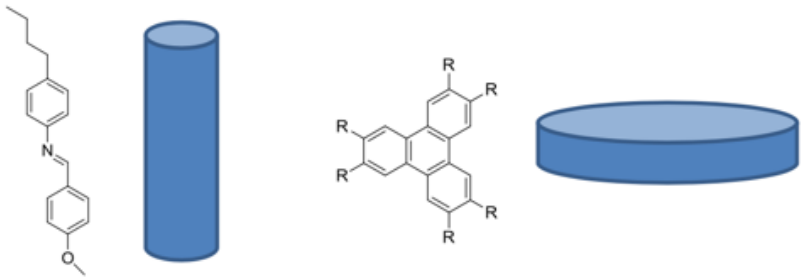

Figure 23: Illustration of calamitic (left) and discotic (right) liquid crystals. Represented from Ref.[30]

4.1.1. Calamitic liquid crystals

Calamitic liquid crystals (CLCs) are rod-shaped molecules that have one molecular axis longer than the other two. Three different classes of CLCs phases structures are recognized: nematic, smectic and cholesteric phases.[27, 28.]

Nematic: This is the simplest phase of calamitic liquid crystals. The nematic phase of a liquid crystal means that the molecules that make it up have no positional order, but they do have an orientation order. The channel formed in this nanostructure is a 2D channel.[27, 28.]

Smectic: The molecules of the smectic phase have a partial positional order, unlike the nematic phase. The orientation order present in the nematic phase is retained but, in this case, they align to form layers or planes. There are also exist a chiral smectic. There are sub-phases whose names have been assigned according to the chronological order of discovery (smectic A, smectic B, …).[27, 28.]

Cholesteric: The cholesteric phase is a nematic phase in which chiral molecules are present. This phase has a helical superstructure. From a thermodynamic point of view, there is no difference between the nematic phase and the cholesteric phase.[27, 28.]

Figure **24** shows the different structures of rod-shaped molecules as a function of increasing temperature.

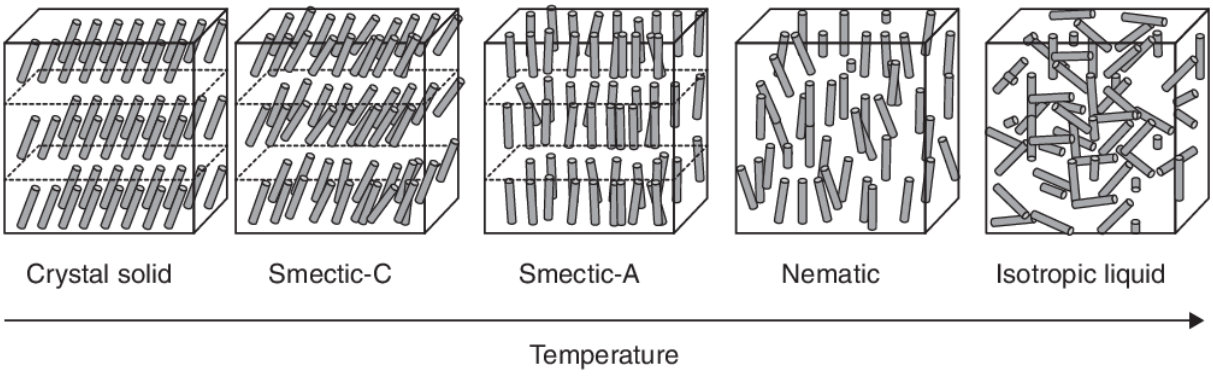

Figure 24: Different structures of rod-shaped molecule. Represented from Ref. [27]

4.1.2. Discotic Liquid Crystals

Discotic liquid crystals (DLCs) are disk-shaped molecules with one molecular axis shorter than the other two. The positional order in discotic is shown by the tendency of the molecules to arrange themselves in columns. Four different classes of DLCs phases structures are recognized: smectic, nematic, columnar, and cubic phases. The nematic and smectic phases are comparable to the calamitic mesophases.[27, 28.]

Columnar: Columnar liquid crystals are shaped like disks instead of long rods, which stack to form columns. The columns are stacked together to form a two-dimensional crystal lattice. The channel formed is this nanostructure is a 1D channel.[27, 28.]

Cubic: Cubic are most often encountered in the case of lyotropic LCs, but they also exist for thermotropic LCs. This phase consists of columns that are linked together to form a network. The channel formed in the cubic nanostructure is a 3D channel.[27, 28.]

Figure **25** shows the different structures of disc-shaped molecules as a function of increasing temperature.

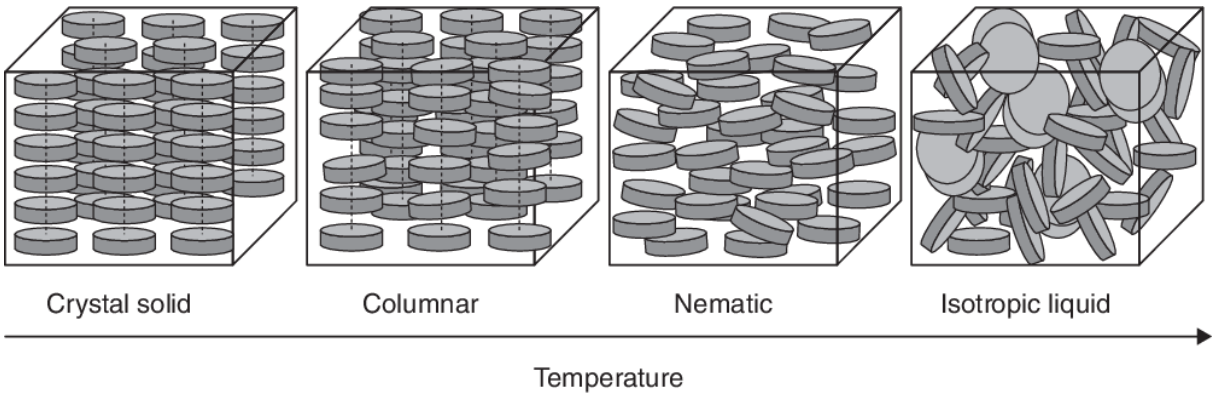

Figure 25: Different structures of disc-shaped molecule. Represented from Ref. [27]

4.2. Lyotropic liquid crystals

Lyotropic liquid crystals are generally made up of amphiphilic molecules that have a hydrophobic tail and a hydrophilic head at the other end, the solvent usually being water. These amphiphilic molecules are also called surfactants. These types of molecules are often found at interfaces. These molecules form ordered structures in polar and non-polar solvents. The solvent molecules add fluidity to the system. LCs depend on the temperature but also on the concentration of the solvent. However, this type of LC have no relevance as electrolytes in Li-metal batteries.[27, 28, 31.]

5. Instruments

5.1. Differential scanning calorimetry

Differential scanning calorimetry (DSC) is a thermal analysis to identify the phase transitions of a material. This is achieved by determining the difference in energy absorbed or released by the sample when cooled or heated compared to a reference material. Phase transitions can be endothermic (glass transition and melting) or exothermic (crystallisation).[32] The results of a DSC analysis can be plotted in a graph of the heat flux transmitted to the sample as a function of temperature. This graph is shown in figure **26**.

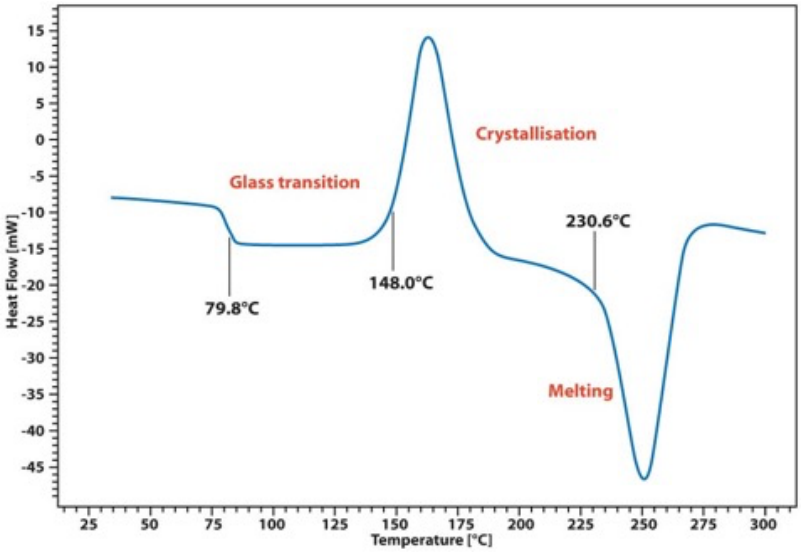

Figure 26: Typical graph of a DSC analysis. Represented from Ref.[33]

5.2. Thermogravimetric analysis

Thermogravimetric analysis (TGA) is a thermal analysis based on the variation of the mass of a sample with temperature. The purpose of this analysis is to evaluate the thermal performance of the sample. TGA is performed using a microbalance placed in an oven, which can itself be supplied with a controlled atmosphere. To perform the measurement, three parameters are important to determine: the temperature range, the rate of temperature rise and the initial mass of the sample. The results of a TGA analysis can be visualised in a graph of sample mass percentages as a function of temperature. This graph is shown in figure **27**. Prior to the degradation temperature, corresponding to a 5% mass loss of the system (Td 5%), the compound is considered stable. [32, 34, 35.]

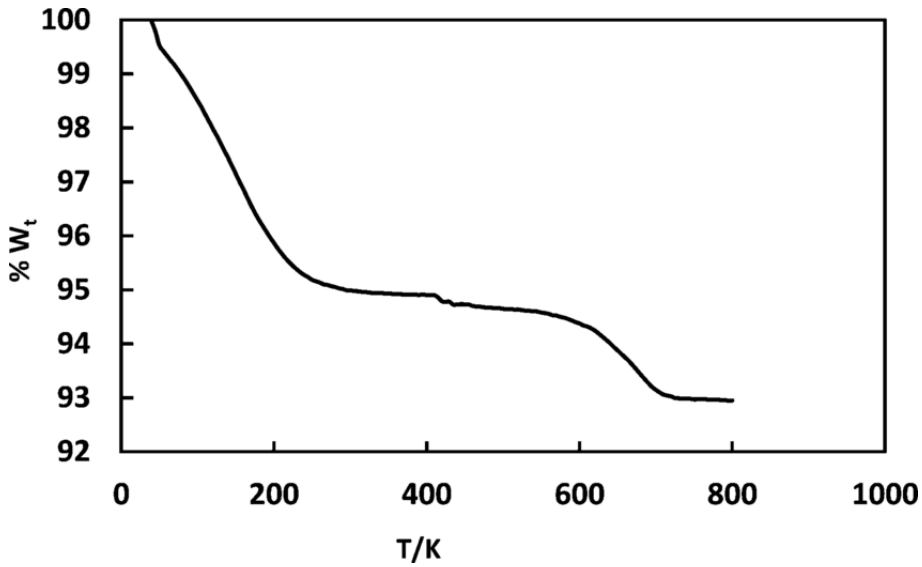

Figure 27: Typical graph of a TGA analysis. Represented from Ref.[36]

5.3. Gel permeation chromatography

Gel permeation chromatography (GPC) is a type of size exclusion chromatographic analysis. The principle of GPC is to circulate the polymer dissolved in an eluent (the mobile phase) through the static phase, which consists of a microporous gel. The shorter the polymer chain, the easier it will be to enter the pores of the static phase and at the same time increase its residence time in the column. The exit of the polymer chains is then detected at the end of the column using a refractometer or UV detector. Calibration of GPC column sets is performed using narrow molecular weight standards.[37]

5.4. Nuclear magnetic resonance

Proton nuclear magnetic resonance (NMR) spectroscopy is a technique used for determining the structure of molecules. The atomic nucleus of hydrogen with a nuclear spin is placed in a magnetic field. When subjected to electromagnetic radiation, the nucleus can absorb the energy of the radiation and then release it during relaxation. Free induction decay (FID) by Fourier transformation gives the NMR spectrum with peaks that can be integrated for hydrogen numbers. There are NMRs for other types of nuclei, such as carbon 13 NMR.[38]

5.5. Electrochemical impedance spectroscopy

Electrochemical impedance spectroscopy (EIS) measures the impedance of the system under study. Impedance is the resistance of a system through which an alternating current flows. The principle of measurement is to apply a small variation in potential to the sample over a

defined frequency range. The response in current variation is recorded. The impedance is known by applying the following formula: $U = Z \times I$ (8)

As the measured impedance is dependent on the intrinsic conductivity of the electrolyte and the dimensions between the measuring electrodes, the conductivity is deduced via this formula: $Z = \frac{1}{\sigma} \times \frac{l}{A}$ (9)

where l is the film thickness and A is the electrode contact area.

The impedance response is interpreted by a Nyquist diagram, as can be seen in figure **28**. It consists of a representation of the imaginary impedance as a function of the real impedance. On the graph, the overall impedance of the system can be read as the red dot. With this value given in Ohm (Ω), the conductivity of the electrolyte is deduced.[39, 40, 41.]

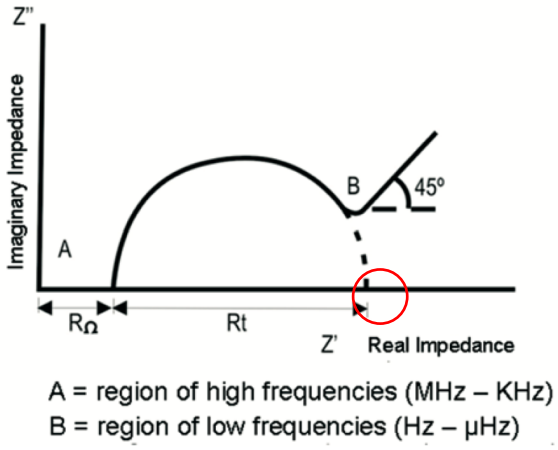

Figure 28: Nyquist diagram. Represented from Ref.[42]

5.6. Polarised optical microscopy

The polarised optical microscopy (POM) consists of a microscope with two orthogonal polarised filters separated by the presence of a sample. The first filter will select an initially unpolarised light orientation, if the sample is capable of birefringence, the plane of polarised light will rotate and there will be light transmission after the second cross polarising filter. It can be coupled with a heating plate to follow the transitions of the sample at different temperatures.[43] The figure **29** represents this principle.

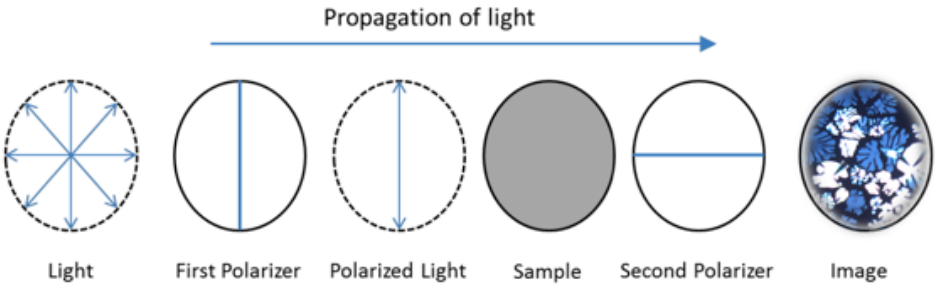

Figure 29: Schematic representation of principle for POM. Represented from Ref. [39]

5.7. Linear sweep voltammetry

Linear sweep voltammetry (LSV) is an analysis technique that provides information about redox potential. The analysis consists of varying the potential of the working electrode (measured against a reference electrode) linearly with time and recording the changes in electric current between the working electrode and the counter electrode. The analysed electrical current results from the oxidation or reduction of the polymer components of interest. The obtained data are entered into a graph of the electric current as a function of the applied voltage. To obtain a graph that combines the degradation of a polymer at high and low voltage, it is necessary to perform two measurements on two different cells.[44]

5.8. Cycling stability testing

This analysis allows the loss of cell capacity to be seen at each cycle. During charge/discharge cycles, the applied current is constant. However, the potential increases or decreases depending on the state of charge. When the cell is charged, the potential increases until it reaches the redox potential of the active material in the electrode. After that, the potential no longer varies and follows a plateau so that all the active material reacts. Then the charges continue to build up at the electrode until the cut-off potential is reached. The principle is the same for the discharge cell but the current flows in the opposite direction and the potential decreases until the cut-off potential is reached.[45]

III. Materials and methods

1. Reagents and Chemicals

All solvents were supplied by VWR. Reagents were purchased from Aldrich-Sigma except for 4-cyano-4'-hydroxyphenyl and *p*-methoxybenzylidene *p*-butylaniline which were supplied by Fluorochem. The reagents were used directly without any further purification.

2. Methods

2.1. Differential scanning calorimetry

The DSC measurements of LCs and SPEs were performed on a Mettler-Toledo 822e calorimeter. Samples were analysed under a nitrogen atmosphere in a 40 µL aluminum pan. The samples were cooled from 25 °C to -80 °C at a rate of 5 °C min^{-1}. The temperature was held for 1 minute before switching cycles. The samples were then heated from -80 to 120 °C. The temperature was held for 1 minute and then cooled to -80 °C at a rate of 5° C min^{-1}. The cooling-heating cycle was repeated three times. The software used to analyse the data was Stare.

2.2. Thermogravimetric analysis

The thermal stability of the LCs, polymers and SPEs was studied by thermogravimetric analysis. Those were carried out with a TGA/SDTA 851e (Mettler-Toledo, Switzerland). Samples of known mass were heated from 30 °C to 600 °C at a rate of 10 °C min^{-1}.

2.3. Gel permeation chromatography

The number average molar mass and weight average molar mass of the polymers and their dispersity were obtained using an Agilent size exclusion chromatography device equipped with an Agilent 1200 pump, an Agilent differential refractometer and two Polymer Standards Service Gram columns (1000 and 100 Å). The eluent used for the analyses was N,N-dimethylformamide containing 2.5×10^{-3} M of NH_4PF_6 and with a flow rate of 1 mL min^{-1}. The calibration is carried out using a poly(methylmethacrylate) (PMMA) standards.

2.4. Nuclear magnetic resonance

The ^{1}H-NMR spectra were acquired on a 300 MHz Bruker Avance II spectrometer. Samples were prepared by dissolution of 5 - 10 mg of the product with 600 µL of $CDCl_3$, DMSO-d6 or DMF-d7 as solvent.

2.5. Electrochemical impedance spectroscopy

EIS measurements were carried out using a Parstat 4000 instrument in the frequency range of 1 MHz to 10 mHz and with an alternating excitation potential amplitude of 10 mV. The measurements were taken from 30 to 100 °C in 10 °C increments. The coin cells were left in the oven for 30 minutes before taking the measurement.

2.6. Polarized optical microscopy

The samples were observed by POM. The device was an Olympus Provis AX70 series coupled to the Mettler FP 90 hot plate. The images were analysed via the automatic analySIS program.

2.7. Linear sweep voltammetry

To perform the SPE LSV measurements, the cells were run through a Parstat 4000 cycler down to 0 V for the low voltage test and down to 7 V for the high voltage test at a rate of 1 mV s^{-1} at 40 °C with a rest time of 30 minutes before analysis.

2.8. Discharge and charge experiments

For the discharge process a limit of 0 V (for the charge process 5 V) was set in order to avoid undesirable reactions and prevent the cell from quick ageing. The samples were measured immediately after assembly. They rested for one hour at RT to achieve an equilibrium before the discharge and charge experiments. The charge/discharge rates (r_c) were selected considering the capacity of the battery. Table **1** shows an example of the parameters for the different r_c for Cell-1 with a capacity of 2.14 x 10^{-4} Ah. The voltage range used is 3 - 3.8 V. The current is determined with the formula:

$$Current = charge/discharge\ rate \times capacity \quad (11)$$

The other samples were tested in a similar way.

Cycles	**Charge/Discharge rate** (h^{-1})	**Current** (A)	**Time** (min)
10	1	2.14 x 10^{-4}	60
10	2	4.28 x 10^{-4}	30
10	5	1.07 x 10^{-3}	12
10	1	2.14 x 10^{-4}	60

Table 1: Parameters for the different r_c for Cell-1.

3. Synthesis

3.1. Monomers

3.1.1. (2-oxo-1,3-dioxolan-4-yl) methyl methacrylate

Dry dimethylformamide (DMF) solution (100 mL) of 1,2-glycerol carbonate (35.24 g, 2.6 x 10^{-1} mol) and triethylamine (44.92 mL, 3.2 x 10^{-1} mol) are refluxed for one hour at RT under argon atmosphere. The solution is chilled in an ice-water bath and methacrylate chloride (26.23 mL, 2.6 x 10^{-1} mol) is added dropwise to the solution. The reaction is followed by thin layer chromatography (TLC). When the reaction is finished, the formed precipitate is collected on a Buchner. The solution is washed with water and brine. The aqueous phase and organic are separated via separating funnel. The organic phase is recovered and dried via Na_2SO_4. The solution is filtered and concentrated under air flow. The product is purified by chromatography column with ethyl acetate as eluent. The solvent is evaporated by air. The product is a pure viscous brownish liquid and is stored in dry DMF at a ratio of 80:20 by weight to avoid a self-polymerization. Yield is 12.2 g (68 %)[46]. The reaction scheme of (2-oxo-1,3-dioxolan-4-yl)methyl methacrylate (M1) is represented in figure **30**.

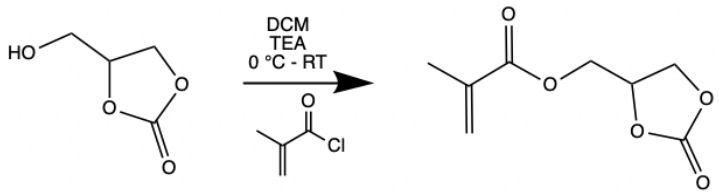

Figure 30: Reaction scheme of (2-oxo-1,3-dioxolan-4-yl)methyl methacrylate.

3.1.2. 2-((1,3,2-dioxaborepan-2-yl)oxy)ethyl methacrylate

Anhydrous acetonitrile solution (65 mL) of 1,4-butanediol (0.89 mL, 1 x 10^{-1} mol) and trimethyl borate (11.15 mL, 1 x 10^{-1} mol) is refluxed for one hour at RT under argon atmosphere. The poly(ethylene glycol) (36 g, 1 x 10^{-1} mol) is added to the solution. The solution is stirred at 65 °C for three hours and then stirred at RT overnight. The reaction is followed by TLC. The solution is concentrated by rotavapor. The product is a pure viscous colorless liquid. Yield is 14.3 g (80 %)[47]. The reaction scheme of 2-((1,3,2-dioxaborepan-2-yl)oxy)ethyl methacrylate (M2) is shown in figure **31**.

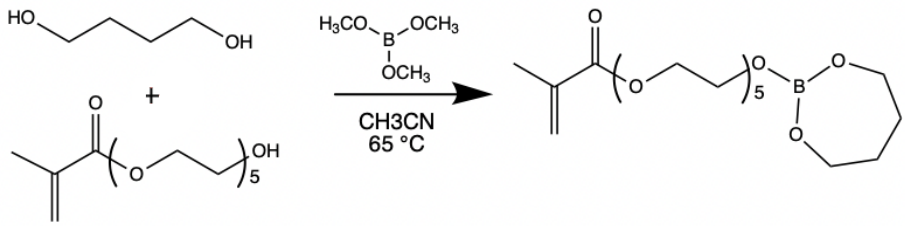

Figure 31: Reaction scheme of 2-((1,3,2-dioxaborepan-2-yl)oxy)ethyl methacrylate.

3.2. Polymers

The polymerisations were carried out with AIBN as initiator and in the presence of the chain transfer agent, 4-cyano-4-(phenyl-carbonothioyl(thio)pentanic acid (CTA) for the RAFT controlled radical polymerisation under argon atmosphere. The procedure is the same as for the FR polymerisation process, but without CTA. The proportions of AIBN and RAFT agent depend on the type of polymerisation performed. All polymerisations were carried out in anhydrous DMF and under an argon atmosphere. The solutions were degassed with argon for 30 minutes to remove all traces of oxygen and then heated at 70 °C. After completing the polymerization, the obtained polymers were recovered by precipitation in a cold diethyl ether solution followed by filtration. The polymers were then placed at 40 °C in a vacuum oven for 24 hours.

3.2.1. Copolymer of M1/M2

3.2.1.1. Radical reversible addition fragmentation chain transfer method

An anhydrous DMF (30 mL) solution of CTA (0.12 g, 4 x 10^{-4} mol), 80 mol % of M1 (6.70 g, 1 x 10^{-2} mol), 20 mol % of M2 (3.90 g, 9 x 10^{-3} mol) and AIBN (0.02 g, 1.3 x 10^{-4} mol) is degassed for 30 minutes. The solution is stirred at 70 °C for eight hours. The polymerisation is stopped when the temperature is decreased. The polymer is precipitated by adding it dropwise to a solution of cold diethyl ether (250 mL). The final product is a pink solid. Figure **32** shows the reaction scheme of copolymer M1/M2 synthesized by RAFT method.

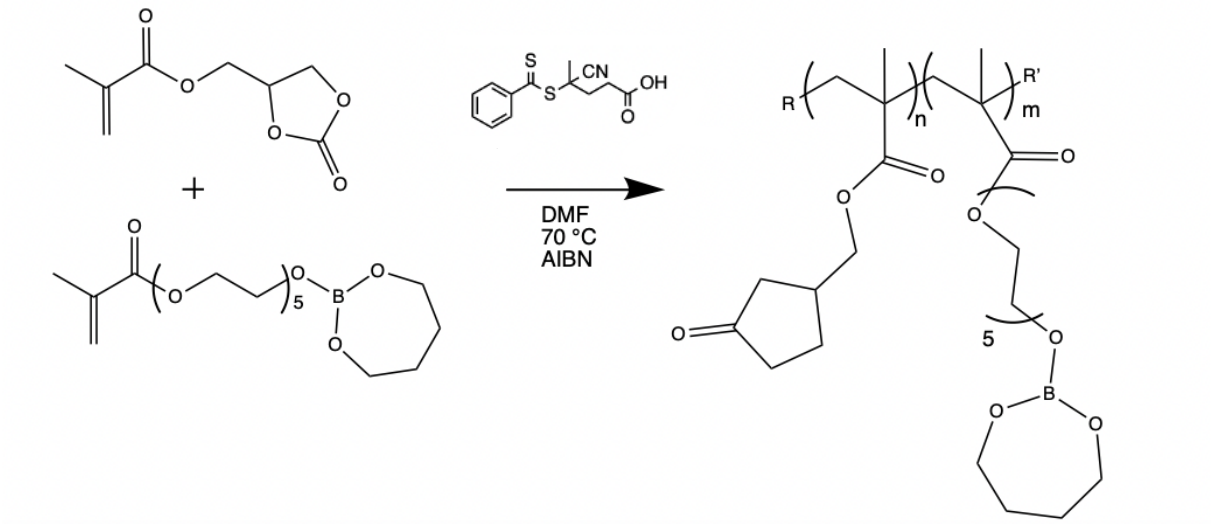

Figure 32: Reaction scheme of copolymer M1/M2 by RAFT method.

3.2.1.2. Free radical method

An anhydrous DMF (24 mL) solution with 80 mol % of M1 (2.79g, 3.6 x 10^{-2} mol), 20 mol % of M2 (1.30 g, 3 x 10^{-3} mol), AIBN (1.2 x 10^{-2} g, 7 x 10^{-5} mol) is degassed for 30 minutes. The solution is stirred at 70 °C for five hours. The polymerisation is stopped when the temperature is decreased. The polymer is precipitated by adding it dropwise to a solution of cold diethyl ether (250 mL). The final product is a colourless solid. Figure **33** shows the reaction scheme of copolymer M1/M2 synthesised by FR method.

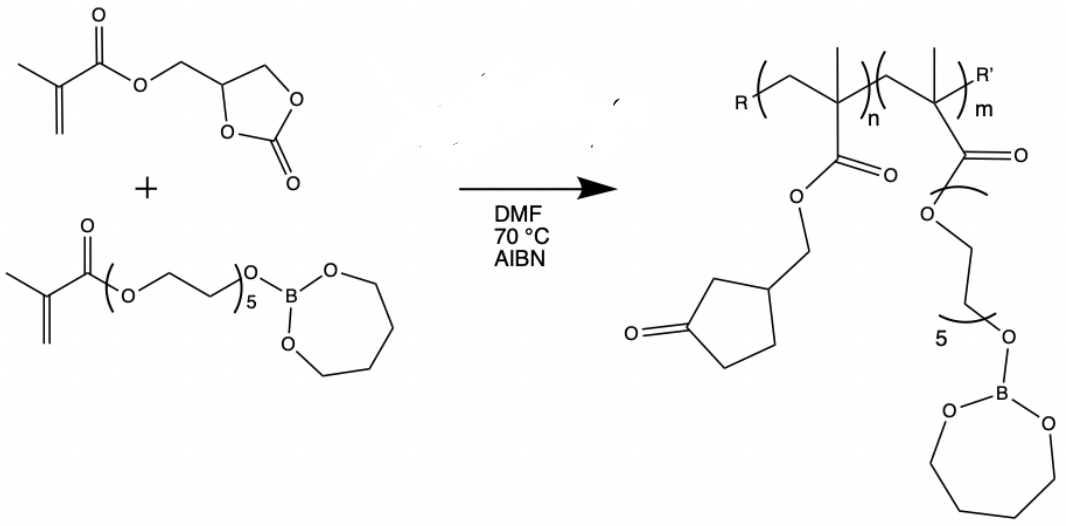

Figure 33: Reaction scheme of copolymer M1/M2 by FR polymerization.

3.2.2. Homopolymer of poly(ethylene glycol) methyl ether methacrylate

An anhydrous DMF (10 mL) solution of poly(ethylene glycol) methyl ether methacrylate (10 g, 3.3 x 10^{-2} mol), AIBN (8.2 x 10^{-3} g, 5 x 10^{-5} mol), trioxane (1 g, 1.1 x 10^{-2} mol) and RAFT agent

(9.3 x 10^{-2} g, 3 x 10^{-4} mol) is degassed during 30minutes. The solution is stirred at 70 °C for 17 hours. The polymerisation is stopped when the temperature is decreased. The polymer is precipitated by adding it dropwise to a solution of cold diethyl ether (250 mL). The final product is a pink viscous solid. Figure **34** shows the reaction scheme for poly(ethylene glycol) methyl ether methacrylate (M3) homopolymer synthesis by RAFT method.

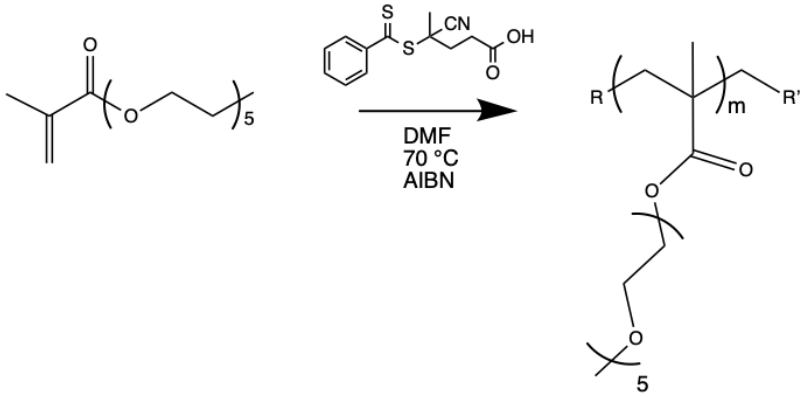

Figure 34: The reaction scheme of M3 homopolymer.

3.3. Liquid crystals

3.3.1. 4'-((6-hydroxyhexyl)oxy)- [1,1'-biphenyl]-4-carbonitrile

A dry acetone solution (150 mL) of 4-cyano-4'-hydroxyphenyl (21.66 g, 1.1 x 10^{-1} mol), anhydrous potassium carbonate (30.67 g, 2.2 x 10^{-1} mol) and a spatula of potassium iodide is refluxed at 65 °C under argon atmosphere. 1-bromo-6-hexanol (20.09 mL, 1.4 x 10^{-1} mol) is added dropwise to the solution and is maintained at 65 °C overnight. The reaction is followed by TLC. When the reaction is complete, the solution is poured into a beaker containing 350 mL of demineralised water. The precipitate is recovered by Buchner filtration and pump drying. The crude product is recrystallized from methanol (45 mL). The final product is a white crystalline material and it is stored at RT. Yield is 29.4 g (98%)[48]. Figure **35** shows the reaction scheme of 4'-((6-hydroxyhexyl)oxy)-[1,1'-biphenyl]-4-carbonitrile (MALC).

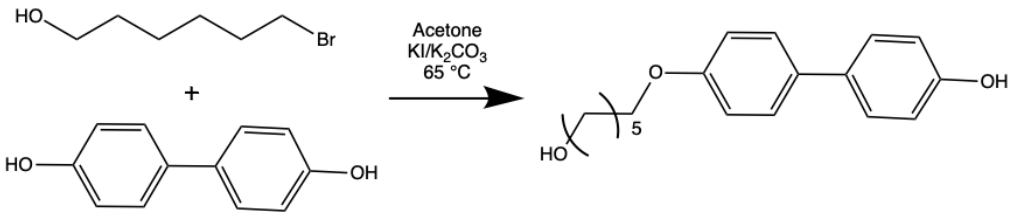

Figure 35: Reaction scheme of 4'-((6-hydroxyhexyl)oxy)-[1,1'-biphenyl]-4-carbonitrile.

3.3.2. *4'-(hexyloxy)-[1,1'-biphenyl]-4-carbonitrile*

A dry acetone solution (50 mL) of 4-cyano-4'-hydroxyphenyl (3.70 g, 1.9 x 10^{-2} mol), anhydrous potassium carbonate (7.87 g, 5.7 x 10^{-2} mol) and a spatula of potassium iodide was refluxed at 65 °C under argon atmosphere. Bromohexane (4 mL, 2.8 x 10^{-2} mol) is added dropwise to the solution and is maintained at 65 °C overnight. The reaction is followed by TLC. When the reaction is finished, the solution is recovered and concentrated by rotavapor. After the rotavapor, the flask is put to the vacuum pump. The crude product is recrystallized from methanol:hexane (15:15). The pure product is a white crystal and is stored at RT. Yield is 2,1 g (42%)[48]. The reaction scheme of 4'-(hexyloxy)-[1,1'-biphenyl]-4-carbonitrile (HBC) is shown in figure **36**.

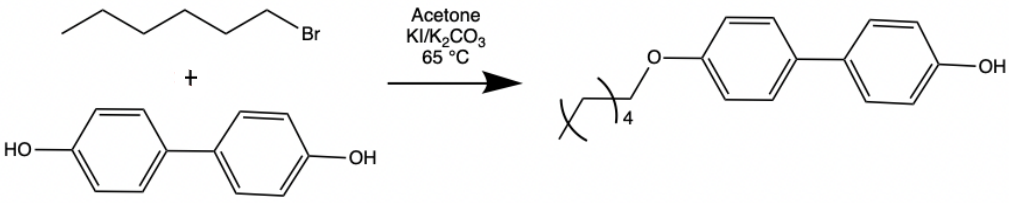

Figure 36: Reaction scheme of 4'-(hexyloxy)-[1,1'-biphenyl]-4-carbonitrile.

3.4. Preparation of solid polymer electrolytes

The electrolyte films were prepared by dissolving the polymer (1 molar ratio), liquid crystal (0.5-1-2 molar ratio), and lithium salt (LiTFSI in a molar ratio of 2) in acetonitrile or DMF (1 mL). The addition of LiTFSI is performed in the glove box under controlled argon atmosphere. The solutions are deposited on 0.5 mm thick stainless-steel disks either directly or using a glass fiber. The solvent was removed by placing the stainless-steel disk in the oven at 40 °C under vacuum for 48 hours. Table **2** gives an example of composition for MBBA with M1/M2 RAFT. In this table, M1/M2 RAFT is used as polymer matrix, MBBA as liquid crystal and LiTFSI as lithium salt. The percentage weight is used as a reference, it has not been considered in the calculations. The proportions are the same for other LCs and M3 RAFT polymer.

Abbreviation	**Polymer matrix**			**Liquid crystal**			**Lithium salt**	
	Name	**Molar ratio**	**Weight** (%)	**Name**	**Molar ratio**	**Weight** (%)	**Molar ratio**	**Weight** (%)
SPE-MBBA-0.5	M1/M2 RAFT	1	25	MBBA	0.5	14	2	61
SPE-MBBA-1	M1/M2 RAFT	1	22	MBBA	1	25	2	53
SPE-MBBA-2	M1/M2 RAFT	1	18	MBBA	2	40	2	42

Table 2: Composition of SPEs made with M1/M2 RAFT and MBBA.

3.5. Preparation of catholyte

The catholytes are prepared by first dissolving the M1/M2 polymer (0.219 g, 9.28 x 10^{-4} mol) in anhydrous DMF (2 mL) at RT. Then Super P (0.1 g, 8.33 x 10^{-3} mol) and lithium iron phosphate (LFP) (0.9 g, 5.71 x 10^{-3} mol) are mixed via mortar and added to the solution along with LiTFSI (0.533 g, 1.9 x 10^{-3} mol) and *p*-methoxybenzylidene *p*-butylaniline (MBBA) (0.248 g, 9.28 x 10^{-4} mol) as liquid crystal. In total 2 g of final product are produced. These data are collected in table **3**.

	Components	**Weight** (%)	**Quantity** (g)	**Number of moles** (mol)
Active material	LFP	45	0.9	5.71 x 10^{-3}
Carbon	Super P	5	0.1	8.33 x 10^{-3}
SPE	M1/M2 RAFT	22	0.219	9.28 x 10^{-4}
	MBBA	25	0.248	9.28 x 10^{-4}
	LiTFSI	53	0.533	1.90 x 10^{-4}

Table 3: Composition of catholytes.

Beads are added to the solution to ensure proper homogenization before being stirred at room temperature for 24 hours. The drop casting is carried out on an aluminum foil coated with carbon with a thickness of 100 µm. The catholyte is dried at 50 °C in an oven. The catholyte is cut into a disk of 8 mm diameter. Figure **37** shows a picture of catholyte coated on the aluminum foil.

Figure 37: Picture of a catholyte on aluminum foil.

After cutting, the catholytes are weighed to determine the exact amount of LFP (45% of the catholyte weight), so that the capacity of the catholytes can be determined. Indeed, the theoretical specific capacity of LFP is known to be equal to 170 mAh g^{-1}.

3.6. Coin cell assembly

3.6.1. Impedance electrochemical spectroscopy experiments

The electrolyte-soaked glass fibers are placed on the 0.5 mm thick stainless-steel disk. They are topped by a second stainless steel disk of the same diameter. These two stainless-steel disks were then assembled in a coin cell type 2032 cell with a spring to ensure optimal contact. The cells were sealed under five tons pressure. The thickness of the films is also measured before and after the EIS. For an EIS comparison test, a cell is constructed using a teflon spacer instead of glass fiber. Figure **38** shows a schematic representation of the different components of the coin cell.

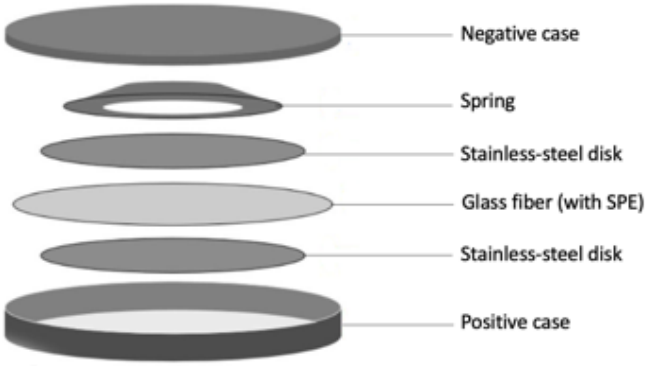

Figure 38: Schematic representation of components for coin cell 2032.

3.6.2. Linear sweep voltammetry experiments

The cell assembly is the same as for EIS measurements just with the difference that the electrolyte-soaked glass fiber is put between a stainless-steel disk and a lithium disk and a spring.

3.6.3. Charge-discharge experiments

For the cycling stability tests, the coin cell is assembled using the prepared catholyte. The catholyte is placed on a stainless-steel disk. On top of this catholyte is added a glass fiber soaked with $LiPF_6$ solution in EC/DMC (135 µL) or with the SPE. The glass fiber is topped with a 15 mm diameter lithium electrode. The coin cell type 2032 cell is then sealed under five tons pressure.

IV. Results and discussions

The work for this master thesis is divided into three major parts.

1. Synthesis of the monomers, LCs, and polymerizations
2. Electrochemical and thermal characterizations of solid polymer electrolytes
3. Electrochemical characterization of catholytes

1. Synthesis of the monomers, liquid crystals, and polymerizations

1.1. Monomers

The synthesis of the monomers (2-oxo-1,3-dioxolan-4-yl) methyl methacrylate (M1) and 2-((1,3,2-dioxaborepan-2-yl) oxy) ethyl methacrylate (M2) was realized while poly(ethylene glycol) methyl ether methacrylate (M3) was purchased. The structures of these three monomers are shown in table **4.**

Abbreviation	Name	Structure
M1	(2-oxo-1,3-dioxolan-4-yl)methyl methacrylate	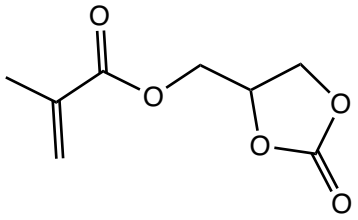
M2	2-((1,3,2-dioxaborepan-2-yl)oxy)ethyl methacrylate	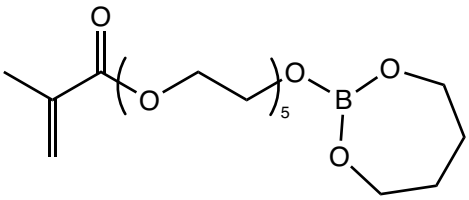
M3	Poly(ethylene glycol) methyl ether methacrylate	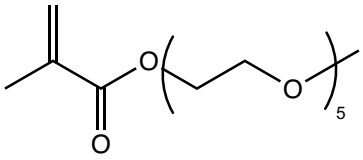

Table 4: Structure of monomers used for this project.

These three different monomers were selected to create the polymer matrix: the cyclocarbonate and polyethylene glycol have been widely studied as electrolytes and their ion-conductive properties are well established.[1] This provides reference systems in order to demonstrate the advantages and/or disadvantages related to the further addition LCs. M2 (variation of M3) was introduced to increase the mechanical properties of the SPE since after the addition of LC the SPE presented poor mechanical properties.[49] In addition, boron is a

Lewis acid, *i.e.* a molecule with an electron gap, which will allow the complexation of the lithium salt anion. This complexation means that the majority of the charge balance is achieved by Li^+ which is useful to mitigate the growth of lithium dendrites.

1.1.1. (2-oxo-1,3-dioxolan-4-yl) methyl methacrylate

The reaction mechanism for the synthesis of M1 is illustrated in figure **39**. The free electron pair of triethylamine (TEA) attacks the hydrogen of the alcohol group of 1,2-glycerol carbonate forming an alcoholate. The alcoholate will perform a nucleophilic attack on the carbonyl of the methacryloyl chloride and break the bond of the chloride anion leaving group.

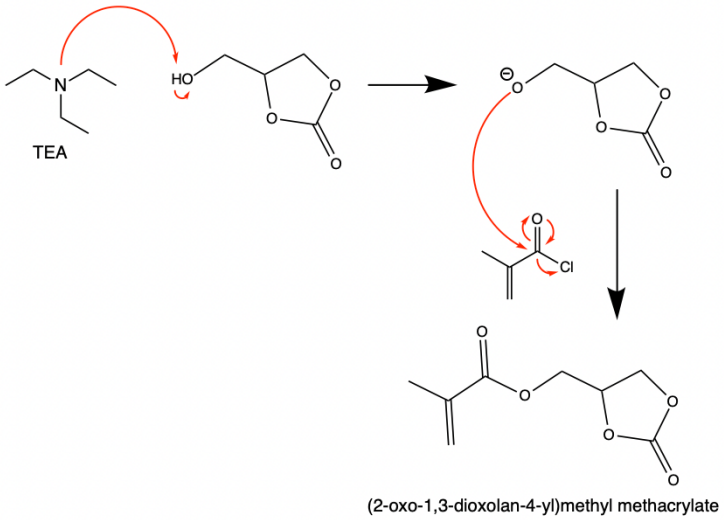

Figure 39: Mechanism for the formation of M1.

The ^{1}H-NMR analysis confirms the structure of M1 with high purity (96 % HPLC). The ^{1}H-NMR spectrum is shown in figure **40**.

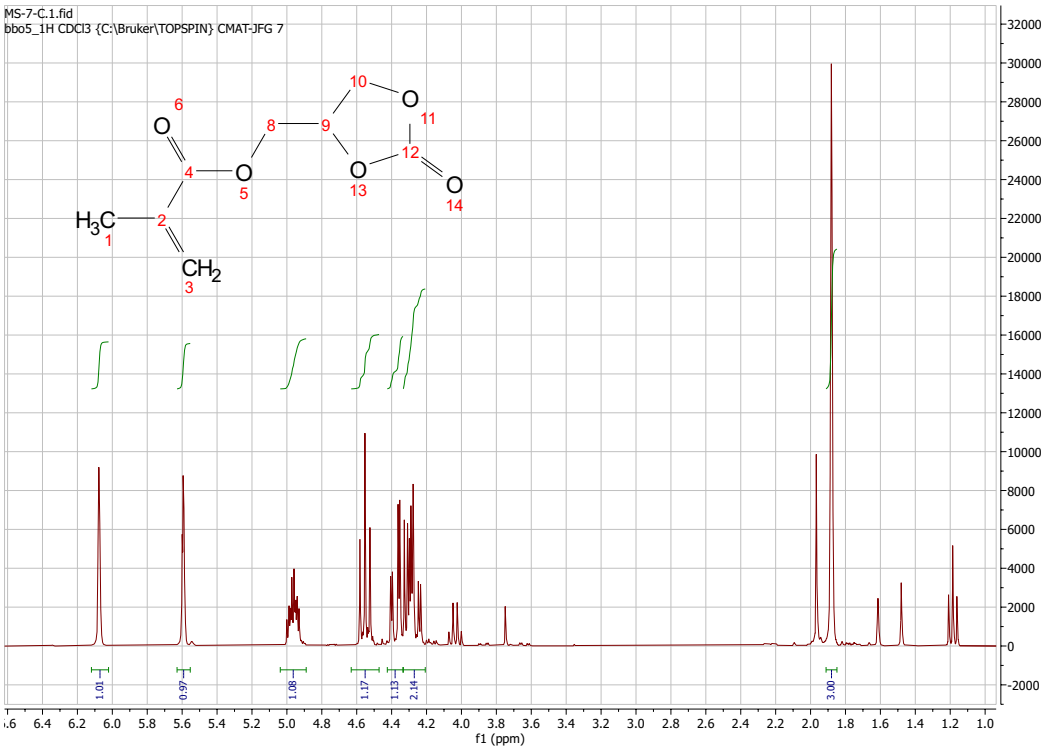

Figure 40: ^{1}H-RMN spectrum of M1.

^{1}H-NMR [300MHz, CD_3, δ(ppm)] of M1: 6 (s, 1H, H3), 5.6 (s, 1H, H3), 4.8-5 (m, 1H, H9), 4.5 (t, 1H, H8), 4.3 (m, 1H, H8), 4.2 (m, 2H, H10), 1.9-1.8 (s, 3H, H1).

1.1.2. 2-((1,3,2-dioxaborepan-2-yl)oxy)ethyl methacrylate

The reaction mechanism for the synthesis of M2 is illustrated in figure **41**. The alcohol function of 1,4-butanediol attacks the B of the trimethyl borate and methanol is released. The second alcohol function attacks the boron forming the cyclic boronate. The last step is the addition of poly(ethylene glycol) by attacking the alcohol function on the boron of the cyclic boronate.

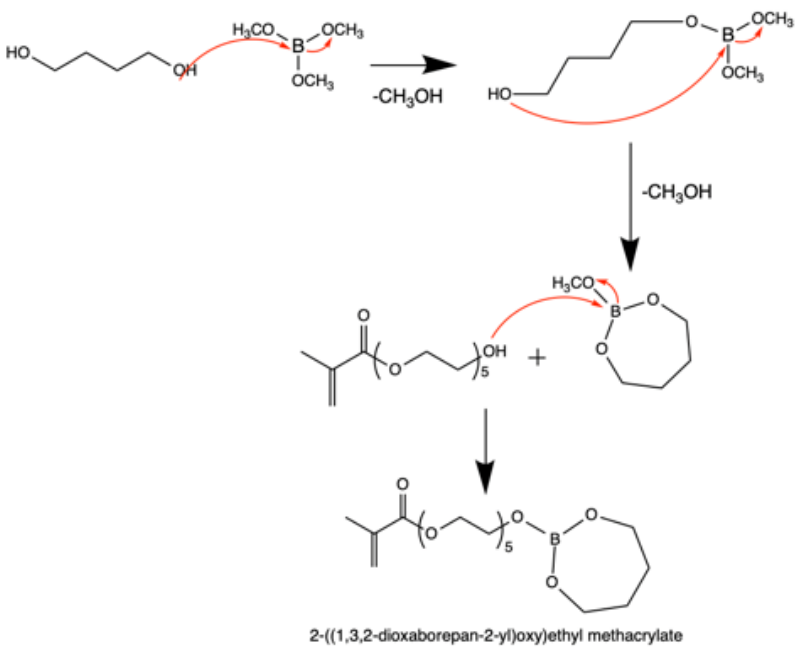

Figure 41: Mechanism for the formation of M2.

The ^{1}H-NMR analysis confirms the structure of M2 with high purity and the spectrum is shown in figure **42**.

Figure 42: ^{1}H-RMN spectrum of M2.

^{1}H-NMR [300MHz, CD_3, δ(ppm)] of M2: 6.2 (s, 1H, H4), 5.6 (s, 1H, H4), 4.4 - 4.2 (t, 2H, H8), 4 - 3.8 (m, 4H, H25-H28), 3.7 (t, 2H, H9), 3.6 (s, 16H, H11-H12-H14-H15-H17-H18-H20-H21), 2(s, 3H, H3), 1.9 - 1.5 (m, 4H, H26-H27).

1.1.3. Poly(ethylene glycol) methyl ether methacrylate

The M3 monomer has a Mn of 300 g mol^{-1} indicating an average of five ethylene oxide units. The ^{1}H-NMR analysis confirms the structure of M3 and the spectrum is shown in figure **43**.

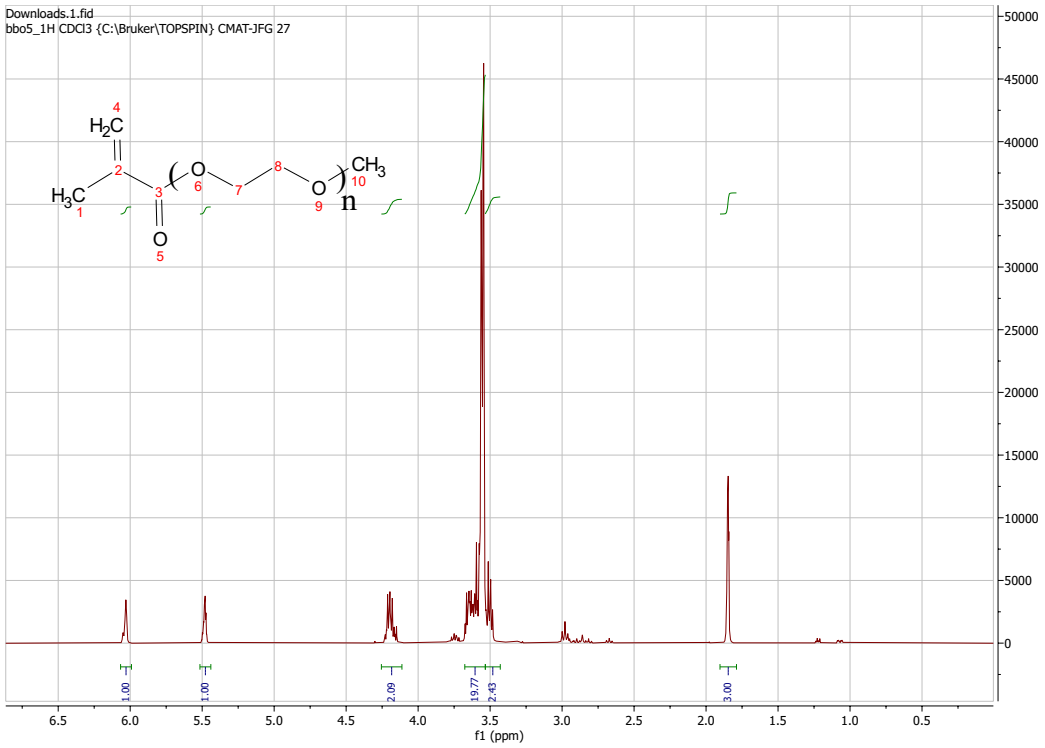

Figure 43: ^{1}H-RMN spectrum of M3.

^{1}H-NMR [300MHz, CD_3, δ(ppm)] of M3: 6.2 (s, 1H, H4), 5.4 (s, 1H, H4), 4.4 - 4.2 (t, 2H, H7), 3.5 (s, 3H, H0), 3.6 (m, 20H, H8) 1.8 (s, 3H, H1).

1.2. Polymers

Different M1/M2 ratios were tested and the 80/20 weight ratio was selected. This is the best compromise between conductivity, mechanical properties, and interactions with LCs (soaking capacity). Table **5** summarizes the compositions and characteristics of the synthesized polymers.

Abbreviation	Polymer type	Monomer ratio in weight percentage (%)			Polymerization method	Mn (g mol^{-1})	PDI
		M1	M2	M3			
M1/M2 RAFT	Copolymer	80	20	0	RAFT	37 400	1.5
M1/M2 FR	Copolymer	80	20	0	FR	32 410	3.2
M3 RAFT	Homopolymer	0	0	100	RAFT	39 000	1.5

Table 5: Composition and characterization of polymers

As it can be seen in table 5, the PDI of polymers made by FR is twice as high as those made by RAFT polymerisation. As far as the average molecular weight is concerned, the three polymers are in the same range. The M1/M2 copolymer is a hard solid and while the M3 homopolymer is a soft solid.

^{1}H-NMR analysis of the M1/M2 RAFT copolymer is used to estimate its real composition. To determine the real ratio between M1 and M2, the two characteristic peaks of the monomers are integrated, namely H9 of M1 and H26 and H27 of M2 (circled in red in figure **44**). The H9 peak is integrated for 1 hydrogen. The integration of the peak corresponding to M2 is 1.05. Knowing that the M2 peak is worth four hydrogens, the integration of one proton is worth 0.25, in other words 20 % of the final composition.

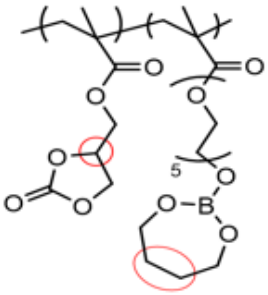

Figure 44: Structure of M1/M2 copolymer

The determination of ratio of M1/M2 FR polymer is realised by the same method as M1/M2 RAFT.

DSC measurements of the three polymers were performed with a sweep between -80 °C and 120 °C with a ramp of 5 °C min^{-1} under nitrogen flow. These analyses showed that there is no detectable glass transition in this range of temperature. The thermal stability of the three polymers is measured by thermogravimetric analysis. The thermograms of the polymers are shown on figure **45**.

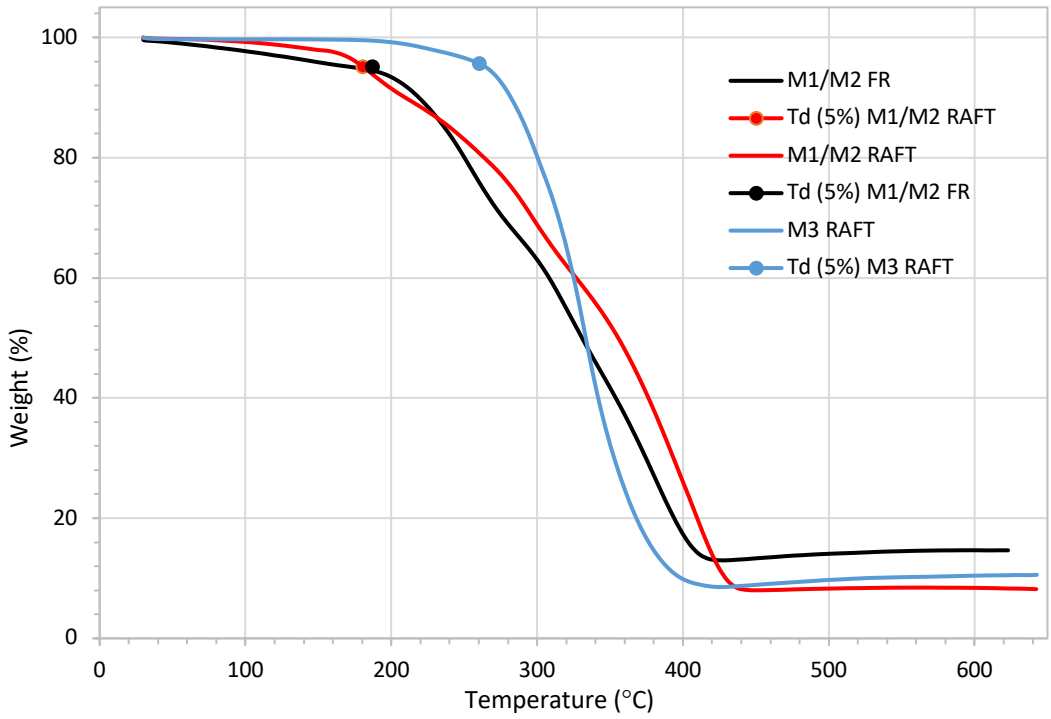

Figure 45: Thermograms of the polymers, weight (%) vs. temperature (°C).

The values of the degradation temperatures of the polymers are available in table 6. This temperature corresponds to a loss of 5 % by mass of the analysed compound. Above this temperature, the compound is considered unstable. The Tds (5 %) of the M1/M2 RAFT and FR polymers are quite similar. However, the Td (5 %) of M3 RAFT is higher. The M3 RAFT shows a higher stability but also a higher decomposition rate. A summary of the degradation temperatures of the polymers can be found in table **6**.

Polymer matrix	**Td (5 %)** (°C)
M1/M2 RAFT	180.2
M1/M2 FR	186.8
M3 RAFT	260.2

Table 6: Results of TGA for the three polymers.

1.3. Liquid crystals

Another step in this work is the synthesis of the liquid crystals, namely 4'-((6-hydroxyhexyl)oxy)-[1,1'-biphenyl]-4-carbonitrile and 4'-propoxy-[1,1'-biphenyl]-4-carbonitrile. *P*-methoxybenzylidene *p*-butylaniline was purchased.

The structures of these three liquid crystals and their abbreviations are shown in table **7**.

Abbreviation	Name	Structure
HBC	4'-propoxy-[1,1'-biphenyl]-4-carbonitrile	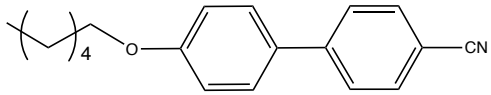
MBBA	*p*-methoxybenzylidene *p*-butylaniline	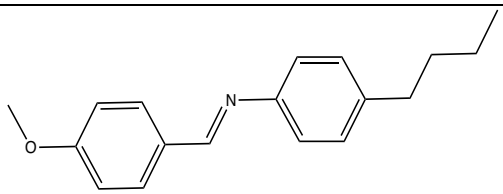
MALC	4'-((6-hydroxyhexyl) oxy)-[1,1'-biphenyl]-4-carbonitrile	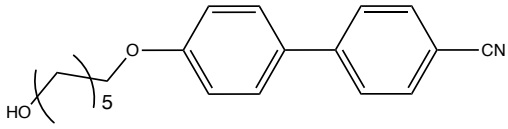

Table 7: Structure of LCs used for this project.

These three different LCs were selected because they show three different transition temperatures which allows a better understanding of the influence on the conductivity of the LCs.

1.3.1. 4'-(hexyloxy)-[1,1'-biphenyl]-4-carbonitrile

The reaction mechanism for the synthesis of HBC is illustrated in figure **46**. The base, potassium carbonate (K_2CO_3), deprotonates the terminal alcohol of 4-cyano-4'-hydroxyphenyl. The potassium iodide catalyses the reaction by replacing bromide. The alcoholate attacks the carbon bearing the iodide and rejects the iodide anion.

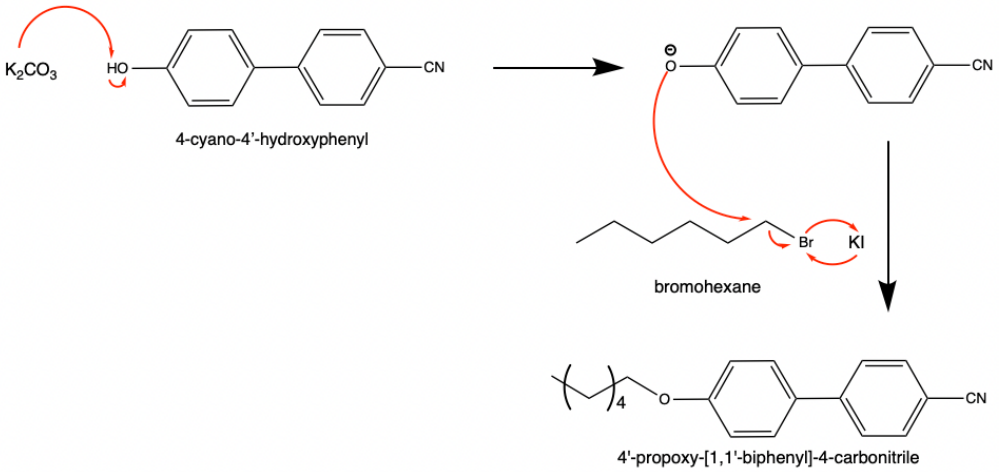

Figure 46: Mechanism for the synthesis of HBC.

The ^{1}H-NMR analysis confirms the structure of HBC with high purity and the spectrum is shown in figure **47**.

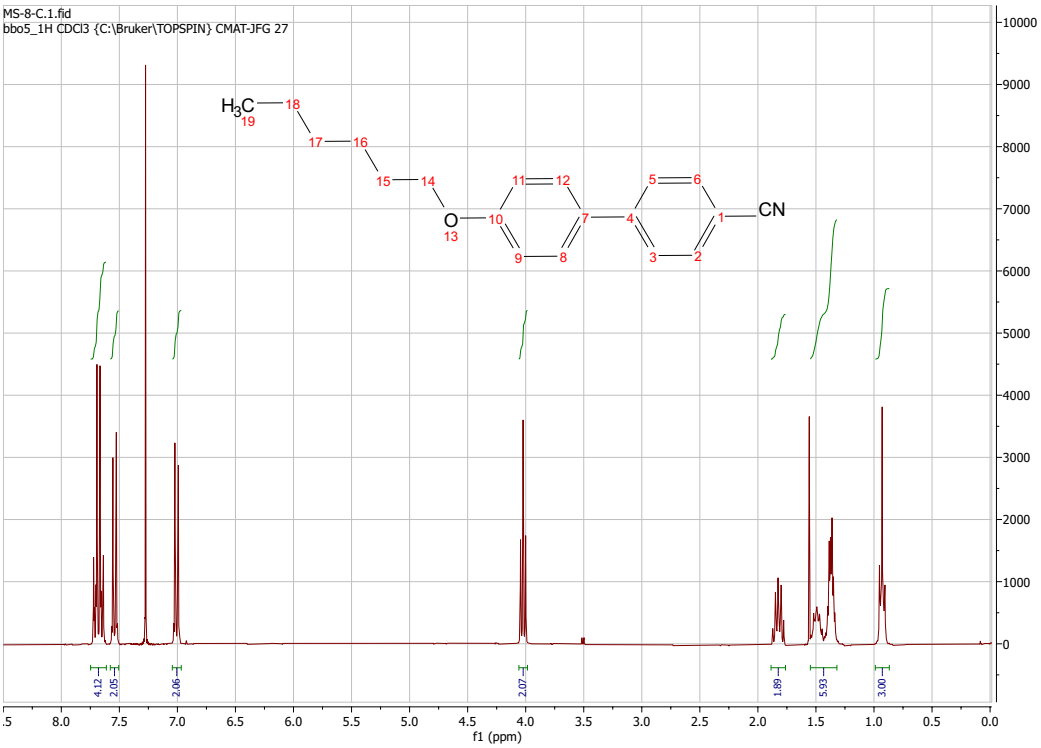

Figure 47: [1]H-NMR spectrum of HBC.

[1]H-NMR [300MHz, CD_3, δ(ppm)] of HBC: 7.6 - 7.7 (m, 4H, aromatic), 7.5 (d, 2H, aromatic), 7 (d, 2H, aromatic), 4 (t, 2H, H14), 1.6 - 1.7 (m, 2H, H15), 1.4 - 1.5 (m, 6H, H16-17-18), 0.9 (t, 3H, H19). [1]H-NMR analysis shows the presence of trace amounts of water and residual methanol.

The thermal stability of HBC is measured by thermogravimetric analysis. The thermogram of HBC is shown in figure **48**. The Td (5 %) of HBC is 349.3 °C. At 500 °C, only 7 % of the initial product remains. The signal noise visible on the degradation curve is not of chemical origin. They are due to the vibration of the balance because of the laboratory conditions during the measurement.

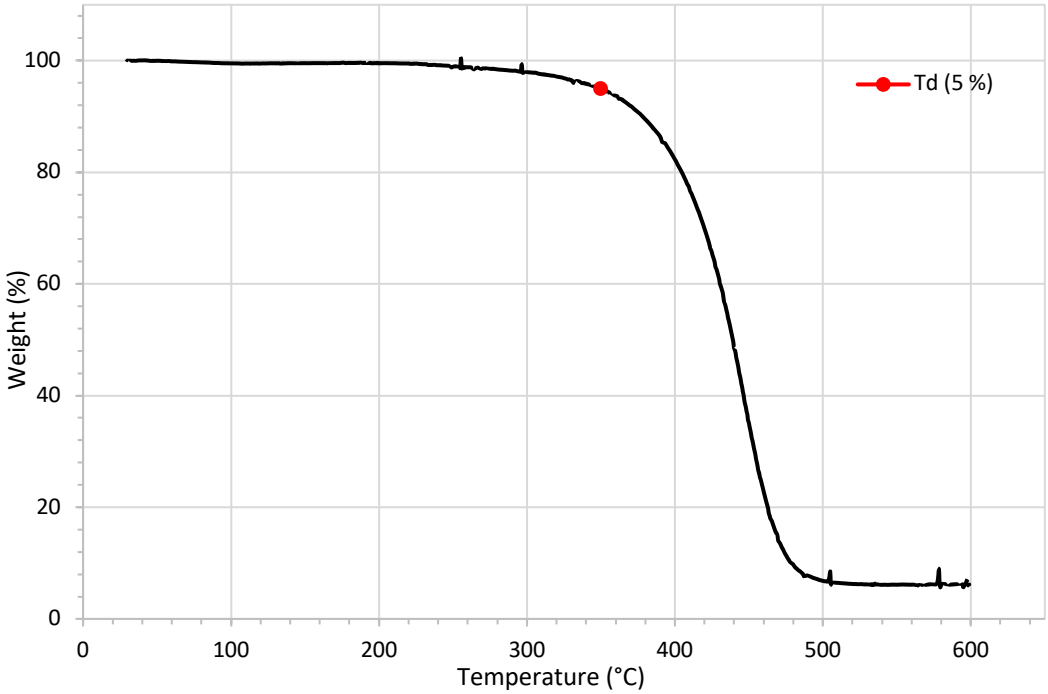

Figure 48: Thermogram of HBC, weight loss (%) vs. temperature (°C).

The DSC spectrum of HBC is shown in figure **49**. As can be seen from the graph, there are two peaks for heating and two for cooling. The first heating peak at 58 °C corresponds to the endothermic heat exchange. It is the peak of the transition between the crystalline to the liquid crystal phase (Tm). The second heating peak is smaller at 77°C and corresponds to the transition from the liquid crystal phase to the isotropic liquid phase (Tc). As it can be seen from the cooling curve, there are two peaks corresponding to the exothermic exchange. The first peak at 77°C is the transition between isotropic liquid to liquid crystal phase. The second peak at 26 °C corresponds to the transition between liquid crystal to crystalline phase of HBC. The shift between this temperature and Tm is called over cooling effect.

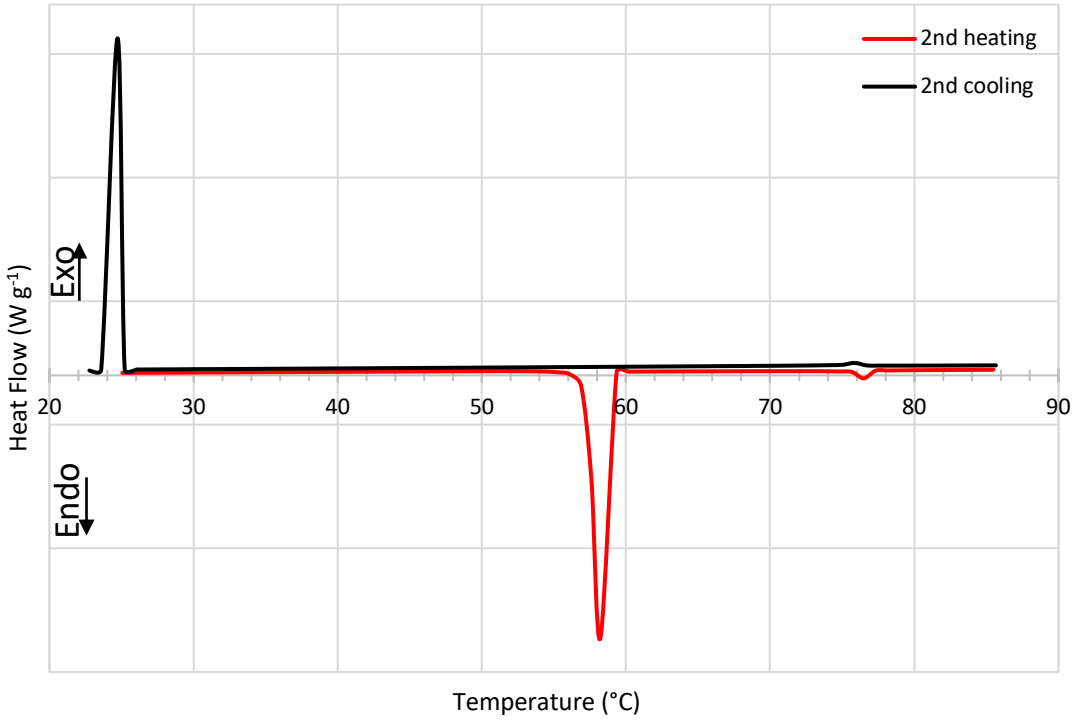

Figure 49: Thermogram of HBC, heat flow (W g^{-1}) vs. temperature (°C).

Figure **50** is a picture of HBC taken with POM at 65 °C (in the liquid crystal state) with a magnification of 100. This image confirms presence of the LC and shows the characteristic texture of a smectic mesophase.

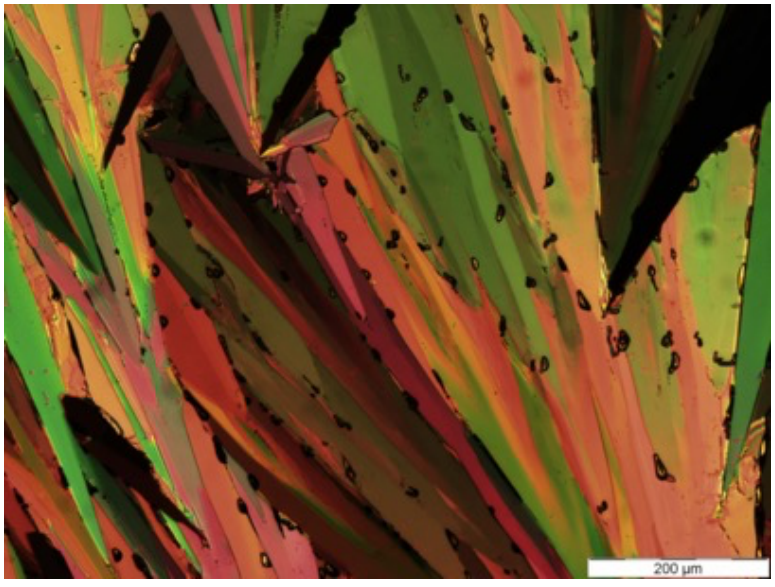

Figure 50: Picture of HBC taken by POM at 65°C.

1.3.2. P-Methoxybenzylidiene-p-butylaniline

The ^{1}H-NMR analysis confirms the structure of MBBA, and the spectrum is shown in figure **51**.

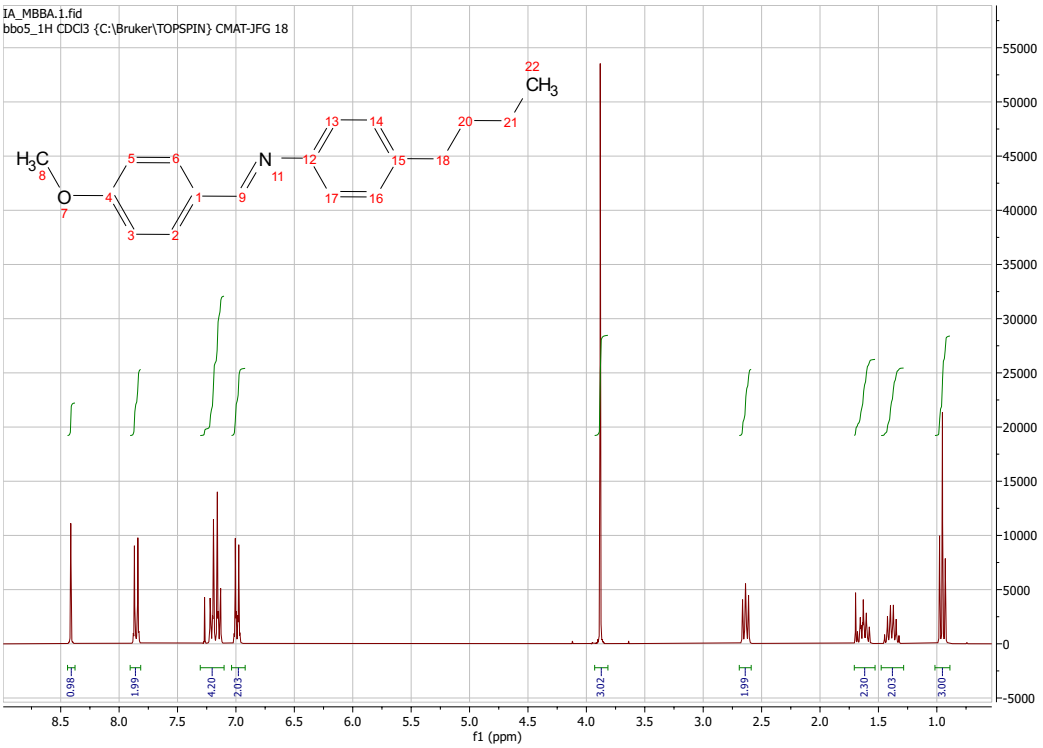

Figure 51: ^{1}H-NMR spectrum of MBBA.

^{1}H-NMR [300MHz, CD_3, δ(ppm)] of MBBA: 8.4 (s, 1H, H9), 7.9 (d, 2H, H2-H6), 7.3 - 7.2 (q, 4H, H13-H14-H16-H17), 7 (d, 2H, H3-H5), 3.9 (s, 3H, H8), 2.6 (t, 2H, H18), 1.6 (m, 2H, H20), 1.4 (m, 2H, H21), 0.9 (t, 3H, H22).

The thermal stability of MBBA is measured by thermogravimetric analysis. The thermogram of MBBA is shown in figure **52**. The Td (5 %) of MBBA is 346.4 °C. As it can be seen on figure **52**, there are 2 mechanisms of degradation. The first drop corresponds to a 38 % degradation. At 365 °C, there is another drop. In order to know which degradation is taking place, it would be necessary to analyse the gases produced with a coupled high-resolution mass spectroscopy (HRMS). At 500 °C, only 13 % of product remains.

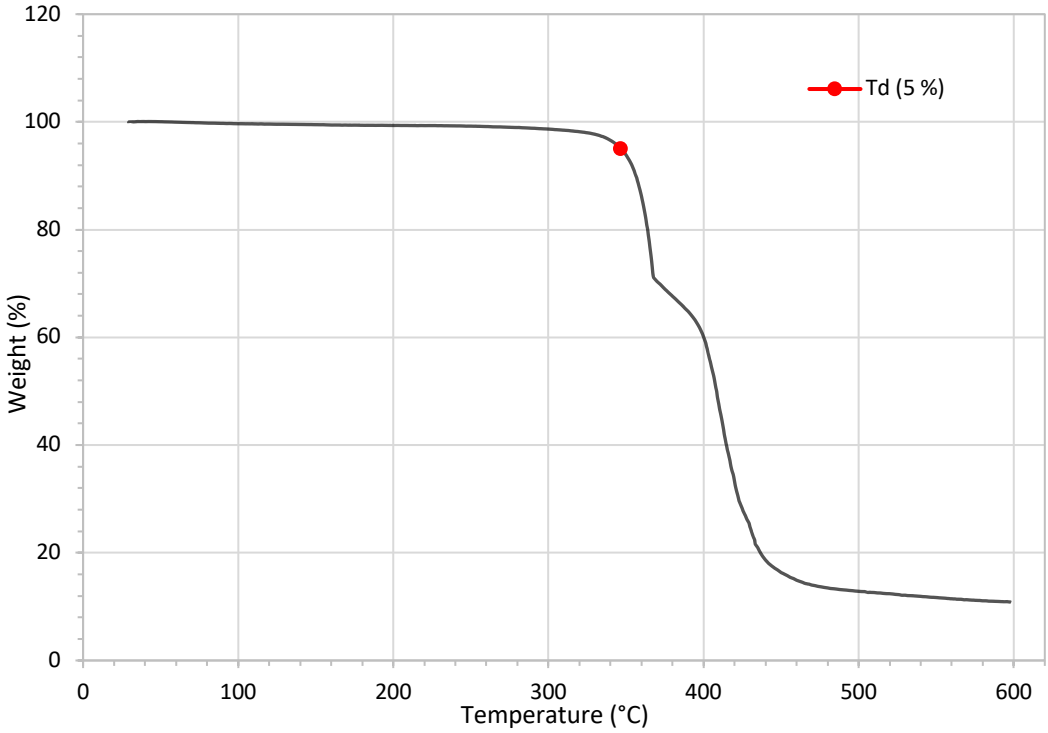

Figure 52: Thermogram of MBBA, weight loss (%) vs. temperature (°C).

The DSC thermogram of MBBA is shown in figure **53**. As it can be seen from the graph, there are two peaks for heating and two for cooling. The second heating peak at 41 °C is not very visible in this case but is clearly present during cooling. The first heating peak at 17 °C (Tm) corresponds to the transition between the crystalline to liquid crystal phase. The first heating peak corresponds to a larger endothermic exchange than the second one. The second heating peak is at 41 °C (Tc) and corresponds to the transition between the liquid crystal to the isotropic liquid phase of MBBA. The first cooling peak at 44 °C corresponds to the transition between the isotropic liquid to the liquid crystal phase. The second cooling peak at 4 °C is the transition between the liquid crystal to crystalline phase of MBBA. There is also a shift due to the over cooling effect.

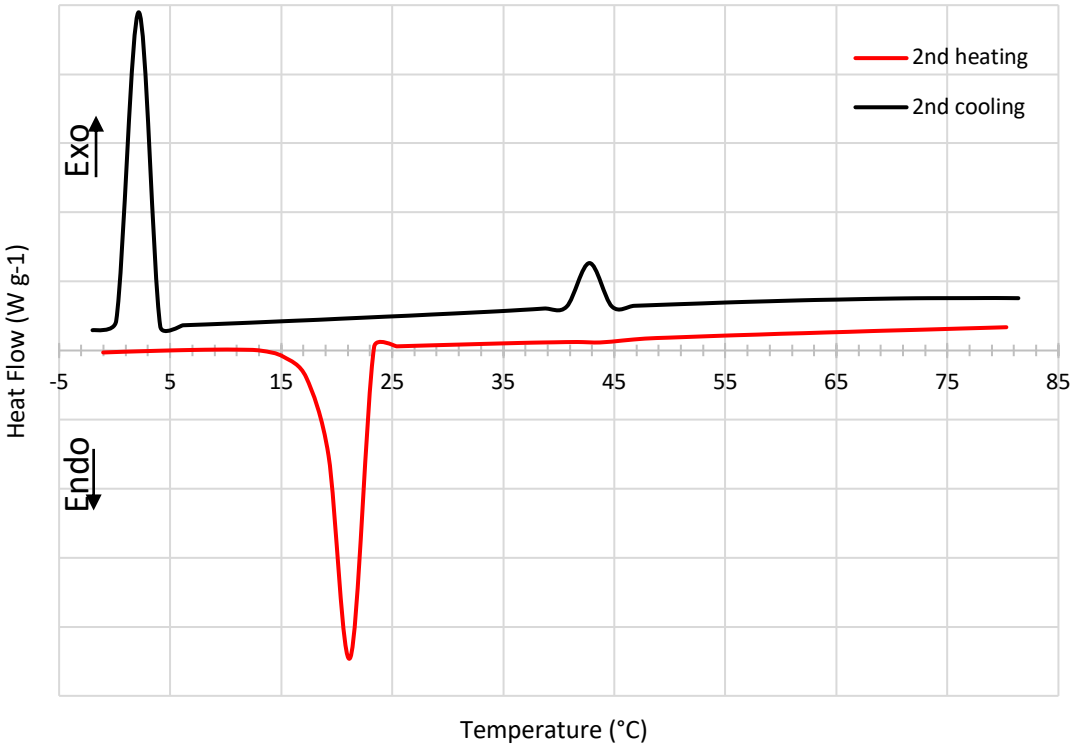

Figure 53: Thermogram of MBBA, heat flow (W g^{-1}) vs. temperature (°C).

Figure **54** is a picture of MBBA taken with POM at RT (in the liquid crystal state) with a magnification of 100. The image confirms presence of the LC and the texture is characteristic of a nematic mesophase.

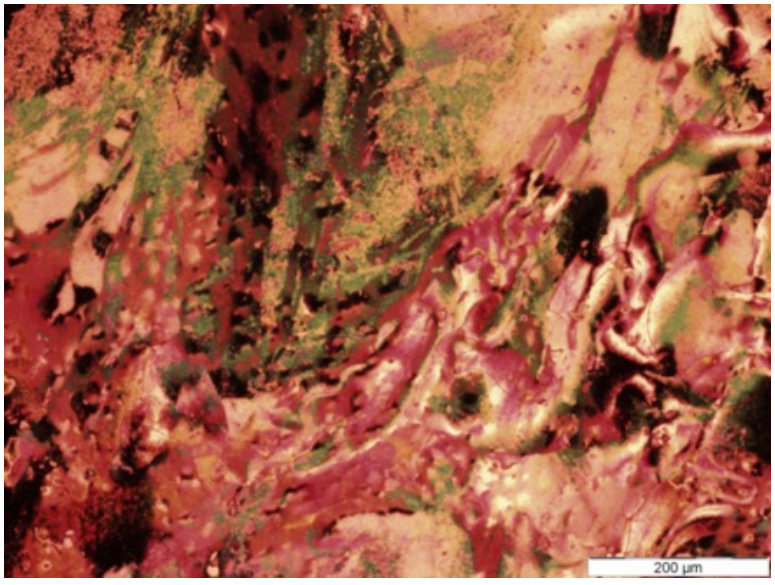

Figure 54: Picture of MBBA taken by POM at RT.

1.3.3. 4'-(6-hydroxyhexyl) oxy-[1,1'-biphenyl]-4-carbonitrile

The reaction mechanism towards the formation of MALC is illustrated in figure **55**. The base, K_2CO_3, deprotonates the alcohol group of 4-cyano-4'-hydroxyphenyl. Potassium iodide catalyses the reaction by replacing the bromide of the 6-bromohexan-1-ol. The alcoholate attacks the carbon bearing the iodine and the iodide anion is the leaving group.

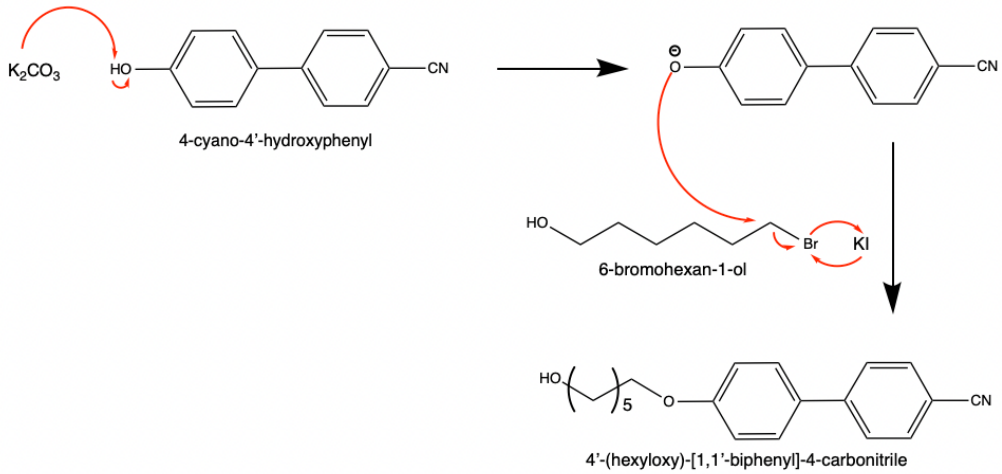

Figure 55: Mechanism for synthesis of MALC.

The ^{1}H-NMR analysis confirms the structure of MALC with high purity (97 % HPLC). The ^{1}H-NMR spectrum of MALC is shown in figure **56**.

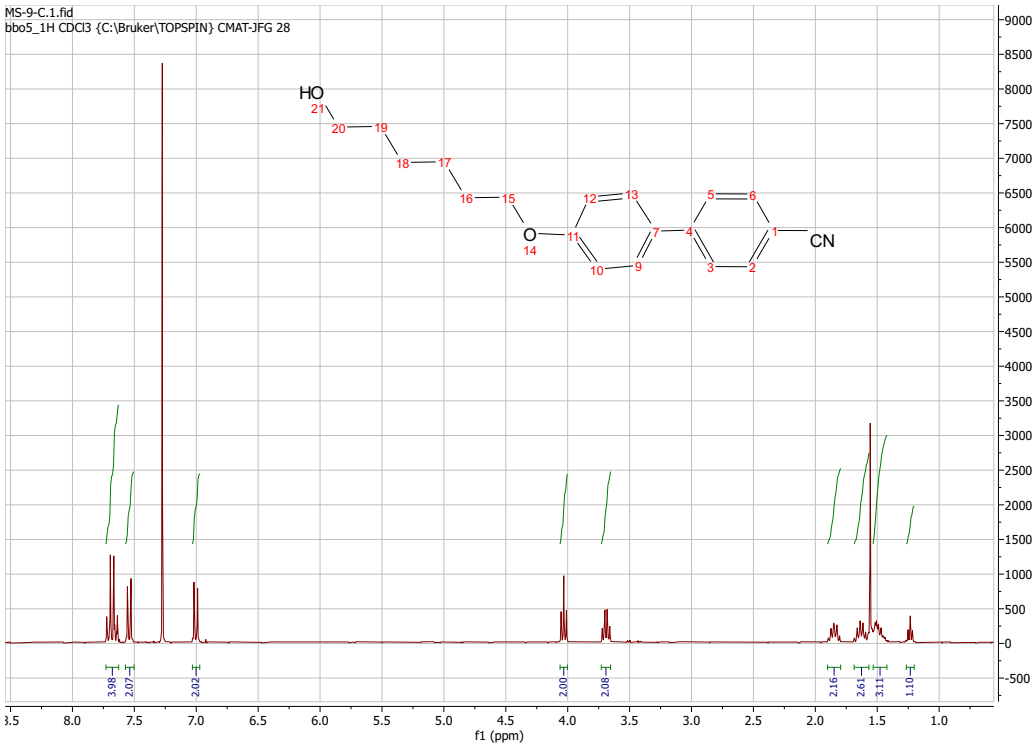

Figure 56: ^{1}H-NMR spectrum of MALC.

^{1}H-NMR [300MHz, CD_3, δ(ppm)] of MALC: 7.7 - 7.6 (m, 4H, aromatic), 7.6 - 7.5 (m, 2H, aromatic), 7 (d, 2H, aromatic), 4 (t, 2H, H15), 3.7 (t, 2H, H20), 1.9 - 1.8 (m, 2H, H16), 1.6 - 1.2 (m, 6H, H17-18-19).

The thermal stability of MALC is measured by thermogravimetric analysis. The thermogram of MALC is shown in figure **57**. The Td (5 %) of MALC is 366.9 °C. Above this temperature MALC is no longer considered stable. At 500 °C only 10 % of the product remains. The signal noise visible on the degradation curve are not of chemical origin. They are due to the vibration of the balance because of the laboratory conditions during the measurement.

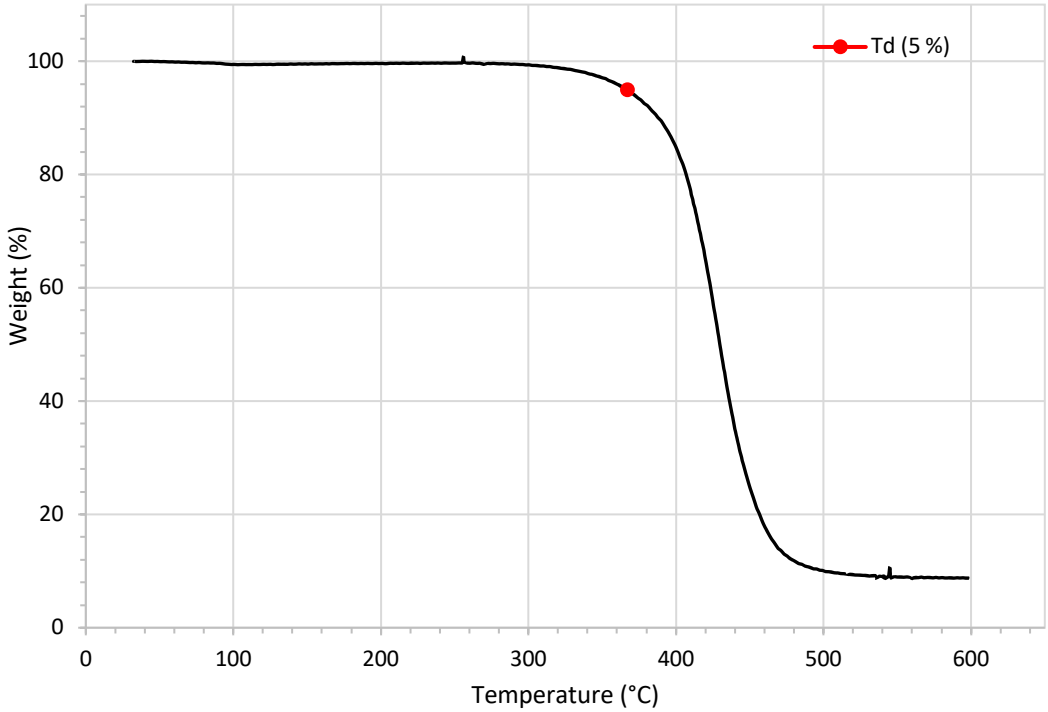

Figure 57: Thermogram of MALC, weight loss (%) vs. temperature (°C)

The DSC thermogram of MALC is shown in figure **58**. As it can be seen from the graph, there are two peaks for heating and two for cooling. The first heating peak is a larger endothermic heat exchange than the second peak. The first heating peak is located at 92 °C (Tm). This peak corresponds to the transition between the crystalline phase and the liquid crystal phase. The second heating peak at 108 °C (Tc) is the transition to the isotropic liquid. As it can be noticed on the cooling curve, the first cooling peak at 44 °C is the transition between the isotropic liquid to the liquid crystal phase. The second cooling peak at 4 °C corresponds to the transition between the liquid crystal to the crystalline phase of MBBA. There is also a shift due to the over cooling effect.

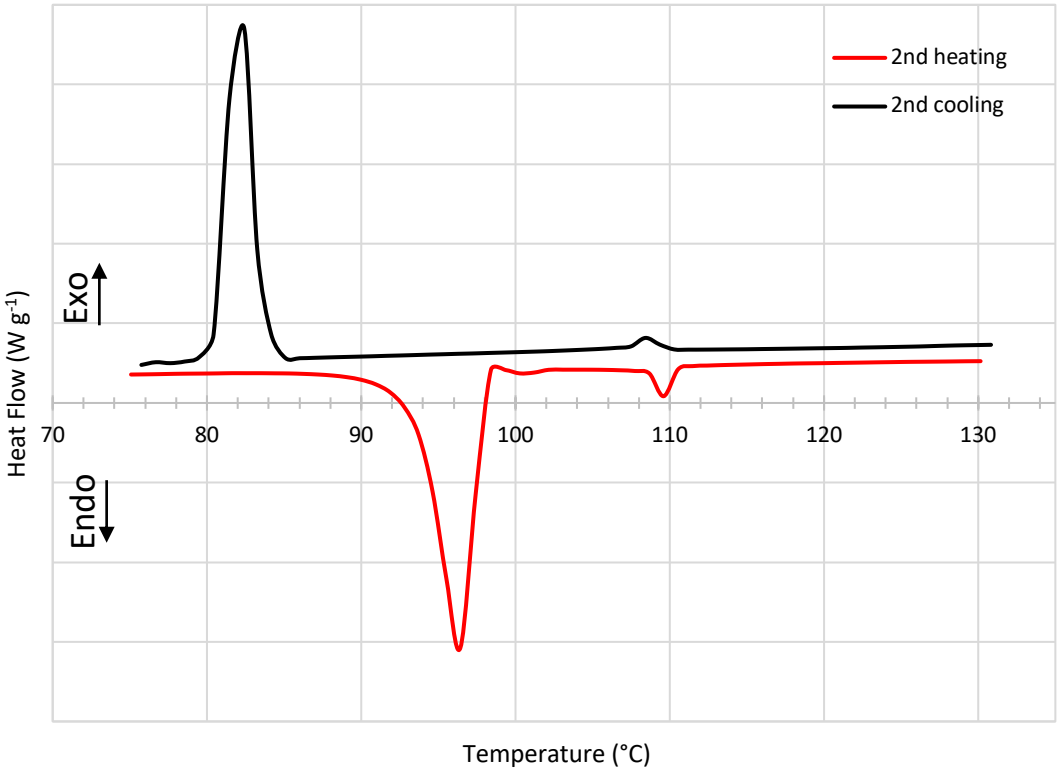

Figure 58: Thermogram of MALC, heat flow (W g^{-1}) vs. temperature (°C).

Figure **59** is a picture of MALC taken with POM at 95 °C (in the liquid crystal state) with a magnification of 100. The image is in agreement with the texture of a smectic LC.

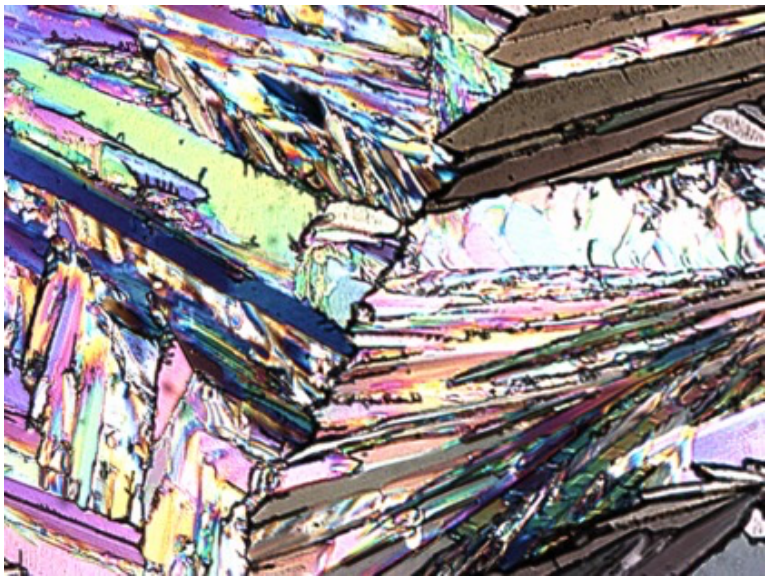

Figure 59: Picture of MALC taken by POM at 95°C.

Table **8** summarises the thermal properties obtained for each LC.

Name	**Td (5 %)** (°C)	**Liquid crystal phase** (°C)	**Structure type**
HBC	349.3	58 - 77	Smectic
MBBA	366.9	17 - 41	Nematic
MALC	346.3	92 - 108	Smectic

Table 8: Thermal properties of LCs.

2. Electrochemical and thermal characterizations of solid polymer electrolytes

To better understand the properties of LCs in SPEs, the three LCs were added in different molar ratios (0.5, 1 and 2). The polymers were added in a molar ratio of 1 and the lithium salt in a molar ratio of 2 which was kept constant. SPEs were prepared with M1/M2 RAFT, M1/M2 FR and M3 RAFT polymers with each crystal liquid to determine the best combination. Table **9** summarizes the prepared SPEs.

	Liquid crystal		Lithium Salt	Polymer matrix	
Abbreviation	**Name**	**Molar ratio**	**Molar ratio**	**Name**	**Molar ratio**
SPE-MBBA-0.5	MBBA	0,5	2	M1/M2 RAFT	1
SPE-MBBA-1	MBBA	1	2	M1/M2 RAFT	1
SPE-MBBA-2	MBBA	2	2	M1/M2 RAFT	1
SPE-MALC-0.5	MALC	0,5	2	M1/M2 RAFT	1
SPE-MALC-1	MALC	1	2	M1/M2 RAFT	1
SPE-MALC-2	MALC	2	2	M1/M2 RAFT	1
SPE-HBC-0.5	HBC	0,5	2	M1/M2 RAFT	1
SPE-HBC-1	HBC	1	2	M1/M2 RAFT	1
SPE-HBC-2	HBC	2	2	M1/M2 RAFT	1
SPE-MBBA-0.5	MBBA	0,5	2	M3 RAFT	1
SPE-MBBA-1	MBBA	1	2	M3 RAFT	1
SPE-MBBA-2	MBBA	2	2	M3 RAFT	1
SPE-MALC-0.5	MALC	0,5	2	M3 RAFT	1
SPE-MALC-1	MALC	1	2	M3 RAFT	1
SPE-MALC-2	MALC	2	2	M3 RAFT	1
SPE-HBC-0.5	HBC	0,5	2	M3 RAFT	1
SPE-HBC-1	HBC	1	2	M3 RAFT	1
SPE-HBC-2	HBC	2	2	M3 RAFT	1

Table 9: Composition of prepared SPEs

2.1. Electrochemical impedance spectroscopy experiments

The Arrhenius Plot for M3 RAFT is shown in figure **60**. It represents the best conductivity results obtained for SPE containing MALC, HBC and MBBA with M3 RAFT as polymer. With this graph, a comparison between the LCs can be made. As it can be seen, the best conductivities is obtained for SPE-MALC-1. Indeed, the conductivity curve of SPE-MALC-1 outperforms the other two curves whatever the temperature. SPE-MALC-1 is the SPE made of M3 RAFT as polymer matrix with MALC as LC in a molar ratio of 1.

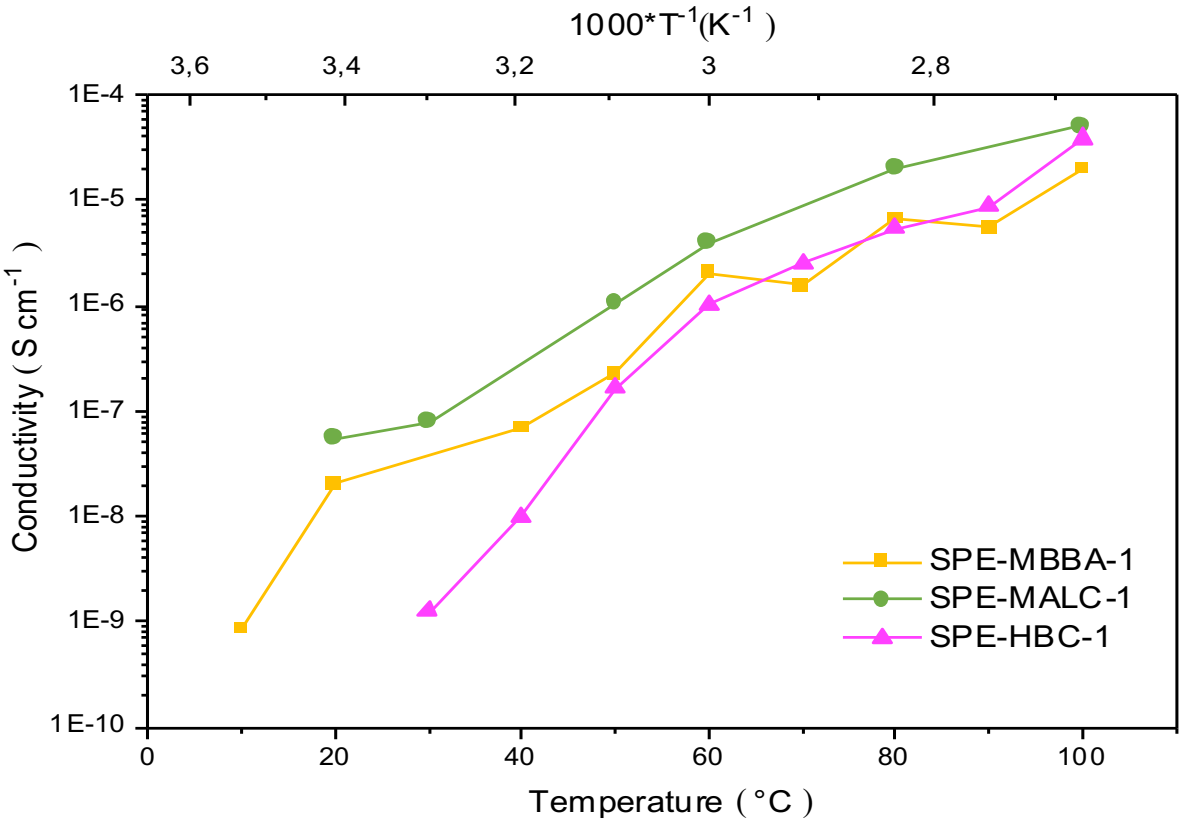

Figure 60: Arrhenius Plots for comparison of conductivity between LCs for SPE composed of M3 RAFT.

The conductivities of these SPEs are in range of 10^{-8} - 10^{-9} S cm^{-1} at RT until 40 °C. After this temperature, the conductivities increase until reaching 10^{-5} - 10^{-6} S cm^{-1}. A table of conductivities is available in the attachment. As it can be seen in the graph, the conductivity of SPE-MALC-1 is higher than SPE-MBBA-1 or SPE-HBC-1. This could indicate that conduction pathways for lithium ions are better defined for MALC containing samples.

The Arrhenius graph for M1/M2 RAFT is shown in figure **61**. It shows the best conductivity results obtained for MALC, HBC and MBBA mixed with M1/M2 RAFT as polymer matrix. With this graph, a comparison of the LCs can be made. As it can be seen, the best conductivity is obtained for the SPE-MBBA-1. Indeed, the conductivity curve of SPE-MBBA-1 is higher than the other two curves. SPE-MBBA-1 is a SPE made of M1/M2 RAFT as polymer matrix with MBBA as LC in a molar ratio of 1.

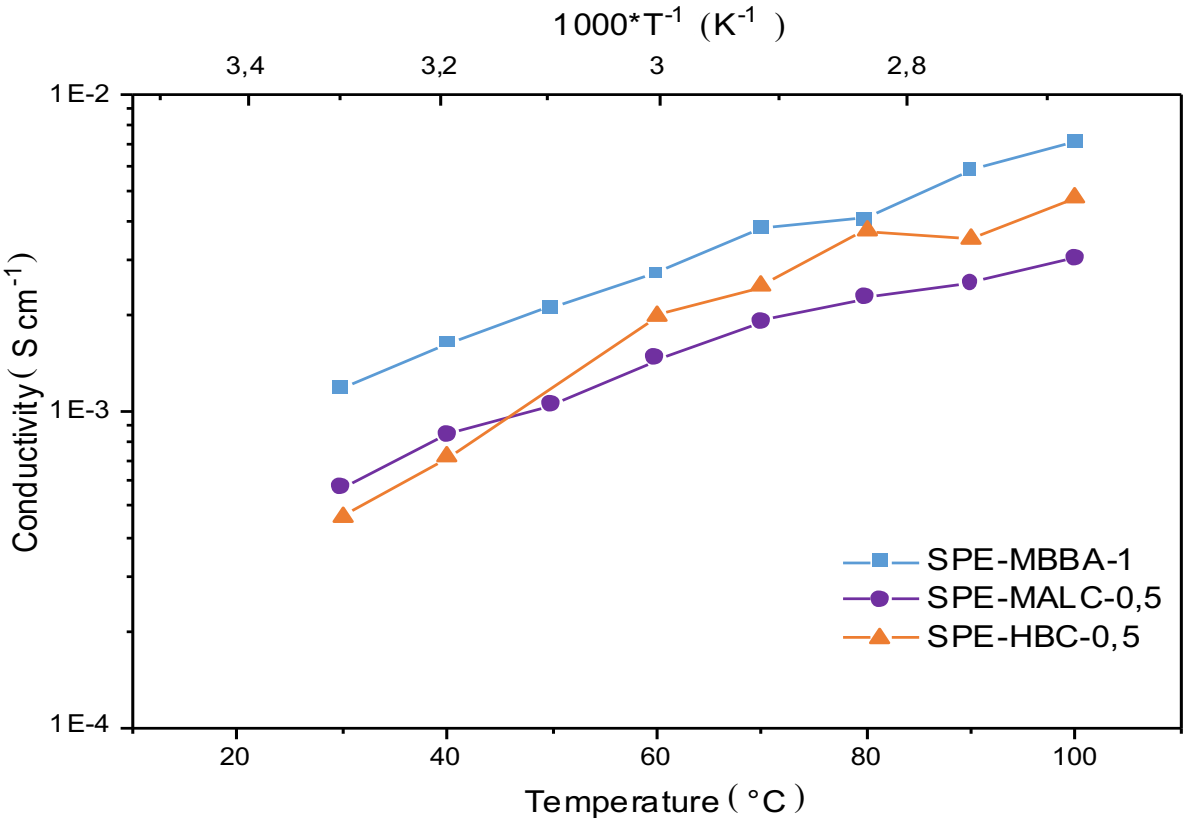

Figure 61: Arrhenius Plots for comparison of conductivity between LCs for SPE composed of M1/M2 RAFT.

The conductivities of SPEs are in range of 10^{-3} - 10^{-4} S cm^{-1} at different temperatures. A table of conductivities is available in the attachment. As it can be seen in the graph, the conductivity of SPE-MBBA-1 is higher than SPE-MALC-0.5 or SPE-HBC-0.5. The explanation that MBBA provides the best result is probably because it is in the isotropic liquid state at most of the investigated temperatures and it facilitates contact between the electrolyte and the electrodes, which increases conductivity.

It is also necessary to prove that the presence of liquid crystals improves the ionic conductivity. SPEs were thus prepared in the same way as the previous samples but without liquid crystals (M1/M2 RAFT + LiTFSI and M3 RAFT + LiTFSI) in order to compare their conductivities with those of SPE-MBBA-1 and SPE-MALC-1. The Arrhenius plot, shown in figure **62**, compares the obtained conductivity curves. As it can be seen, the conductivity curve of SPE-MBBA-1 is much higher than that of SPE-MALC-1. SPE-MBBA-1 is composed of cyclocarbonate, and ethylene oxide moiety known to improve the conductivity. In addition, the boronate group complexes the lithium salt anion, facilitating the circulation of Li^+ cations in the electrolyte. While SPE-MALC-1 composed of M3 RAFT as polymer contains only ethylene

oxide groups. The conductivity of SPE-MBBA-1 is in the range of 10^{-3} S cm^{-1} at RT. Conductivity tables are available in the attachment. It is also necessary to prove that the presence of liquid crystals has improved the conductivity performance. The grey curve is that of the M3 RAFT SPE without the liquid crystal (M3 RAFT + LiTFSI). In the case of SPE-MALC-1, one can notice that the green curve is higher than the grey one. The conductivity increased from 10^{-8} to 10^{-6} S cm^{-1} with the liquid crystal at 50 °C. The presence of the liquid crystal in the case of RAFT M3 notably improves the ionic conductivity. The black curve in figure **62** corresponds to the SPE of M1/M2 RAFT without liquid crystal (M1/M2 RAFT + LiTFSI). For the M1/M2 RAFT case, the improvement is not as important (compare black and blue curve in figure **62**) as for the M3 RAFT.

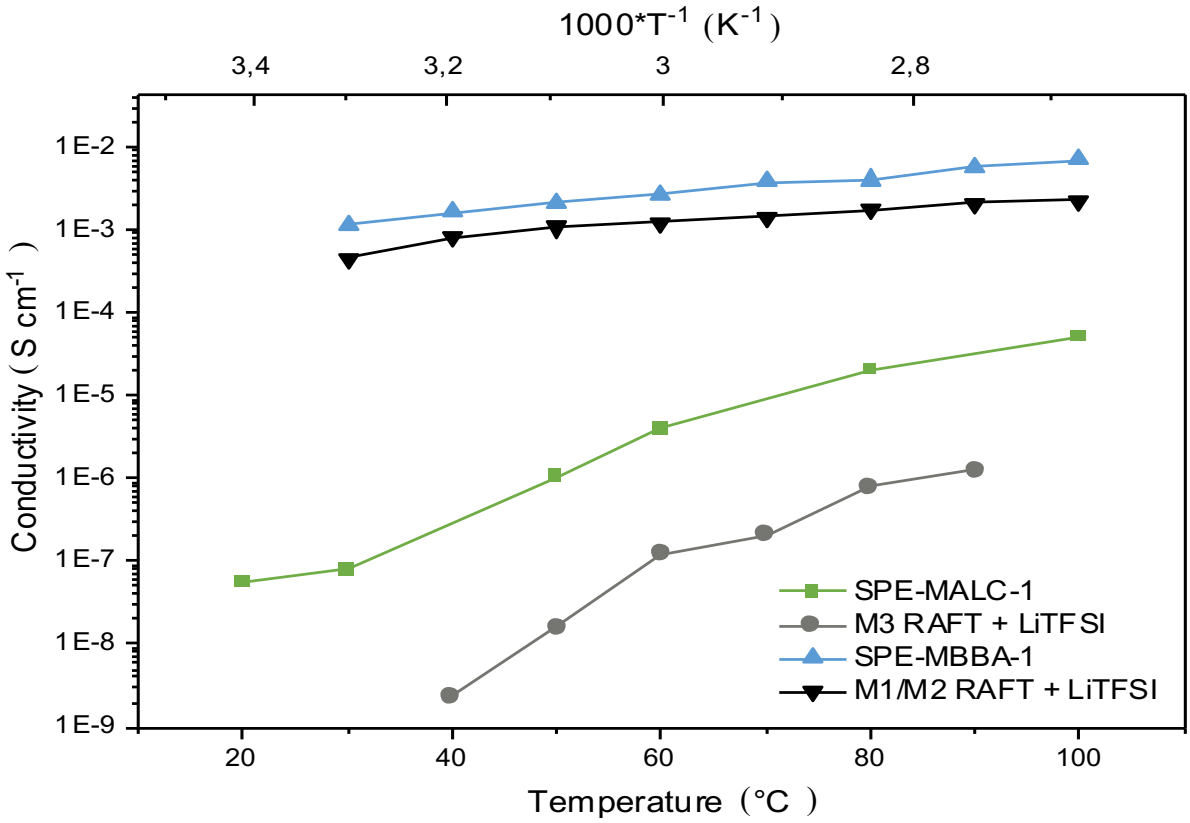

Figure 62: Arrhenius Plots for comparison of conductivity between SPEs with and without LCs.

As the best results are obtained for SPE-MBBA-1. The work was continued only with M1/M2 as polymer matrix. A solid polymer electrolyte with the same composition as SPE-MBBA-1 was prepared using the M1/M2 FR copolymer instead of the M1/M2 RAFT. The aim is to know whether the presence of the CTA for the RAFT M1/M2 polymer influences the conductivity. The Arrhenius plot is shown in figure **63**. It compares the conductivity curves for SPEs made with M1/M2 RAFT and M1/M2 FR. As it can be seen from this graph, the presence of the CTA

does not really influence the conductivity. Indeed, the conductivities of M1/M2 RAFT or FR are of the order of 10^{-3} S cm^{-1}. A table of conductivities is available in the attachment. It can be concluded that it is not necessary to have a copolymer synthesised by the RAFT method.

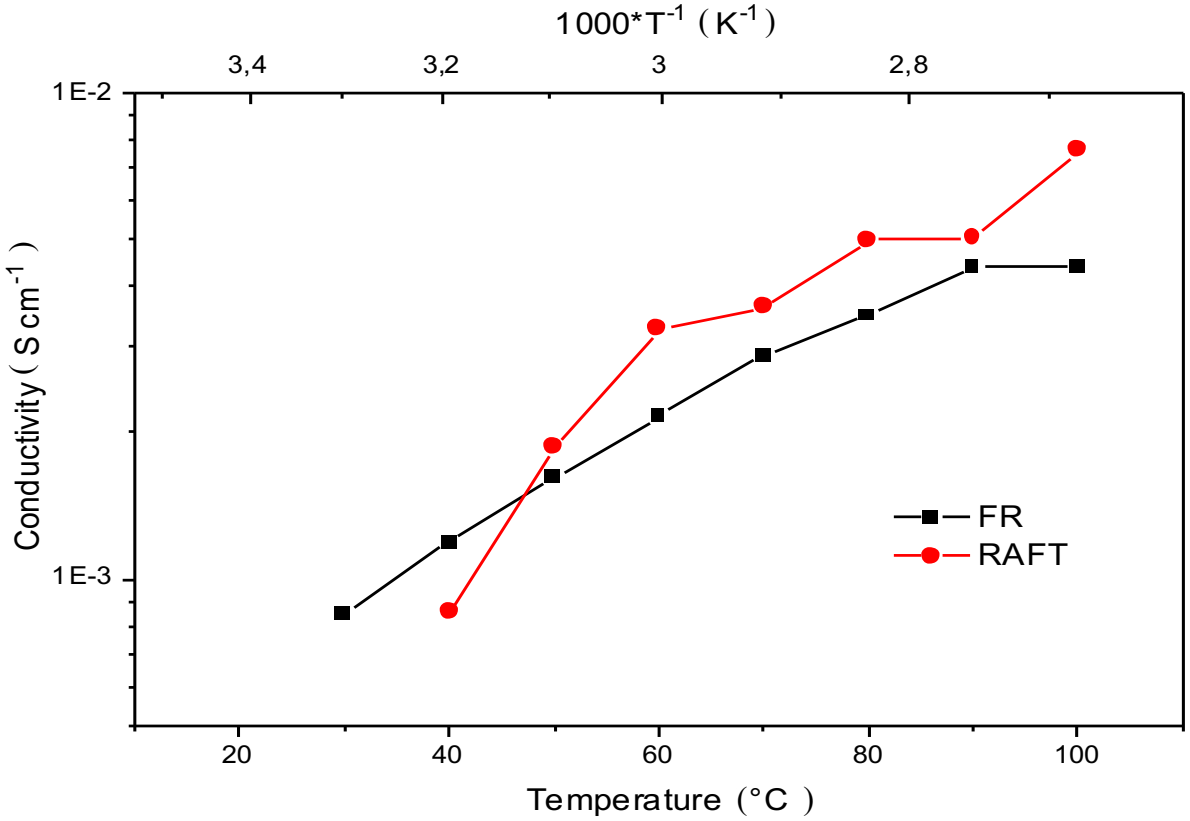

Figure 63: Arrhenius Plots for comparison of conductivity between M1/M2 RAFT or FR.

Finally, the conductivity of the SPE-MBBA-1 using a glass fiber or teflon spacer is compared. Measurements without spacer showed only short circuits. Indeed, the mechanical properties are poor with the addition of the liquid crystal, requiring the use of a spacer. The Arrhenius plot is shown in figure **64**. The glass fiber cells gave the best results with a conductivity close to 10^{-3} S cm^{-1}, while the teflon spacer cells gave a conductivity of 10^{-6} S cm^{-1} over a wide temperature range. The glass fiber provides better conductivity because the electrolyte is in contact with the stainless-steel disk. For the teflon spacer, the thickness of the electrolyte must be sufficient to have contact between the SPE and the stainless-steel disk. A table of conductivities is available in the attachment.

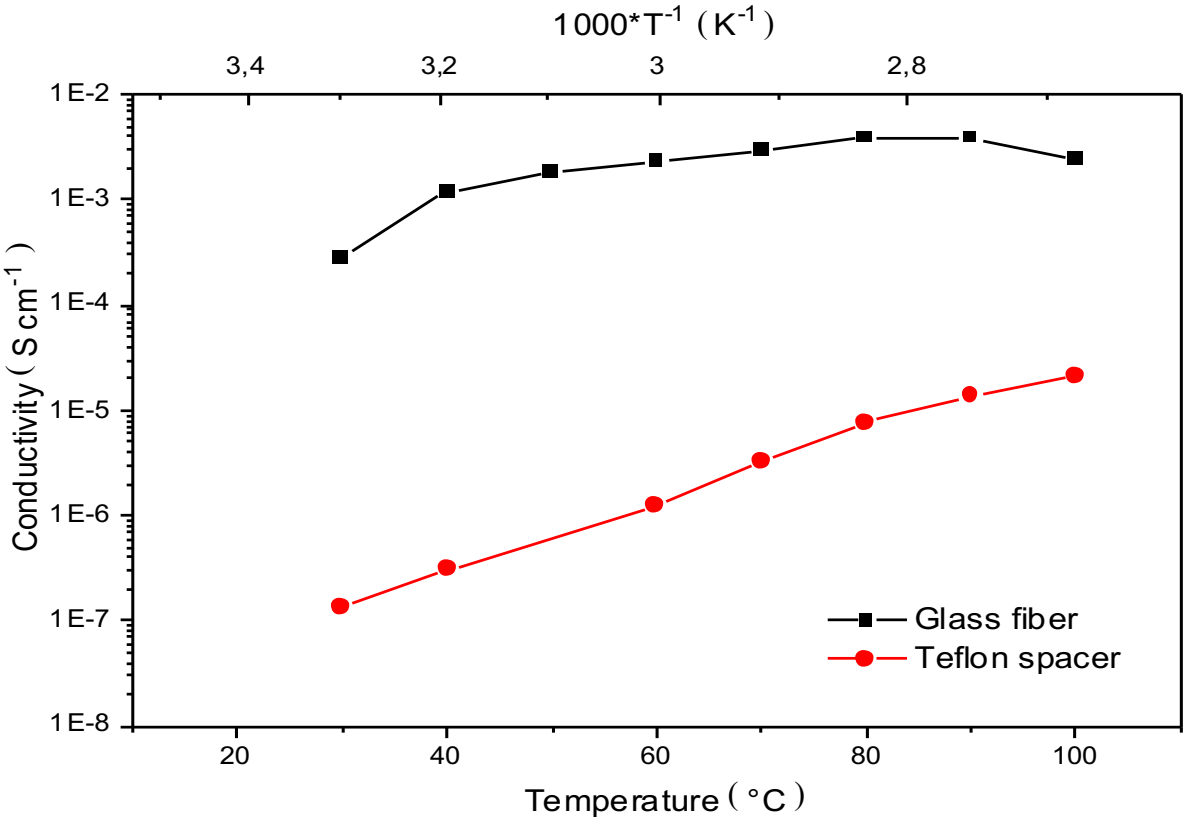

Figure 64: Arrhenius Plots for comparison between glass fiber or teflon spacer.

As seen in the previous points, the best conductivity results were obtained for a SPE composed of M1/M2 RAFT as polymer matrix, MBBA in a molar ratio of 1 as liquid crystal and glass fiber as separator. The conductivity is in the order of 10^{-3} S cm^{-1} at RT, which is remarkable.

2.2. Differential scanning calorimetry

The DSC thermograms of SPE-MBBA-1 and SPE-MALC-1 are shown in figure **65**. For SPE-MBBA-1, an exothermic heat exchange is observed at -60 °C, indicating crystallisation. At 14 °C and 20 °C there are two endothermic heat exchange peaks, which are characteristic of the MBBA transition. The first peak corresponds to the crystalline transition to the liquid crystal phase (Tm) and the second peak to the transition to the isotropic liquid phase (Tc). The heat exchange of the first peak (14 °C) is greater than that at 20 °C. Compared to the DSC analysis of MBBA, the peaks are shifted to lower temperatures. For SPE-MBBA-1, no glass transition peak is observed between -80 °C and 125 °C. In the case of SPE-MALC-1, there is only one peak at 58 °C. This is an endothermic heat exchange peak. It is necessary to carry out a POM analysis to determine the thermal transition of SPE-MALC-1 at this temperature.

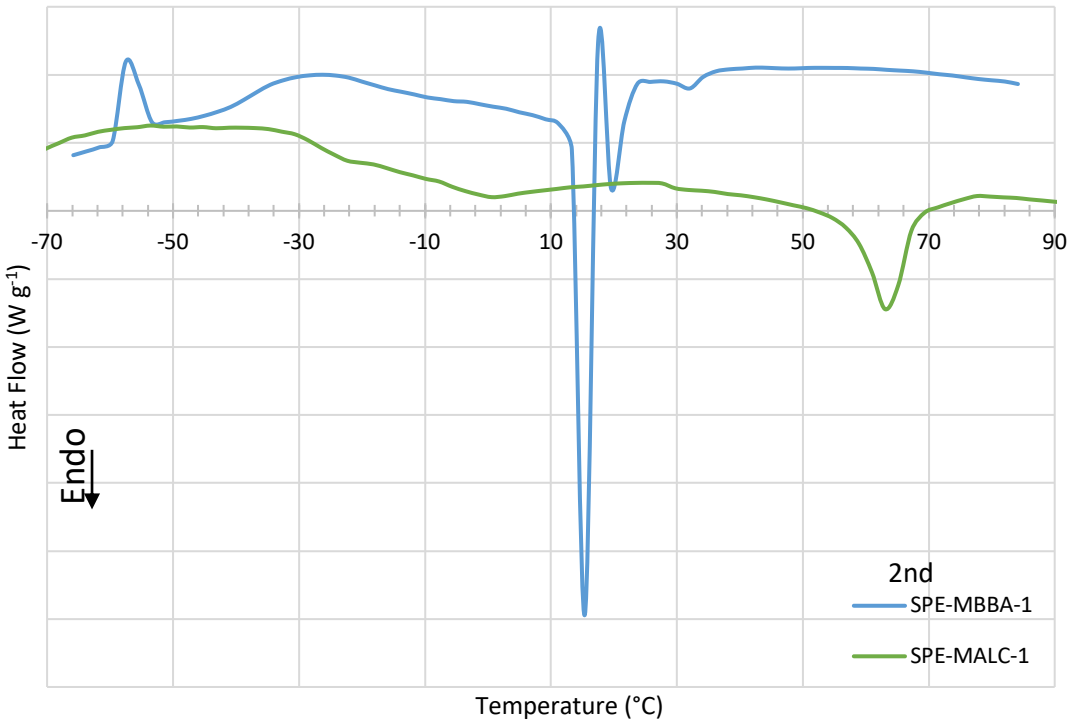

Figure 65: Thermograms of second heating of SPEs heat flow (Wg^{-1}) vs. temperature (°C).

2.3. Thermogravimetric analysis

The thermal stability of SPE-MBBA-1 and SPE-MALC-1 was measured by thermogravimetric analysis. The thermographs of SPE-MBBA-1 and SPE-MALC-1 are shown in figure **66**. The Td (5 %) of SPE-MBBA-1 is 113.2 °C, and the Td (5 %) of SPE-MALC-1 is 278.9 °C. The degradation temperature of SPE-MBBA-1 is lower than that of SPE-MALC-1 but is still above the temperature used in batteries. The curve of SPE-MBBA-1 shows two degradation mechanisms. The first drop corresponds to 42 % degradation (259 °C). This may be due to the presence of MBBA. Indeed, on the MBBA thermogram, these two mechanisms were observed. An analysis of the gases produced could determine the chemical nature of this degradation. On the graph, one can also notice that SPE-MBBA-1 degrades less quickly than SPE MALC-1. The SPE-MALC-1 curve is steeper than that of SPE-MBBA-1. For SPE-MBBA-1 at 500 °C, 15 % of the initial product remain, whereas for SPE-MALC-1 only 5 % remain.

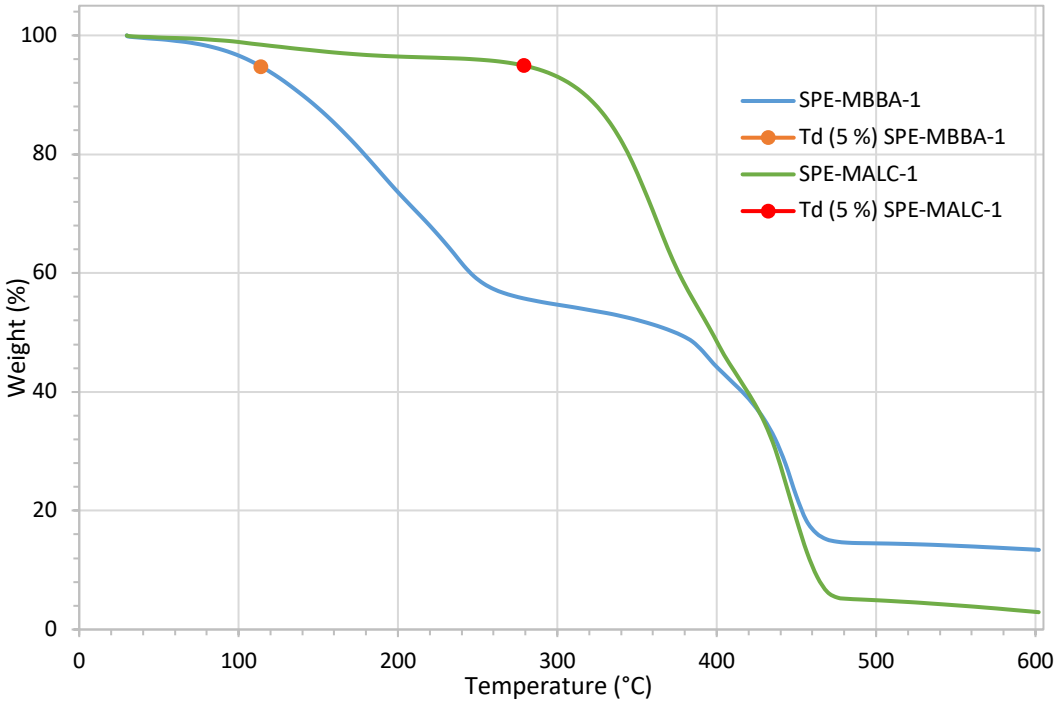

Figure 66: Thermograms of SPEs, weight loses (%) vs. temperature (°C).

2.4. Polarised optical microscopy

In order to assess the miscibility of the different components in the electrolytes as well as the phase transitions of the LC, selected samples were analysed by POM (SPE-MBBA-1, SPE-MALC-1, M3 RAFT + LiTFSI and M1/M2 RAFT + LiTFSI).

M3 RAFT + LiTFSI at RT (Figure **67**) is black with white dots. The white dots can be lithium salt crystals. They stand out against the black background because of the birefringent property of the crystals.

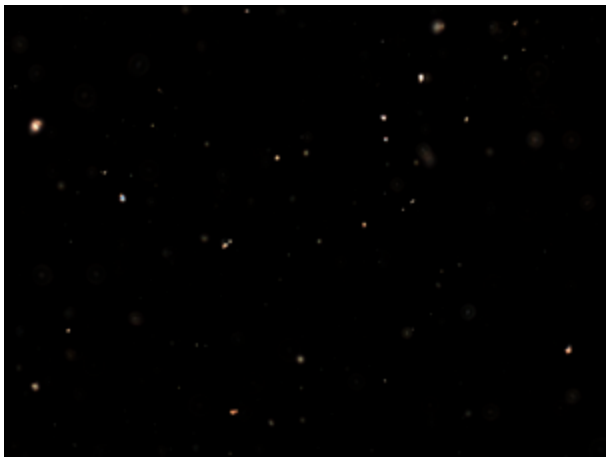

Figure 67: Picture of M3 RAFT + LiTFSI taken by POM at RT.

As it can be seen in figure **68** (left), SPE-MALC-1 at RT shows a black background with some colours. The black is due to the presence of the isotropic polymer domains. The coloured areas are related to the presence of birefringent liquid crystal. SPE-MALC-1 is therefore a material consisting of immiscible polymer and LC domains. When SPE-MALC-1 is heated, it can be observed that the compound starts to have a certain fluidity. At 75 °C, the liquid crystals are in the isotropic liquid state (see DSC thermogram in figure **65**), leaving only some white dots, it as can be seen from the figure **68** (right). The white dots can be aggregates of lithium salts.

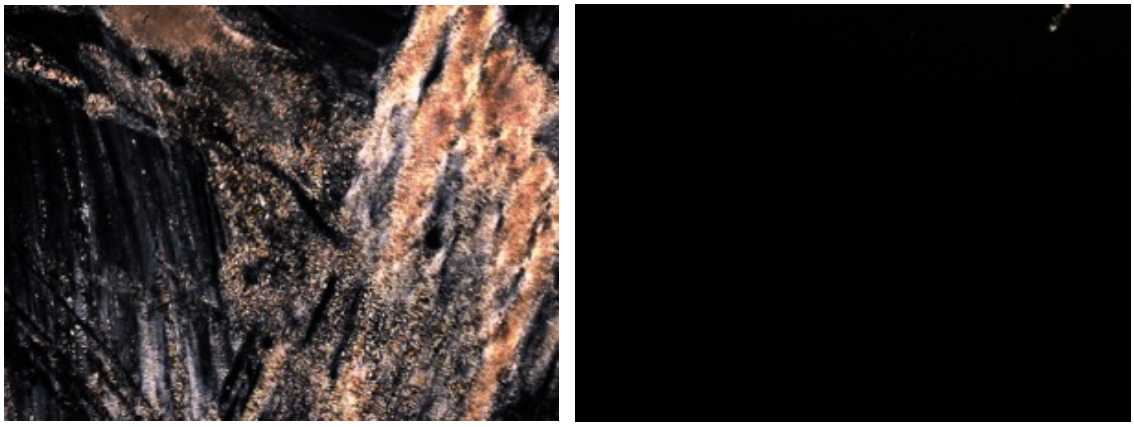

Figure 68: Picture of SPE-MALC-1 taken by POM at (left) RT and (right) 75°C.

SPE-MBBA-1 and M1/M2 RAFT + LiTFSI at RT reveal a black background with white dots (figure **69**). The black background is the signature if isotropic polymer and LC domains. The white dots can be the lithium salt crystals which are birefringent. There is no difference between SPEs with and without LC. Unfortunately, it is not possible to visualize the transition of the LC because it is not possible to cool the sample below room temperature during the POM analysis. Following the DSC analysis of SPE-MBBA-1 (see figure **65**), the MBBA transition peaks are still present below 20 °C. This may be an indication of immiscibility between the polymer and the LC components in the SPE-MBBA-1 sample. This should be confirmed by a POM analysis below 20 °C where MBBA in crystalline or liquid crystal form could be observed.

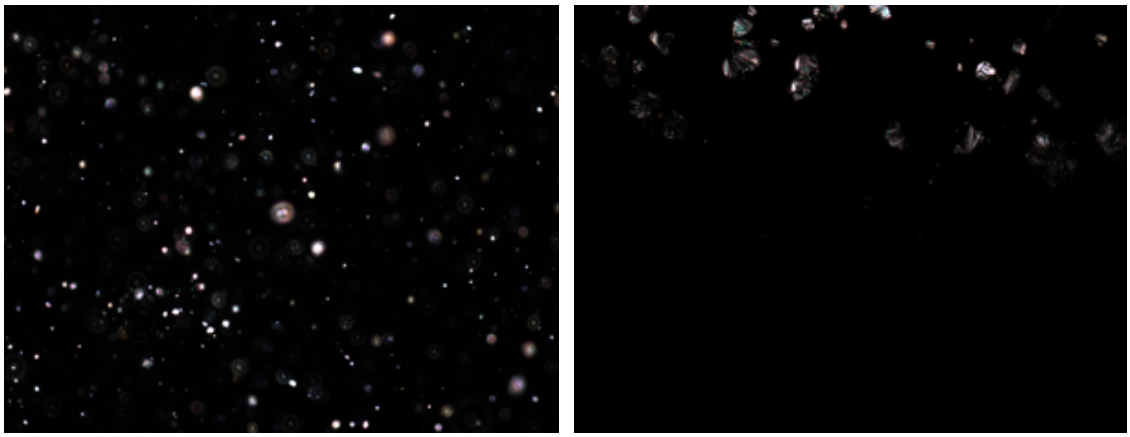

Figure 69: Pictures of SPE-MBBA-1 (left) and M1/M2 RAFT + LiTFSI (right) taken by POM at RT.

In conclusion, the POM analysis of SPEs made revealed that those system are formed of a polymer and a LC phase, the properties of the LC phase being retained in the SPEs.

2.5. Linear sweep voltammetry

The electrochemical stability of SPE-MBBA-1 is measured by LSV analysis. The LSV diagram is shown in figure **70**. The orange curve represents the oxidation of SPE-MBBA-1, and the blue represents the reduction of SPE-MBBA-1. A degradation of the SPE starts directly (see zoom of the LSV diagram in figure **70**). Nevertheless, LFP/SPE-MBBA-1/ Lithium coin cells were successfully cycled in the voltage window of 3 - 3.8 V.

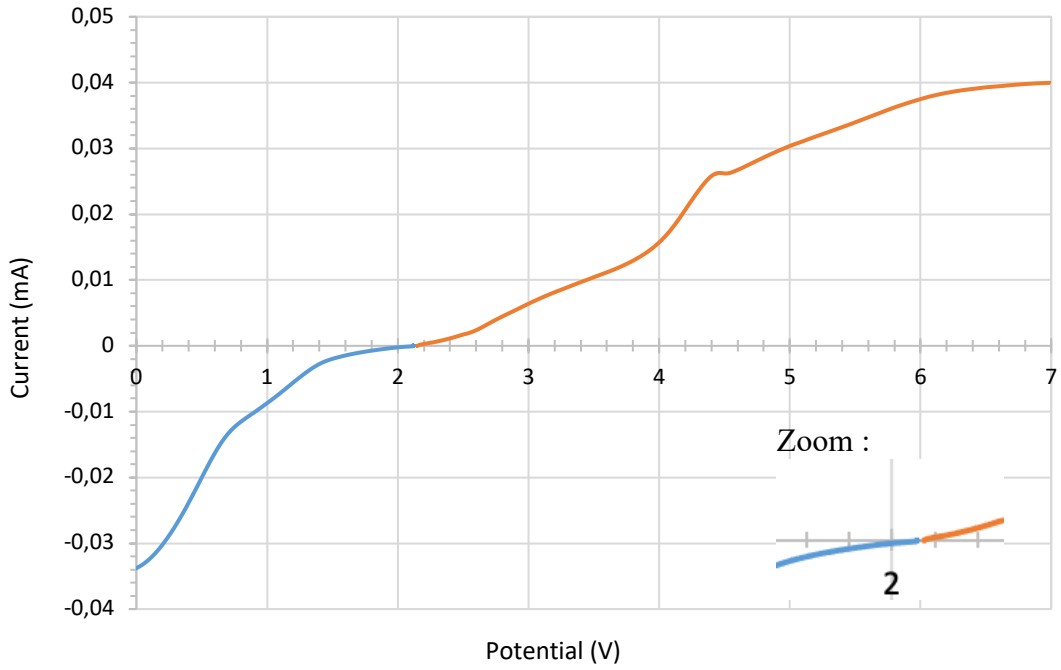

Figure 70: LSV diagram of SPE-MBBA-1.

3. Electrochemical characterization of catholytes

3.1. Charge-discharge experiments

First, a coin cell was tested using the usual liquid electrolyte for LMB (EC/DMC) just to verify if the catholyte can be used with the M1/M2 polymer as binder. The advantage of using M1/M2 RAFT as a binder is that the binder, usually polyvinylidene fluoride (PvdF), can be eliminated as dead material in the battery and enables ionic conduction inside the cathode. LFP was used as cathode material. The conditions for experiments are available in the attachment part.

For this test, different currents were used with 10 charge/discharge cycles at each C-rate. The C-rates are: 1 C, 2 C, 5 C and finally 1 C. The last 1 C shows the capacity degradation after higher C-rates. The current to test depends on the capacity of catholyte and the C-rate. Two coin cells were assembled; Cell-1 and Cell-2. Cell-1 has a voltage of 1.6 V while Cell-2 has a voltage of 1.8 V. The graph with the results of Cell-1 is shown in figure **71**. The red line stands for the efficiency of charge/discharge. The black curve stands for the discharge specific capacity. The black curve with orange dots stands for the first ten cycles. The black curve with yellow dots stands for the for cycles 11 to 20, the black line with purple dots for cycles 21 to 30. And cycles 31 to 40 are represented by the black line with green dots.

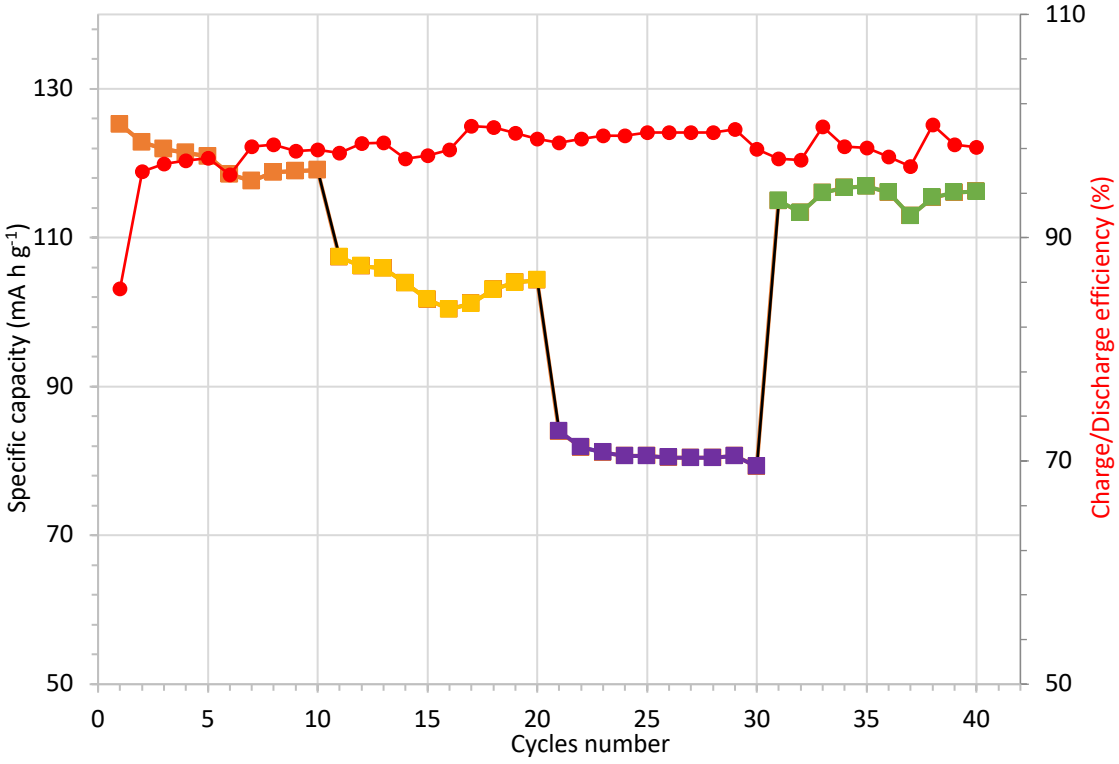

Figure 71: Charge/discharge stability graph of Cell-1.

As it can be seen in figure **71**, the charge/discharge efficiency starts with 85 %. After the fisrt cycle, the efficiency is always in the 95 % range during the 40 cycles. It can also be seen that the specific capacity is 120 mAh g^{-1} after ten cycles at 1 C, meaning a 30 % capacity loss. Cycles at 2 C have a specific capacity of 105 mA h g^{-1} resulting in a 40 % capacity loss. For the next ten cycles at 5 C we can see that the capacity has decreased again, 80 mAh g^{-1}, with a loss of 45 %. The greatest capacity loss occurs during the first ten cycles. In the last cycles at 1 C the specific capacity is 115 mAh g^{-1}, which is almost the same as the capacity obtained in the first ten cycles. The fact that the reached capacity stay constant between C-rates shows that the cell can be cycled normally even at high speeds (5 C). After 40 cycles, the capacity retains almost the initial value showing that the degradation during these cycles is negligible. The fact that the specific capacity is 120 mAh g^{-1} instead of 170 in the first cycle can be explained by the fact that not all the active LFP material is accessible or distributed in the catholyte. It can be concluded that our system works!

Since the cell with the liquid electrolyte worked fine, the M1/M2 RAFT polymer can be tested as binder and ion conductor inside the cathode material. To have a comparison, the same C-rates as for the liquid electrolyte were tested. Two coin cells were assembled; Cell-3 and Cell-4. The graph with the results of Cell-3 is shown in figure **72**. The red line stands for the efficiency of charge/discharge. The black curve stands for the discharge specific capacity. The black curve with orange dots stands for the first ten cycles. The black curve with yellow dots stands for the for cycles 11 to 20, the black line with purple dots for cycles 21 to 30. And cycles 31 to 40 are represented by the black line with green dots.

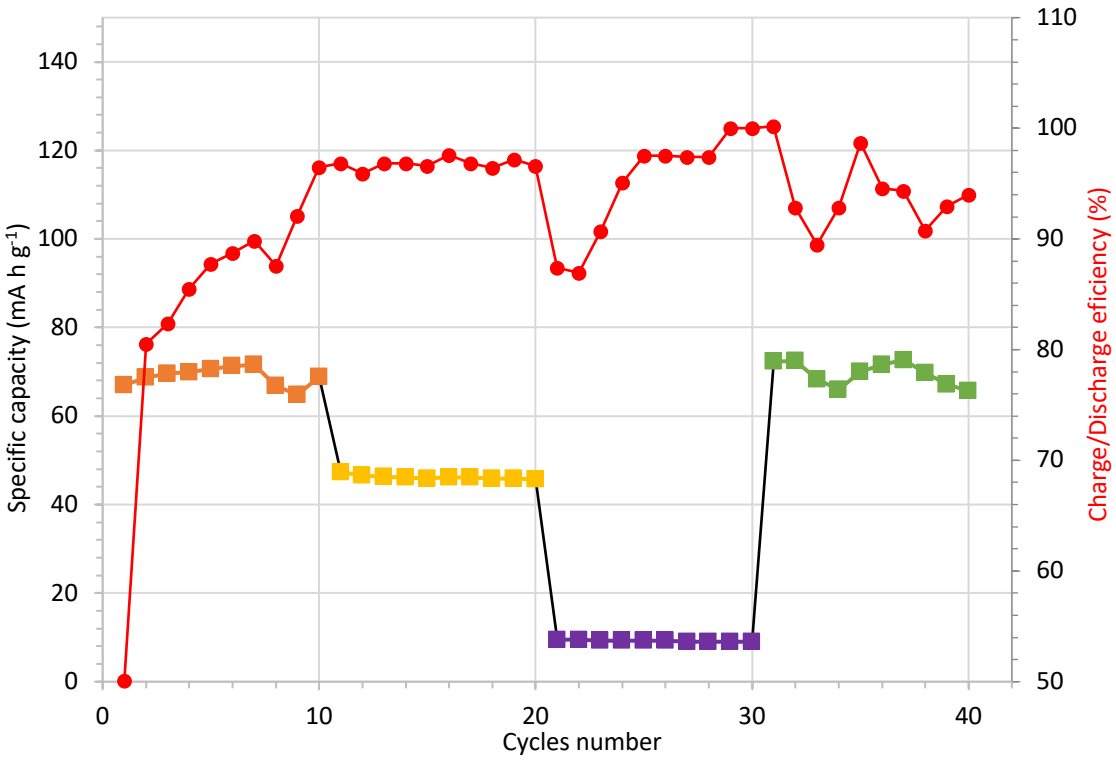

Figure 72: Charge/discharge stability graph of Cell-3.

As can be seen from the figure **72**, the charge/discharge efficiency starts at 50 %. During the first ten cycles, the efficiency increases to 95 % for the following cycles. After the ten cycles at 2 C and 3 C, there is a 5 % drop in efficiency. This decrease may be due to the change in voltage. It can also be seen that the specific capacity is 70 mAh g^{-1} after ten cycles at 1 C, which means a 60 % capacity loss. The cycles at 2 C have a specific capacity of 26 mAh g^{-1}, which means a capacity loss of 75 %. For the next ten cycles at 5 C, one can observe that the capacity has decreased further, 10 mAh g^{-1}, with a loss of 95 %. The greatest capacity loss occurs during the first ten cycles. In the last cycles at 1 C, the specific capacity is the same as that obtained in the first ten cycles. After 40 cycles, the capacity retains almost the initial value showing that the degradation during these cycle is negligible. The capacities obtained with SPE-MBBA-1 are lower than those with the liquid electrolyte. One possibility for this difference is that the interfacial contact with the SPE is not as good than when using the liquid electrolyte.

Figures **73** and **74** show the difference in voltage behavior during cycling when using the liquid electrolyte or the SPE. This analysis was carried out under the same conditions as for the charge/discharge tests. Different C-rates were tested: 1 C, 2 C, 5 C and finally 1 C. The blue dots correspond to the charge and discharge of the first cycle at 1C. The greens for those of

the 11th cycle, the reds for the 21st cycle. And the black dots correspond to the charge/discharge of the 31st cycle. Figure **73** is for the Cell-1 and figure **74** is for the Cell-3.

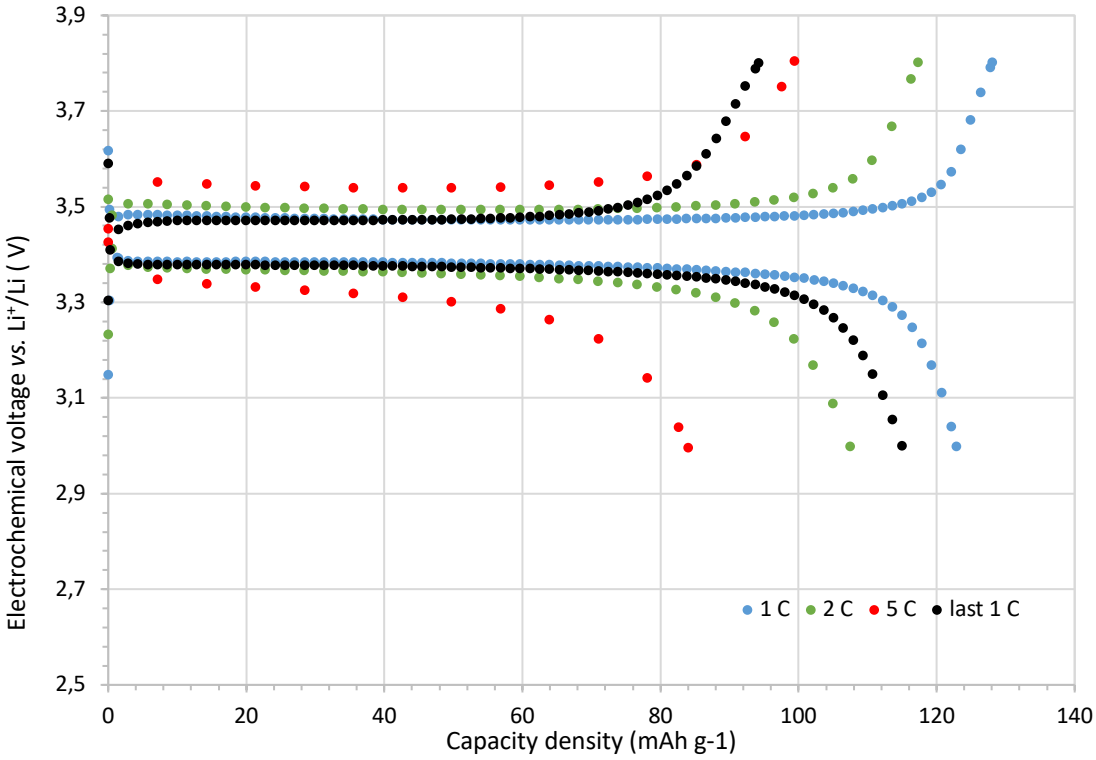

Figure 73: Charge/discharge graph of Cell-1.

In figure **73**, the curves upwards are the charge curves at different C-rates and those downwards are the discharge curves. A reversibility between charge and discharge at different C-rates can be observed. As the charge/discharge rate increases, the capacity loss increases. The 1 C and last 1 C curves are quite close, proving that the catholyte is not degraded even after cycling at highest speed (5 C).

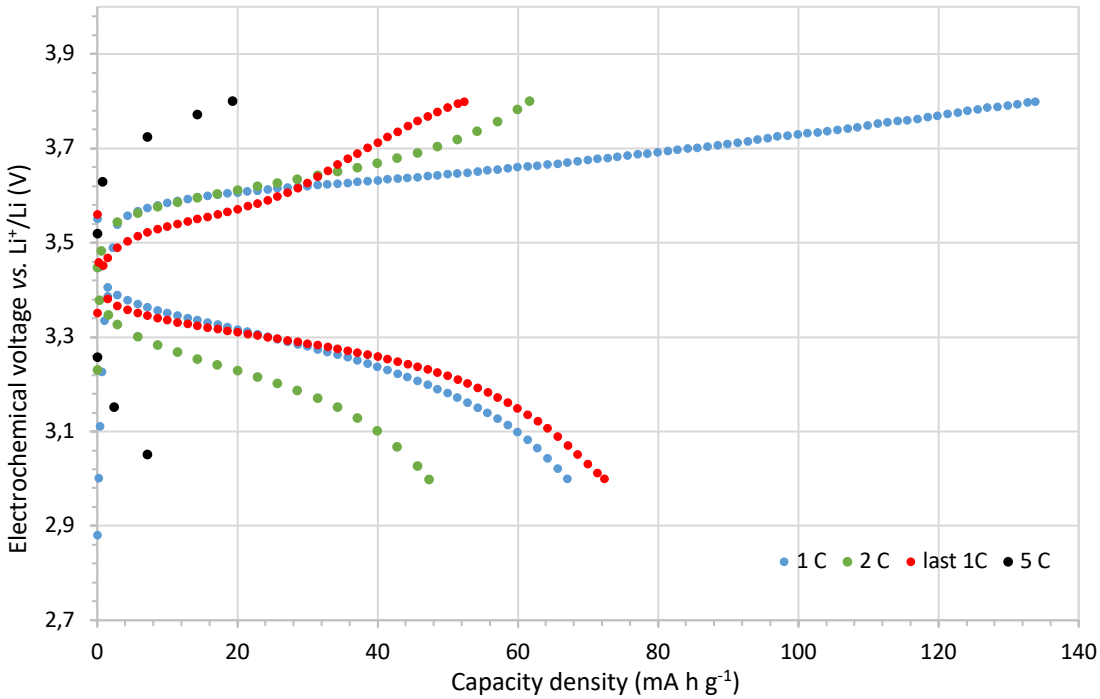

Figure 74: Charge/discharge graph of Cell-3.

In figure **74**, the curves upwards are the charge curves at different C-rates and those downwards are the discharge curves. Reversibility is more difficult to observe than with the liquid electrolyte. There is a loss of capacity between charge and discharge. The discharge curve at 1 C no longer reaches 120 mAh g^{-1}. There is also a greater loss of capacity as the charge/discharge rate increases. By comparing figures **73** and **74**, one can conclude that the capacity loss is greater with the SPE.

V. Conclusion and outlooks

The experiments carried out in this master thesis allowed the preparation of a solid polymer electrolyte providing a conductivity of 10^{-3} S cm^{-1} at room temperature. This solid polymer electrolyte is composed of M1/M2 RAFT polymer with MBBA as liquid crystal. Using M1/M2 RAFT to make the solid polymer electrolyte instead of M1/M2 FR does not bring an improvement in conductivity. The ionic conductivity of the solid polymer electrolytes was improved by the addition of liquid crystals. This effect is higher in the case of SPE-MALC-1 with a change in conductivity from 10^{-8} to 10^{-6} S cm^{-1} upon addition of MALC. This improvement is not as visible in the case of SPE-MBBA-1. Indeed, in this case, the conductivity remained in the same range when MBBA was added. SPE-MBBA-1 was selected for further experiments because it has a conductivity close to that of liquid electrolytes. The polarised optical microscopy analysis of SPE-MBBA-1 and SPE-MALC-1 showed that the polymer, liquid crystal, and lithium salt are (partly) immiscible. This was confirmed by differential scanning calorimetry measurements. Indeed, the thermograms showed the characteristic transitions of the polymer but also those of the liquid crystal. SPE-MBBA-1 offers thermal stability up to 113 °C. The electrochemical stability did not impart any results that could be exploited. As the solid polymer electrolyte had proven its ionic conduction efficiency, a catholyte in which the M1/M2 copolymer substitutes the binder, was prepared in order to assemble LFP-based half cells. The half cells were charged and discharged successfully for 40 cycles. A loss of capacity was clearly observed between the cells using either of a liquid electrolyte or the solid polymer electrolyte. This difference is thought to originate from a less efficient electrode/electrolyte interfacial contact in the case of the solid polymer electrolyte. Although the objective of this work to improve ionic conductivity is reached, some avenues are to be considered. Further characterization about the interaction between the liquid crystal and the polymer matrix are needed, as well as the development of strategies to align the liquid crystal molecules to improve further the ionic conduction.

Attachments

Comparative conductivity table of the best results obtained for MBBA, MALC and HBC with M3 RAFT as polymer:

	Conductivity (S cm^{-1})		
T (°C)	SPE-MBBA-1	SPE-MALC-1	SPE-HBC-1
30	/	8,00E-08	1,27E-09
40	6,89E-08	/	9,92E-09
50	2,25E-07	1,06E-06	1,65E-07
60	2,07E-06	3,97E-06	1,03E-06
70	1,55E-06	/	2,51E-06
80	6,75E-06	2,03E-05	5,41E-06
90	5,55E-06	/	8,76E-06
100	2,00E-05	5,06E-05	3,85E-05

Comparative conductivity table of the best results obtained for MBBA, MALC and HBC with M1/M2 RAFT as polymer:

	Conductivity (S cm^{-1})		
T (°C)	SPE-MBBA-1	SPE-MALC-0.5	SPE-HBC-0.5
30	1,18E-03	5,74E-04	4,86E-04
40	1,65E-03	8,44E-04	7,13E-04
50	2,13E-03	1,04E-03	/
60	2,72E-03	1,46E-03	1,99E-03
70	3,88E-03	1,92E-03	2,49E-03
80	4,05E-03	2,28E-03	3,72E-03
90	5,80E-03	2,54E-03	3,50E-03
100	6,71E-03	3,04E-03	4,74E-03

Comparative conductivity table of SPE-MBBA-1, SPE-MALC-1 and SPE made of polymer and lithium salt (LiTFSI):

	Conductivity (S cm^{-1})			
T (°C)	SPE-MBBA-1	M1/M2 RAFT + LiTFSI	SPE-MALC-1	M3 RAFT + LiTFSI
30	1,18E-03	1,09E-03	5,58E-09	/
40	1,65E-03	1,24E-03	8,00E-08	2,41E-09
50	2,13E-03	1,69E-03	1,06E-06	1,59E-08
60	2,72E-03	2,20E-03	3,97E-06	1,25E-07
70	3,88E-03	1,44E-03	/	2,12E-07
80	4,05E-03	1,75E-03	2,03E-05	8,12E-07
90	5,80E-03	2,10E-03	/	1,27E-06
100	6,71E-03	2,28E-03	5,06E-05	/

Comparative conductivity table of SPE-MBBA-1 made of M1/M2 RAFT or M1/M2 FR:

	Conductivity (S cm^{-1})	
T (°C)	RAFT	FR
30	1,18E-03	8,45E-04
40	1,65E-03	1,19E-03
50	2,13E-03	1,62E-03
60	2,72E-03	2,16E-03
70	3,88E-03	2,89E-03
80	4,05E-03	3,48E-03
90	5,80E-03	4,38E-03
100	6,71E-03	4,38E-03

Comparative conductivity table of SPE-MBBA-1 using glass fiber (GF) or teflon spacer (TS):

	Conductivity (S cm^{-1})	
T (°C)	GF	TS
30	1,18E-03	1,32E-07
40	1,65E-03	3,08E-07
50	2,13E-03	/
60	2,72E-03	1,22E-06
70	3,88E-03	3,22E-06
80	4,05E-03	7,63E-06
90	5,80E-03	1,37E-05
100	6,71E-03	2,10E-05

Charge/discharge stability test conditions for Cell-1 and Cell-2:

	LFP mass (g)	**Capacity** (Ah)	**C-rate** (1/h)	**Current to test** (A)
Cell-1	1,26E-03	2,14E-04	1C	2,14E-04
			2C	4,28E-04
			5C	1,07E-03
			1C	2,14E-04
Cell-2	1,04E-03	1,76E-04	1C	1,76E-04
			2C	3,52E-04
			5C	8,80E-04
			1C	1,76E-04

Charge/discharge stability test conditions for Cell-3 and Cell-4:

	LFP mass (g)	**Capacity** (Ah)	**C-rate** (1/h)	**Current to test** (A)
Cell-3	9,45E-04	1,61E-04	1C	1,61E-04
			2C	3,21E-04
			5C	8,03E-04
			1C	1,61E-04
Cell-4	1,40E-03	2,37E-04	1C	2,37E-04
			2C	4,74E-04
			5C	1,19E-03
			1C	2,37E-04

Literature

1. Piana, G. Electrolyte solide innovant à base de liquides ioniques pour micro-accumulateurs au lithium: réalisation par voie humide et caractérisation des propriétés de transport. 269.

2. Vlad Alexandru. LCHM2260 - Electrochemical Energy storage. (2021).

3. Miomandre, F., Sadki, S., Audebert, P. & Méallet-Renault, R. *Electrochimie : Des concepts aux applications*. (Dunod, 2014).

4. *The AES guide to lithium-ion battery test chambers*. (s. d.-a). Associated Environmental Systems | Environmental Test Chambers. https://www.associatedenvironmentalsystems.com/the-aes-guide-to-lithium-ion-battery-test-chambers

5. Muench, S. *et al.* Polymer-Based Organic Batteries. *Chem. Rev.* **116**, 9438–9484 (2016).

6. Owen, J. University of Salford, UK. 18.

7. Ye, L. & Feng, Z. Polymer electrolytes as solid solvents and their applications. in *Polymer Electrolytes* 550–582 (Elsevier, 2010). doi:10.1533/9781845699772.2.550.

8. Boaretto, N. *et al.* Lithium solid-state batteries: State-of-the-art and challenges for materials, interfaces and processing. *Journal of Power Sources* **502**, 229919 (2021).

9. Xiao, J. How lithium dendrites form in liquid batteries. *Science* **366**, 426–427 (2019).

10. Park, M. S. *et al.* A Highly Reversible Lithium Metal Anode. *Sci Rep* **4**, 3815 (2015).

11. Aslam, M. K. *et al.* How to avoid dendrite formation in metal batteries: Innovative strategies for dendrite suppression. *Nano Energy* **86**, 106142 (2021).

12. Cao, D. *et al.* Lithium Dendrite in All-Solid-State Batteries: Growth Mechanisms, Suppression Strategies, and Characterizations. *Matter* **3**, 57–94 (2020).

13. Azammi, A. M. N. *et al.* Characterization studies of biopolymeric matrix and cellulose fibres based composites related to functionalized fibre-matrix interface. in *Interfaces in Particle and Fibre Reinforced Composites* 29–93 (Elsevier, 2020). doi:10.1016/B978-0-08-102665-6.00003-0.

14. Li, S. *et al.* Progress and Perspective of Ceramic/Polymer Composite Solid Electrolytes for Lithium Batteries. *Adv. Sci.* **7**, 1903088 (2020).

15. Zhao, Y. *et al.* Solid Polymer Electrolytes with High Conductivity and Transference Number of Li Ions for Li-Based rechargeable Batteries. (2021).

16. Hoang Huy, V. P., So, S. & Hur, J. Inorganic Fillers in Composite Gel Polymer Electrolytes

for High-Performance Lithium and Non-Lithium Polymer Batteries. *Nanomaterials* **11**, 614 (2021).

17. Kalhoff, J., Eshetu, G. G., Bresser, D. & Passerini, S. Safer Electrolytes for Lithium-Ion Batteries: State of the Art and Perspectives. *ChemSusChem* **8**, 2154–2175 (2015).

18. Zhu, M. *et al.* Recent advances in gel polymer electrolyte for high-performance lithium batteries. *Journal of Energy Chemistry* **37**, 126–142 (2019).

19. Gohy, J.-F. LCHM1361 - Introduction à la chimie des polymères. (2019).

20. http://unf3s.cerimes.fr/media/paces/Grenoble_1112/peuchmaur_marine/peuchmaur_marine_p02/peuchmaur_marine_p02.pdf.

21. Flory, J. P. *Principles of Polymer Chemistry*. (Cornell University Press, 1953).

22. Zecheru, T. New biopolymers with possible use in dentistry and orthopaedics. 237.

23. *Step-growth polymerization*. (s. d.-a). Plastics Technology. https://polymerdatabase.com/polymer%20chemistry/Stepgrowth%20Polymerization.html

24. Gohy, J.-F. & Fustin, C.-A. LCHM2261 - Polymer Chemistry and Physical Chemistry. (2021).

25. Keddie, D. J. A guide to the synthesis of block copolymers using reversible-addition fragmentation chain transfer (RAFT) polymerization. *Chem. Soc. Rev.* **43**, 496–505 (2014).

26. Goossens, K., Lava, K., Bielawski, C. W. & Binnemans, K. Ionic Liquid Crystals: Versatile Materials. *Chem. Rev.* **116**, 4643–4807 (2016).

27. Shin-Tson, W. & Deng-ke, Y. *Fundamentals of Liquid Crystal Devices*. (2006).

28. Collings, P. J. & Hird, M. *Introduction to Liquid Crystals Chemistry and Physics*. (1997).

29. Guégan, R. Etude des propriétés d'un cristal liquide (8CB) confiné dans des nanopores unidirectionnels. 177.

30. Paquette, J. A. Synthesis and Investigation of the Liquid Crystalline Properties of Polycyclic Aromatic Hydrocarbons. 112.

31. Fonseca-Santos, B., Chorilli, M. & Palmira Daflon Gremião, M. Nanotechnology-based drug delivery systems for the treatment of Alzheimer’s disease. *IJN* 4981 (2015) doi:10.2147/IJN.S87148.

32. Garcia, Y. LCHM2122 - Physical Methods for the Analysis of Solids. (2021).

33. *Chip DSC 10 – Polymères - PET | Linseis Messgeräte GmbH*. (s. d.-a). Linseis Messgeräte GmbH. https://www.linseis.com/fr/votre-industrie/polymeres/chip-dsc-10-polymeres-pet/

34. Liu, X. & Yu, W. Evaluating the thermal stability of high performance fibers by TGA. 8.

35. Review, A. Thermogravimetric Analysis. 19.

36. Borhade, A. V., Kshirsagar, T. A., Dholi, A. G. & Agashe, J. A. Removal of Heavy Metals Cd^{2+}, Pb^{2+}, and Ni^{2+} From Aqueous Solutions Using Synthesized Azide Cancrinite, $Na_8[AlSiO_4]_6(N_3)_{2.4}(H_2O)_{4.6}$. *J. Chem. Eng. Data* **60**, 586–593 (2015).

37. Williams, T. Gel permeation chromatography: A review. *J Mater Sci* **5**, 811–820 (1970).

38. Singleton, M. LCHM2152 - NMR complements. (2021).

39. Magar, H. S., Hassan, R. Y. A. & Mulchandani, A. Electrochemical Impedance Spectroscopy (EIS): Principles, Construction, and Biosensing Applications. *Sensors* **21**, 6578 (2021).

40. Meddings, N. Application of electrochemical impedance spectroscopy to commercial Li-ion cells: A review. *Journal of Power Sources* 27 (2020).

41. Lisdat, F. & Schäfer, D. The use of electrochemical impedance spectroscopy for biosensing. *Anal Bioanal Chem* **391**, 1555–1567 (2008).

42. Ribeiro, D. V., Souza, C. A. C. & Abrantes, J. C. C. Use of Electrochemical Impedance Spectroscopy (EIS) to monitoring the corrosion of reinforced concrete. *Rev. IBRACON Estrut. Mater.* **8**, 529–546 (2015).

43. Wolman, M. Polarized light microscopy as a tool of diagnostic pathology. 30.

44. Bontempelli, G., Dossi, N. & Toniolo, R. Linear Sweep and Cyclic☆. in *Reference Module in Chemistry, Molecular Sciences and Chemical Engineering* B9780124095472122000 (Elsevier, 2016). doi:10.1016/B978-0-12-409547-2.12200-0.

45. Kopylov, E. A., Mizrah, E. A., Fedchenko, A. S. & Lobanov, D. K. Study of a lithium-ion battery charge-discharge test unit characteristics*. *IOP Conf. Ser.: Mater. Sci. Eng.* **122**, 012015 (2016).

46. Yu, J. W. *et al.* Enhancement of the crosslink density, glass transition temperature, and strength of epoxy resin by using functionalized graphene oxide co-curing agents. *Polym. Chem.* **7**, 36–43 (2016).

47. Shim, J., Kim, D.-G., Kim, H. J., Lee, J. H. & Lee, J.-C. Polymer Composite Electrolytes Having Core–Shell Silica Fillers with Anion-Trapping Boron Moiety in the Shell Layer for All-Solid-State Lithium-Ion Batteries. *ACS Appl. Mater. Interfaces* **7**, 7690–7701 (2015).

48. Xu, W. *et al.* Polymorphic Phase Formation of Liquid Crystals Distributed in Semicrystalline Polymers: An Indicator of Interlamellar and Interspherulitic Segregation. *J.*

Phys. Chem. Lett. **12**, 4378–4384 (2021).

49. Figueiredo, T. V. B. Injectable and self-healing polysaccharide hydrogels via boronate ester bonds: relationships between the binding mode of boronic acids to saccharide moieties and the macroscopic mechanical properties. 267.

UNIVERSITÉ CATHOLIQUE DE LOUVAIN
Faculté des sciences
Place des sciences, 2 bte L6.06.01, 1348 Louvain-la-Neuve, Belgique | **www.uclouvain.be/sc**